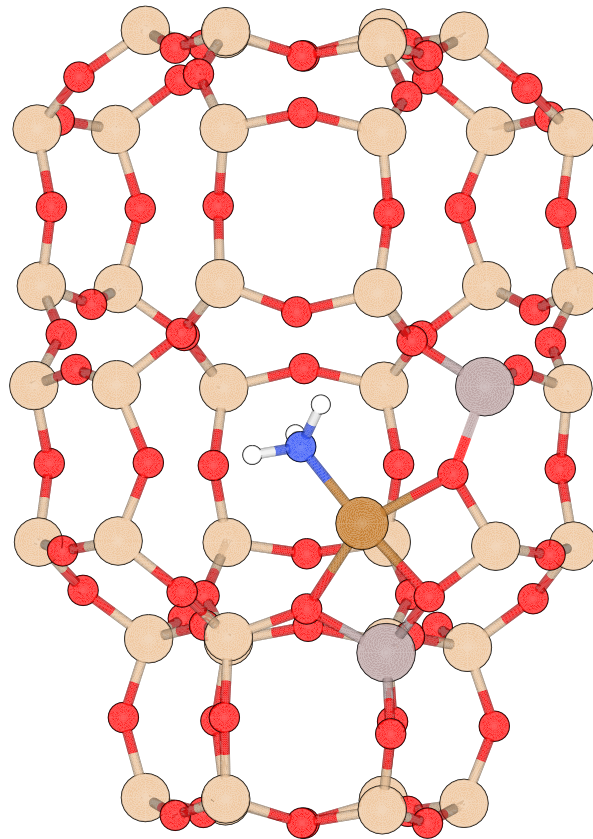




**CHALMERS**  
UNIVERSITY OF TECHNOLOGY

---



# Enhancing ammonia storage by tailoring zeolite doping

A study of different dopants and their position

Master's thesis in Applied Physics

DAVID SCHÖRLING



MASTER'S THESIS 2020

# Enhancing ammonia storage by tailoring zeolite doping

A study of different dopants and their position

DAVID SCHÖRLING



**CHALMERS**  
UNIVERSITY OF TECHNOLOGY

Department of Physics  
Division of Chemical Physics  
CHALMERS UNIVERSITY OF TECHNOLOGY  
Gothenburg, Sweden 2020

Enhancing ammonia storage by tailoring zeolite doping  
A study of different dopants and their position  
DAVID SCHÖRLING

© DAVID SCHÖRLING, 2020.

Supervisors: Professor Henrik Grönbeck, Department of Physics  
Doctor Fredrik Blomgren, Volvo Group  
Examiner: Professor Henrik Grönbeck, Department of Physics

Master's Thesis 2020  
Department of Physics  
Division of Chemical Physics  
Chalmers University of Technology  
SE-412 96 Gothenburg  
Telephone +46 31 772 1000

Cover: An  $\text{NH}_3$  molecule on a  $\text{Cu(II)}$  counter ion adsorbed to an Al doped CHA zeolite.

Typeset in L<sup>A</sup>T<sub>E</sub>X  
Printed by Chalmers Reproservice  
Gothenburg, Sweden 2020

Enhancing ammonia storage by tailoring zeolite doping

A study of different dopants and their position

DAVID SCHÖRLING

Department of Physics

Chalmers University of Technology

## Abstract

Selective catalytic reduction with  $\text{NH}_3$  as a reducing agent ( $\text{NH}_3$ -SCR) is currently the most widely used technology to reduce  $\text{NO}_x$  emissions from automotive diesel engines. One of the most prevalent types of catalysts for this purpose is zeolites. The technology requires storage of  $\text{NH}_3$  in the zeolites over a large temperature range.  $\text{NH}_3$  is stored by adsorption to  $\text{H}^+$  Brønsted acid sites and other counter ions.

In this thesis, adsorption of  $\text{NH}_3$  in the zeolites CHA, BEA and MFI and the zeolite like structure AIPO have been investigated using density functional theory (DFT). In all cases, the effect of doping the zeolite framework was explored. Calculations were performed for four different dopant atoms and the counter ions  $\text{H}^+$ , Cu(I), Cu(II) and Cu(II) with  $(\text{OH})^-$  adsorbed. It was found that the type of dopant atom has a clear effect on the adsorption energies of  $\text{NH}_3$  on  $\text{H}^+$  and Cu(II), while the effect is less noticeable in the cases of Cu(I) and Cu(II) with  $(\text{OH})^-$  adsorbed. The type of zeolite was also found to largely influence the results. The effect of different Al dopant distributions in CHA was also explored. It was found that the relative positions of the dopant atoms have a considerable impact on the adsorption energies.

Keywords: AIPO, BEA, catalysis, CHA, Cu, DFT, Al distribution, MFI,  $\text{NH}_3$ ,  $\text{NO}_x$ , SCR, temperature programmed desorption, zeolites



## Acknowledgements

First I would like to thank my supervisor at Chalmers Professor Henrik Grönbeck for always being fully committed to the project, always being available for questions and finally making me come to terms with the number of vibrational frequencies. Your guidance made the project even more interesting and fun than it seemed at the start. I would also like to thank my supervisor at Volvo Doctor Fredrik Blomgren for proposing ways to cater the project towards applications of interest at Volvo and for letting me present the thesis at your group.

A huge thank you and congratulations on your doctoral degree to my co-supervisor Doctor Lin Chen for explaining your previous work and letting me build upon it. You always being available for answering questions was a huge benefit. Thank you to my officemate during this semester Philip Edenborg for the good company and helping me set up the computation scripts. I also want to thank all of my co-workers at the Division of Chemical Physics and KCK for the nice atmosphere and for letting me occupy your computational resources during this period. An extra thank you to Doctor Adam Arvidsson for giving me the zeolite structures.

David Schörling, Gothenburg, January 2020



# Contents

<b>1</b>	<b>Introduction</b>	<b>1</b>
1.1	Role of zeolites in $\text{NO}_x$ conversion . . . . .	1
1.2	Background . . . . .	3
1.3	Scope . . . . .	3
<b>2</b>	<b>Zeolites</b>	<b>5</b>
2.1	Considered types of zeolite structures . . . . .	6
2.2	Dopant atoms and counter ions . . . . .	8
<b>3</b>	<b>Density functional theory</b>	<b>11</b>
3.1	Schrödinger equation for a system of particles . . . . .	11
3.2	The Born-Oppenheimer approximation . . . . .	12
3.3	The Hohenberg-Kohn theorems . . . . .	12
3.4	The Kohn-Sham approach . . . . .	13
3.4.1	Exchange-correlation approximations . . . . .	14
3.4.2	Plane wave expansion of the Kohn-Sham orbitals . . . . .	16
3.4.3	Pseudo potentials . . . . .	16
3.4.4	Sampling the first Brillouin zone . . . . .	17
<b>4</b>	<b>Calculating zeolite properties</b>	<b>19</b>
4.1	Obtaining atomic structures . . . . .	19
4.2	Vibrational frequencies . . . . .	19
4.2.1	Derivation of frequencies in an atomic structure . . . . .	20
4.2.2	Vibrational frequencies in the zeolites . . . . .	21
4.3	Acquiring the adsorption energies of $\text{NH}_3$ . . . . .	21
4.3.1	Zero-point correction of ground state energies . . . . .	22
4.3.2	Comparison to OH frequency shift on CO adsorption . . . . .	22
4.4	Oxidation states of dopant atoms . . . . .	23
4.5	Bond orders from the electron density . . . . .	23
4.6	Thermodynamics from DFT calculations . . . . .	25
4.6.1	Partition function of molecules in an ideal gas . . . . .	25
4.6.2	Gibbs free energy of adsorption . . . . .	26
4.6.3	Temperature programmed desorption curves . . . . .	27
4.7	Computational setup of DFT calculations . . . . .	29
<b>5</b>	<b>Results</b>	<b>31</b>
5.1	Cell volumes of the structures . . . . .	31

5.2	Investigated dopant configurations . . . . .	33
5.3	NH <sub>3</sub> adsorption at Brønsted sites . . . . .	36
5.3.1	Comparison to O-H bond order . . . . .	39
5.3.2	Oxidation states of dopant atoms . . . . .	39
5.3.3	Comparison to OH frequency shift on CO adsorption . . . . .	40
5.3.4	TPD curves for Brønsted site desorption . . . . .	42
5.4	NH <sub>3</sub> adsorption on Cu(I) . . . . .	42
5.4.1	Comparison to O-Cu bond order . . . . .	48
5.4.2	Phase diagrams for Al/Si doped structures . . . . .	49
5.4.3	TPD curves for Al/Si doped structures . . . . .	50
5.5	NH <sub>3</sub> adsorption on Cu(II) . . . . .	50
5.5.1	Phase diagrams for different dopant atoms in CHA . . . . .	58
5.5.2	TPD curves for different dopant atoms in CHA . . . . .	58
5.6	(Cu(I)(NH <sub>3</sub> ) <sub>4</sub> ) <sup>+</sup> vs (Cu(II)(NH <sub>3</sub> ) <sub>4</sub> ) <sup>2+</sup> shapes . . . . .	59
5.7	Distributions of two Al dopant atoms in CHA . . . . .	60
5.7.1	General properties of the dopant distributions . . . . .	66
5.7.2	Phase diagrams for different Al distributions . . . . .	69
5.7.3	TPD curves for different Al distributions . . . . .	69
5.8	NH <sub>3</sub> adsorption on Cu(II) with (OH) <sup>-</sup> . . . . .	70
5.9	Possibility of H <sub>2</sub> O dissociation . . . . .	76
<b>6</b>	<b>Discussion</b>	<b>79</b>
6.1	Thoughts on the methods used . . . . .	79
6.1.1	Finding the global minima . . . . .	79
6.1.2	Effect of local minima . . . . .	79
6.1.3	Treatment of entropy in the structures . . . . .	80
6.2	Thoughts on the results . . . . .	80
6.2.1	Consistency of the results . . . . .	80
6.2.2	Comparison to previous studies . . . . .	81
6.3	Connection to NO <sub>x</sub> reduction . . . . .	82
6.3.1	Stability of the structures . . . . .	82
6.3.2	Effect of dopant distribution on NO <sub>x</sub> conversion . . . . .	82
6.4	Possible further work . . . . .	83
<b>7</b>	<b>Conclusion</b>	<b>85</b>

# 1

## Introduction

A catalyst introduces alternative reaction paths with favourable barriers for a chemical reaction, without itself being consumed in the process [1]. It can make desired reactions take place while still prohibiting unwanted ones, so that the desired products are acquired. It is this selectivity that makes catalysis play a vital role in many different industrial applications today, such as production of chemicals and emission control [1].

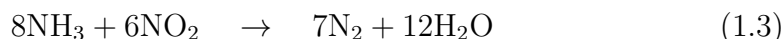
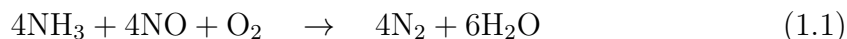
Catalysts are usually categorized into two main groups, namely homogeneous and heterogeneous catalysts. A homogeneous catalyst is in the same phase as the involved reactants and products, while a heterogeneous is not [1]. One example of a heterogeneous catalyst is zeolites, which during the last decade have proved to perform well in reducing  $\text{NO}_x$  emissions from diesel engines [2].

### 1.1 Role of zeolites in $\text{NO}_x$ conversion

$\text{NO}_x$  alludes at both  $\text{NO}$  and  $\text{NO}_2$ , and is one of the most prevalent and dangerous air pollutants stemming from combustion, which makes it vital to reduce such emissions [3]. Today companies that are responsible for  $\text{NO}_x$  emissions have to deal with both legislative and consumer demands. From 1992 to 2013, the European heavy duty emissions regulations on  $\text{NO}_x$  set by the European Union went from  $8.0 \text{ g (kWh)}^{-1}$  to  $0.46 \text{ g (kWh)}^{-1}$  [4].

One of the main sources of  $\text{NO}_x$  emissions is diesel engines in automotive vehicles [3]. In gasoline engines, the three-way catalyst is universally accepted as the best available choice to control the emissions. However, it requires stoichiometric conditions, which prevents it from being used in diesel engine exhausts [5].

Instead of the three-way catalyst, the current technology of choice is selective catalytic reduction with  $\text{NH}_3$  as a reducing agent ( $\text{NH}_3\text{-SCR}$ ) [2]. With  $\text{NH}_3$ , there are mainly three different reactions in the catalyst that convert  $\text{NO}_x$  into harmless products. The three reactions are [2]:



What reaction that dominates depends on the ratio of NO to NO<sub>2</sub>. Usually there is a vast majority of NO. This means that reaction (1.1), which is called standard SCR, is the most common one [2]. Since reaction (1.2) is the fastest, a ratio of 1 is preferred for maximum NO<sub>x</sub> conversion.

A catalyst that has been found to promote reactions (1.1)-(1.3) while also prohibiting unwanted side reactions, like production of NO or N<sub>2</sub>O, is zeolites [2]. Zeolites are porous aluminosilicates inside of which NH<sub>3</sub> can be stored [6]. NH<sub>3</sub> binds to the zeolites at sites where Si atoms are replaced by dopant atoms. Since there are different types of zeolite frameworks and different types and distributions of dopant atoms, there are wide varieties of ways to design a zeolite depending on the operating conditions. The dopant atoms have one valence electron less than Si, this valence electron is reintroduced by introducing counter ions. The counter ions are located within the pores of the zeolites, and it is to these that the NH<sub>3</sub> actually adsorb to [7, 8]. Examples of counter ions are H<sup>+</sup> and Cu(I). A detailed overview of the atomic configurations of the considered zeolites is given in chapter 2.

The catalyst for NO<sub>x</sub> reduction of an exhaust system is commonly called the SCR and is only one of many parts of the exhaust aftertreatment system (EATS) for a diesel engine [4]. The exhaust that enters the EATS is a mix of soot, CO, hydrocarbons and NO<sub>x</sub> [4]. There are many ways in which an EATS can be designed. However, one of the most common ways is described in figure 1.1. In the first part of the EATS, the diesel oxidation catalyst (DOC) takes care of the hydrocarbons and CO while also oxidizing some of the NO into NO<sub>2</sub>, making reaction (1.2) take place at a higher rate [4]. Downstream the DOC sits the diesel particulate filter (DPF), in which soot is captured and stored [2].

After the DPF, a solution of urea ((NH<sub>2</sub>)<sub>2</sub>CO) and H<sub>2</sub>O is pumped into the exhaust pipe, which reacts owing to the high temperature in the following two steps, creating 2NH<sub>3</sub> and CO<sub>2</sub> [4].



The produced NH<sub>3</sub> reacts with NO<sub>x</sub> and O<sub>2</sub> in the SCR according to reactions (1.1)-(1.3). The urea solution is controlled with respect to how much NO<sub>x</sub> that manages to pass through the SCR, so that a sufficient amount is added [4]. When the driving conditions change however, like driving uphill after a long plain straight, more NH<sub>3</sub> is needed. Because of this, having a reserve of NH<sub>3</sub> in the SCR zeolite is essential to deal with an unexpected rise of NO<sub>x</sub> production. Additionally, NH<sub>3</sub> slipping through the zeolite is also a source of air pollution. This means that being able to bind NH<sub>3</sub> at a wide variety of temperatures is a preferable property of the zeolite.

The NH<sub>3</sub> that slips through the SCR is converted mainly into N<sub>2</sub> in the ammonia slip catalyst (ASC) [9].

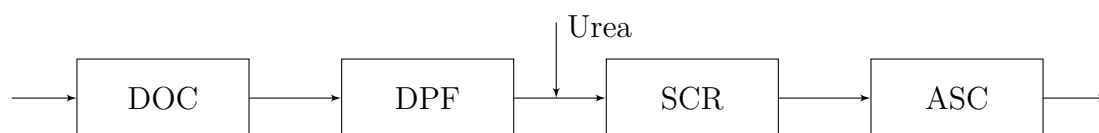


**Figure 1.1:** Schematic overview of a standard EATS for diesel engines. The arrows show the direction of the exhaust flow. An urea solution is added between the DPF and SCR.

## 1.2 Background

Previous work has been performed on the ability to store  $\text{NH}_3$  of Al doped CHA framework zeolites with  $\text{H}^+$ , Cu(I), Cu(II) and Cu(II) with  $(\text{OH})^-$  adsorbed as counter ions [7]. This was done by calculating the adsorption energies of  $\text{NH}_3$  using density functional theory (DFT), which is a method for solving the quantum mechanical equations. The results were related to experimentally measurable properties by constructing temperature programmed desorption (TPD) curves. The ability of Al doped CHA to adsorb  $\text{NH}_3$  at different temperatures and pressures was also visualized in phase diagrams.

Now it is time to extend the study to other zeolite frameworks and dopant atoms, with the goal of finding systems that bind  $\text{NH}_3$  even better than the catalysts currently used in diesel engine exhaust aftertreatment systems.

## 1.3 Scope

The project aims at finding higher adsorption energies of  $\text{NH}_3$  in zeolites than currently known. This is done by testing a variety of dopant atom types and positions in the zeolites CHA, BEA and MFI and the zeolite like structure AlPO with  $\text{H}^+$ , Cu(I), Cu(II) and Cu(II) with  $(\text{OH})^-$  as counter ions, using density functional theory calculations. As in the previous work [7], TPD curves are constructed to relate the results to experimentally measurable properties and phase diagrams are created for visualization of the structures ability to adsorb  $\text{NH}_3$ . Additionally, possible connections between the adsorption energies and the electronic structures of the systems, such as bond orders and oxidation states, are studied.

Only  $\text{NH}_3$  and how it interacts with the considered zeolites is studied. Possible side reactions where  $\text{NO}_x$  is converted into other harmless gasses are not studied. However, the possible implications of the results on  $\text{NO}_x$  conversion is discussed in section 6.3.



# 2

## Zeolites

Zeolites are crystalline materials consisting of O bound to either Si or Al [6]. They occur naturally in many different frameworks. However, because of a high density of impurities in naturally occurring ones, the zeolites used in catalytic applications are synthesised [6]. In this thesis, pure silicate zeolites with sporadic Si atoms exchanged with dopant atoms are considered. A pure silicate zeolite is presented schematically in figure 2.1.

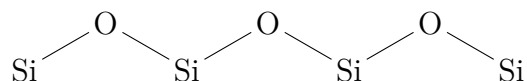


**Figure 2.1:** Si and O atoms arranged as in a pure silicate zeolite.

There are four O atoms bound to every Si atom, forming tetrahedral units of  $\text{SiO}_4$ . Every O atom is part of two of these tetrahedral units, which means that there are twice the amount of O atoms as there are Si atoms. The units of  $\text{Si}^{4+}(\text{O}^{2-})_2$  have closed electronic shells since Si has four and each O has six valence electrons.

One of the main properties that makes zeolites interesting for selective catalysis is that they are porous, which means that molecules can enter the pores [6].

The color codes and relative atomic radii of the atoms visualized in this thesis are presented in figure 2.2.

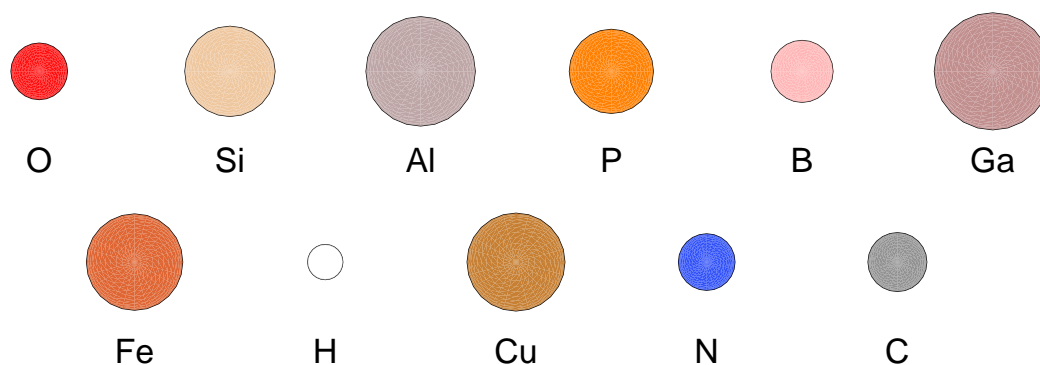
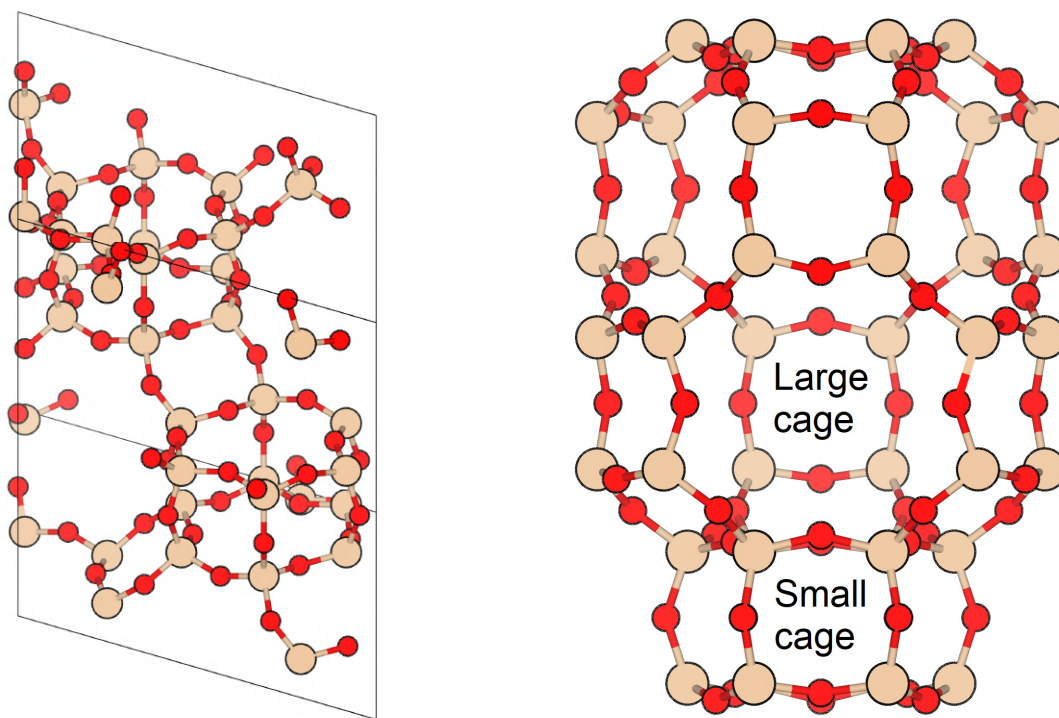


**Figure 2.2:** The atoms visualized in this thesis.

## 2.1 Considered types of zeolite structures

There are various different zeolite frameworks that occur naturally or that can be synthesised [6]. In this thesis, three different zeolite types are studied, namely SSZ-13, Beta and ZSM-5. However, the zeolite and framework names are often used interchangeably. The framework of SSZ-13 is CHA, the framework of Beta is BEA and the framework of ZSM-5 is MFI [10, 11, 12].

The primitive unit cell of CHA consists of 36 atoms, where 12 atoms are Si and 24 atoms are O [7]. However, the structure is easier visualized in a larger cell, in figure 2.3a the hexagonal unit cell with 108 atoms is presented. CHA can also be visualized by its two characteristic cages, the large one consists of four-, six- and eight-membered rings while the small one consists of four- and six-membered rings. The two cages are presented in figure 2.3b.



(a) Hexagonal unit cell of CHA.

(b) Characteristic cages of CHA.

**Figure 2.3:** Two visualizations of the CHA framework.

The primitive unit cell of BEA consists of 192 atoms, where 64 are Si and 128 are O [11, 12]. It is presented in figure 2.4. The primitive unit cell of MFI consists of 288 atoms, where 96 are Si and 192 are O [11, 12]. Two views of MFI are presented in figure 2.5.

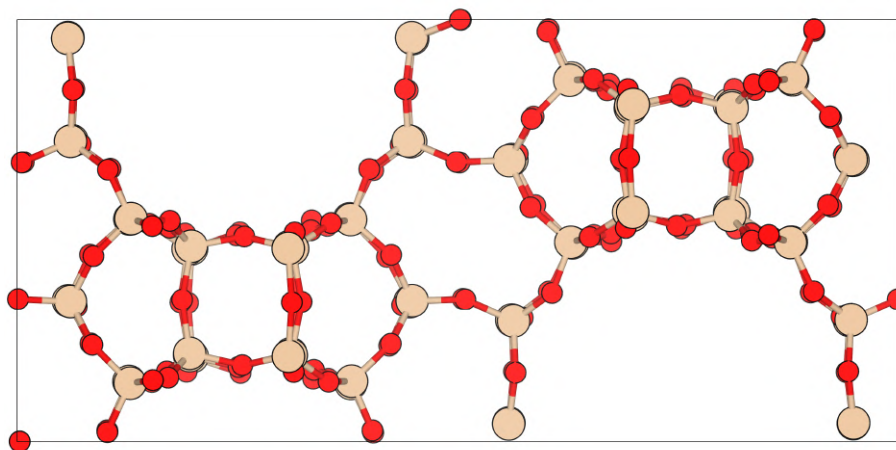


**Figure 2.4:** The primitive unit cell of BEA.

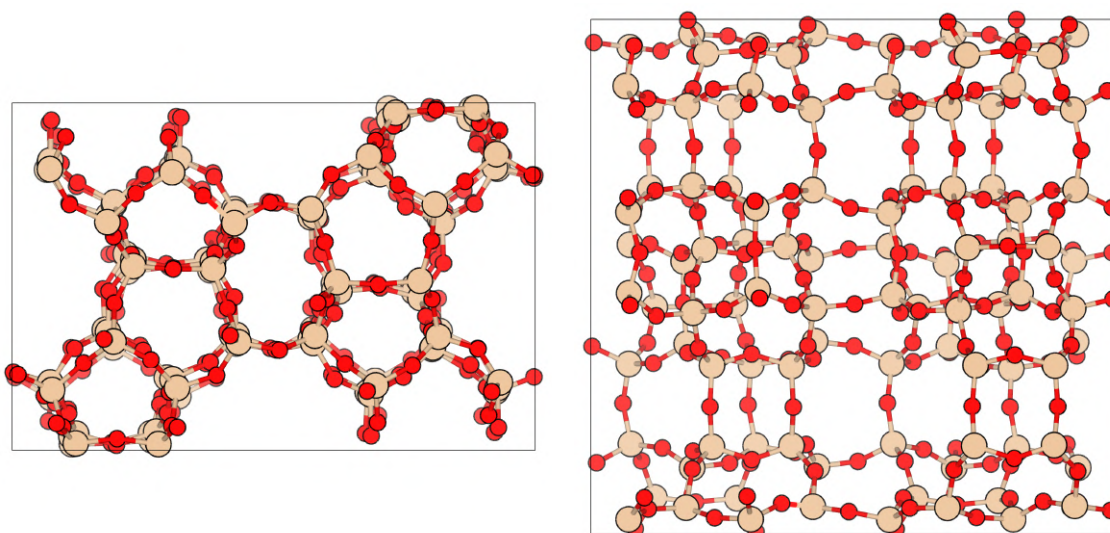


**Figure 2.5:** Two views of the primitive unit cell of MFI.

One zeolite-like structure is also studied, namely aluminium phosphate ( $\text{AlPO}_4$ ) in the CHA framework, often called AIPO [11, 12]. Compared to zeolites, every other Si atom are replaced by Al and every other by P. Since Si has 4, Al has 3 and P has 5 valence electrons, AIPO is isoelectronic to zeolites. A pure AIPO structure is presented schematically in figure 2.6.

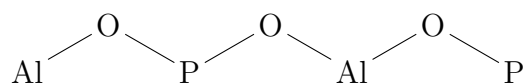


**Figure 2.6:** Al, P and O atoms arranged as in pure AIPO.

The hexagonal unit cell and characteristic cages of AIPO have the same structure as the CHA zeolite, since AIPO is in the CHA framework. They are presented in figure 2.7a and 2.7b, respectively.

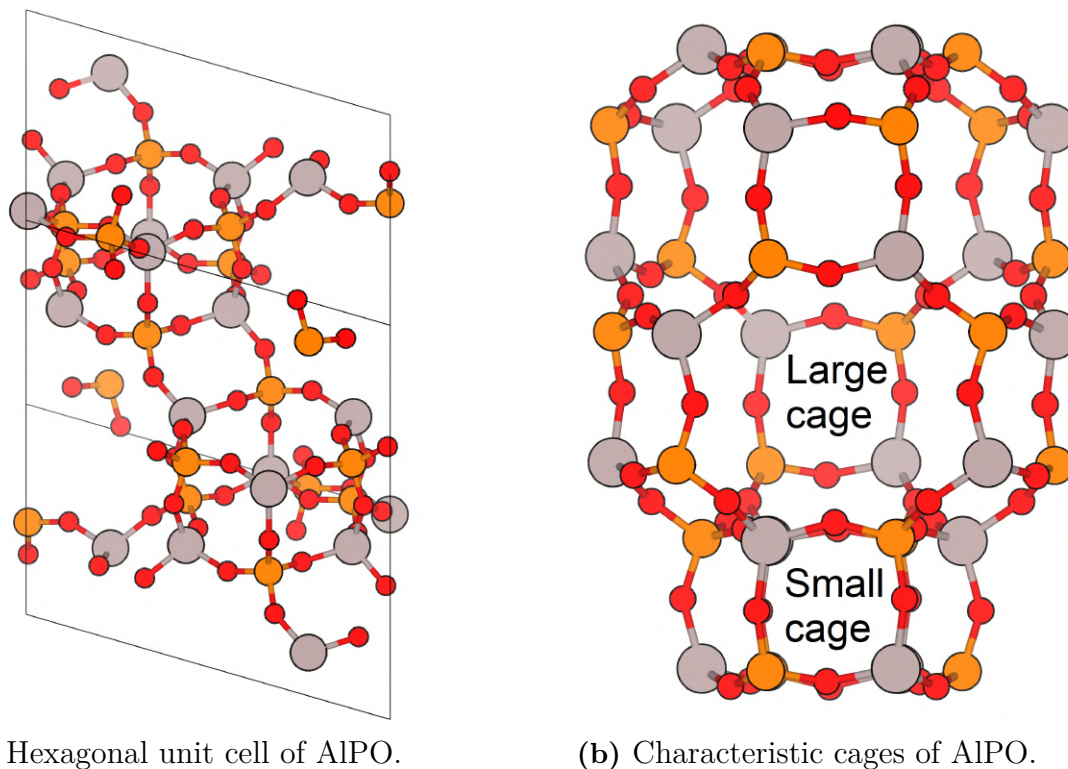


**Figure 2.7:** Two visualizations of AlPO in the CHA framework.

## 2.2 Dopant atoms and counter ions

The first step in being able to bind  $\text{NH}_3$  to zeolites is to replace some Si atoms with dopant atoms [7, 8]. By replacing one of the Si atoms with an atom that has only three valence electrons, one extra electron is needed to obtain a closed electronic shell for the unit of the dopant atom and two nearby O atoms. The extra electron is obtained by introducing a counter ion, that occupies a site close to one of the O atoms next to the dopant atom. In figure 2.8, the case of having an Al dopant atom with  $\text{H}^+$  as a counter ion is visualized. The site of a  $\text{H}^+$  counter ion is called a Brønsted acid site [13].

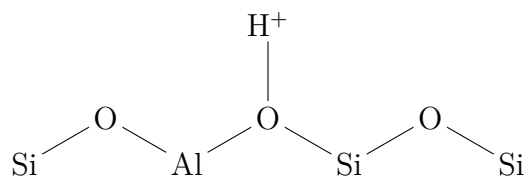


**Figure 2.8:** Si and O atoms arranged as in a pure silicate zeolite, but with one Si atom replaced by an Al dopant atom and a  $\text{H}^+$  counter ion bound to a nearby O atom.

It is the counter ions that  $\text{NH}_3$  adsorb to in the zeolites [7, 8].  $\text{H}^+$  counter ions are commonly found naturally in zeolites [6]. In the SCR of a diesel engine exhaust, it is desirable to have a wide variety of adsorption energies for  $\text{NH}_3$  so that the catalyst binds  $\text{NH}_3$  over a large temperature range. To achieve this, it is possible to

introduce other counter ions than  $H^+$ , for example Cu [6, 8]. Cu counter ions are also needed for dissociation of  $O_2$ , which is a vital sub reaction of reaction (1.1) [14].

The case of Cu(I) binding to O next to an Al dopant atom is presented in figure 2.9.

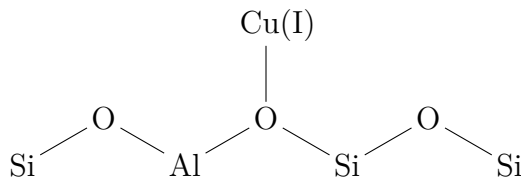


**Figure 2.9:** Si and O atoms arranged as in a pure silicate zeolite, but with one Si atom replaced by an Al dopant atom and a Cu(I) counter ion bound to a nearby O atom.

In the case of two dopant atoms close to each other and one Cu counter ion, the Cu ion obtains an oxidation state of +2. Two Al dopant atoms with a Cu(II) counter ion bound to a nearby O atom is presented in figure 2.10.

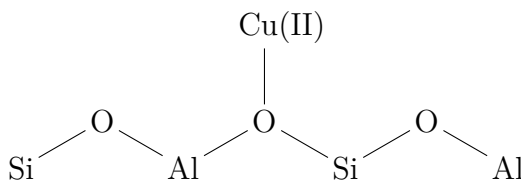


**Figure 2.10:** Si and O atoms arranged as in a pure silicate zeolite, but with two Si atoms replaced by Al dopant atoms and a Cu(II) counter ion bound to a nearby O atom.

During the synthesis, the dopant atoms cannot be placed so close that there is only one O atom between them. This is known as Löwenstein's rule [15]. Otherwise the Si to dopant ratio and the positions of the dopant atoms relative to each other can be controlled somewhat to suit a given application [16, 17, 18, 19].

There often exist  $H_2O$  in zeolites [10], of which one  $H^+$  can desorb from and produce a Brønsted site, leaving OH. This OH can then bind to a Cu(I) counter ion, making it Cu(II) since the OH needs one electron to obtain a closed electronic shell. This arrangement is presented in figure 2.11.

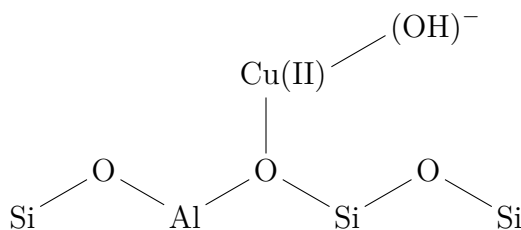


**Figure 2.11:** Si and O atoms arranged as in a pure silicate zeolite, but with one Si atom replaced by an Al dopant atom and a Cu(II) counter ion bound to a nearby O atom and  $(OH)^-$ .

For AlPO, one either replace Al or P atoms. In the case of replacing Al, the dopant atom should have two valence electrons, while when replacing P, the dopant atom should have four valence electrons [11, 12].

Previous studies have shown that at most one  $\text{NH}_3$  molecule at a time can bind to  $\text{H}^+$ , while up to four can bind to Cu(I) and Cu(II) counter ions. In the case of  $(\text{OH})^-$  binding to a Cu(II) counter ion, up to three  $\text{NH}_3$  can bind to it [7, 8].

# 3

## Density functional theory

The Schrödinger equation can be solved exactly only for one electron systems [20]. Thus, when considering many particle systems, approximations have to be made. When dealing with systems of hundreds of atoms, density functional theory (DFT) has during the last couple of decades proved to be a successful approach [21].

In this chapter, the different approximations made, going from the Schrödinger equation to performing calculations using DFT, are presented.

### 3.1 Schrödinger equation for a system of particles

A general quantum system can be described by the time independent Schrödinger equation [22].

$$\hat{H}\psi_n = E_n\psi_n$$

Here  $\hat{H}$  is the Hamiltonian of the system, while  $\psi_n$  and  $E_n$  are the corresponding wavefunctions and energy eigenvalues, respectively.

The Hamiltonian of a many particle system contains cross terms between all of the involved particles, these cross terms make it impossible to find an analytic solution. Consider a system of nuclei with atomic numbers  $Z_k$  and masses  $M_k$  and electrons of mass  $m_e$ . In the non-relativistic limit, the system is described by the following Hamiltonian (in Hartree atomic units<sup>1</sup>) [23].

$$\begin{aligned} \hat{H} = & - \sum_k \frac{1}{2M_k} \nabla_k^2 - \sum_i \frac{1}{2} \nabla_i^2 \\ & + \frac{1}{2} \sum_{k \neq m} \frac{Z_k Z_m}{|\mathbf{R}_k - \mathbf{R}_m|} + \frac{1}{2} \sum_{i \neq j} \frac{1}{|\mathbf{r}_i - \mathbf{r}_j|} - \sum_{i,k} \frac{Z_k}{|\mathbf{r}_i - \mathbf{R}_k|.} \end{aligned} \quad (3.1)$$

The first two terms correspond to the kinetic energy of the nuclei and electrons, respectively. The third, fourth and fifth terms correspond to the nucleus-nucleus, electron-electron and nucleus-electron Coulomb interactions, respectively. The wavefunctions corresponding to the Hamiltonian in equation (3.1) are functions of the spatial coordinates of all nuclei and electrons of the system [23].

$$\psi_n = \psi_n(\mathbf{r}_1, \mathbf{r}_2, \dots, \mathbf{R}_1, \mathbf{R}_2, \dots) =: \psi_n(\mathbf{r}, \mathbf{R})$$

---

<sup>1</sup>The electron mass  $m_e$  and charge  $e$ , Planck's reduced constant  $\hbar$  and the Coulomb force constant  $1/(4\pi\epsilon_0)$  are all set equal to 1.

Thus, in the case of  $N$  particles, the wavefunction is  $3N$  dimensional. It is clear that the difficulty of solving the problem scales rapidly with the number of involved particles.

## 3.2 The Born-Oppenheimer approximation

To solve the Schrödinger equation corresponding to the Hamiltonian in equation (3.1), one needs to implement a couple of approximations, first of which is the Born-Oppenheimer approximation [24]. It states that the electrons stay in their adiabatic eigenstates when the nuclei move. This means that the total wavefunctions can be separated into one factor for the nuclei and one factor for the electrons [23].

$$\psi_n(\mathbf{r}, \mathbf{R}) = \psi_n^{\text{ele}}(\mathbf{r}; \mathbf{R})\psi_n^{\text{huc}}(\mathbf{R}),$$

Here  $\psi_n^{\text{ele}}(\mathbf{r}; \mathbf{R})$  depends only parametrically on  $\mathbf{R}$ . The Born Oppenheimer approximation can be intuitively motivated by the nuclei having a mass that is much larger than the electron mass ( $M_k \gg m_e$ ).

It is now possible to consider the Schrödinger equation only for the electronic parts of the Hamiltonian in equation (3.1) and treat the nuclei separately. The electronic Hamiltonian is

$$\hat{H}_{\text{ele}} = -\sum_i \frac{1}{2} \nabla_i^2 + \frac{1}{2} \sum_{i \neq j} \frac{1}{|\mathbf{r}_i - \mathbf{r}_j|} - \sum_{i,k} \frac{Z_k}{|\mathbf{r}_i - \mathbf{R}_k|}.$$

The remaining term containing the nuclear properties is identified as an external potential stemming from the nuclei.

$$V_{\text{ext}}(\mathbf{r}) = -\sum_{i,k} \frac{Z_k}{|\mathbf{r}_i - \mathbf{R}_k|}$$

The corresponding electronic Schrödinger equation is

$$\hat{H}_{\text{ele}}\psi_n^{\text{ele}}(\mathbf{r}; \mathbf{R}) = E_n(\mathbf{R})\psi_n^{\text{ele}}(\mathbf{r}; \mathbf{R})$$

where the energy eigenvalues  $E_n(\mathbf{R})$  are dependent on the positions of the nuclei.

## 3.3 The Hohenberg-Kohn theorems

Instead of using wavefunctions, it is possible to use the electron density. If there are  $N$  electrons, the dimensionality of the equation is then reduced from  $3N$  to 3. This was done already in 1927 by Thomas and Fermi [25, 26]. However, it was not until 1964 that Hohenberg and Kohn connected the approach to a solid theory. The two theorems, that form the basis of the theory, are [27]:

1. Any external potential  $V_{\text{ext}}(\mathbf{r})$  acting on an electronic system is determined uniquely by the ground state electron density  $n_0(\mathbf{r})$ , except for a constant.

2. There exists an energy functional  $E[n(\mathbf{r})]$  of the electron density  $n(\mathbf{r})$  for all external potentials  $V_{\text{ext}}(\mathbf{r})$ . The global minimum of the functional is the ground state energy of the system and the corresponding electron density is the ground state electron density  $n_0(\mathbf{r})$ .

The first Hohenberg-Kohn theorem leads to a very important conclusion. If the ground state electron density is determined, and thus the external potential  $V_{\text{ext}}(\mathbf{r})$  is determined, the Hamiltonian is also determined. From this follows that all other properties of the electronic system are also determined. However, although Hohenberg and Kohn stated that the ground state density uniquely determines all other properties of the system, they did not show how to actually obtain the properties from the ground state density.

The second Hohenberg-Kohn theorem states that there exists an energy functional  $E[n(\mathbf{r})]$  of the electron density  $n(\mathbf{r})$ . The exact form of the functional is however unknown. In order to obtain a useful expression for the energy functional, further approximations have to be made.

### 3.4 The Kohn-Sham approach

In 1965, Kohn and Sham made the assumption that the density of a system of interacting electrons is equal to the density of some fictitious system of non-interacting electrons in an effective potential  $V_{\text{KS}}(\mathbf{r})$ , named the Kohn-Sham potential [28]. The orbitals of these independent electrons  $\phi_i(\mathbf{r})$  are called the Kohn-Sham orbitals and obey a set of single particle equations, known as the Kohn-Sham equations.

$$\left(-\frac{1}{2}\nabla^2 + V_{\text{KS}}(\mathbf{r})\right)\phi_i(\mathbf{r}) = \epsilon_i\phi_i(\mathbf{r})$$

Here,  $\epsilon_i$  are the energy eigenvalues of the Kohn-Sham orbitals. In total,  $N$  single particle equations of dimensionality 3 now have to be solved. However, since the equations are not coupled, they are solved much easier than the original  $3N$  dimensional Schrödinger equation.

The electron density of this non-interacting system is obtained by summing the square modulus of all of the occupied Kohn-Sham orbitals.

$$n(\mathbf{r}) = \sum_i^N |\phi_i(\mathbf{r})|^2$$

Within the Kohn-Sham assumption, the energy functional of the non-interacting system of electrons can be expressed as

$$E[n(\mathbf{r})] = F[n(\mathbf{r})] + E_{\text{ext}}[n(\mathbf{r})]$$

where

$$E_{\text{ext}}[n(\mathbf{r})] = \int V_{\text{ext}}(\mathbf{r})n(\mathbf{r})d\mathbf{r} = -\sum_k \int \frac{Z_k}{|\mathbf{r} - \mathbf{R}_k|}n(\mathbf{r})d\mathbf{r}$$

stems from the external potential and  $F[n(\mathbf{r})]$  is a universal energy functional independent of the external potential. It can be separated into three terms.

$$F[n(\mathbf{r})] = T_0[n(\mathbf{r})] + E_{\text{H}}[n(\mathbf{r})] + E_{\text{xc}}[n(\mathbf{r})]$$

Here  $T_0[n(\mathbf{r})]$  is the kinetic energy of the non-interacting electrons and  $E_{\text{H}}[n(\mathbf{r})]$  is the classic Coulomb interaction between the electrons.

$$T_0[n(\mathbf{r})] = -\frac{1}{2} \sum_i \langle \phi_i | \nabla_i^2 | \phi_i \rangle$$

$$E_{\text{H}}[n(\mathbf{r})] = \frac{1}{2} \int \frac{1}{|\mathbf{r} - \mathbf{r}'|} n(\mathbf{r}) n(\mathbf{r}') d\mathbf{r} d\mathbf{r}'$$

$E_{\text{xc}}[n(\mathbf{r})]$  is an exchange-correlation functional, which in principle should contain the many-body interactions of the interacting electronic system that are left out from the non-interacting system.

The Kohn-Sham potential  $V_{\text{KS}}(\mathbf{r})$  acting on the non-interacting system can be calculated from the energy functional  $E[n(\mathbf{r})]$  according to

$$V_{\text{KS}}(\mathbf{r}) = V_{\text{ext}}(\mathbf{r}) + V_{\text{H}}(\mathbf{r}) + V_{\text{xc}}(\mathbf{r})$$

where

$$V_{\text{ext}}(\mathbf{r}) = \frac{\delta E_{\text{ext}}[n(\mathbf{r})]}{\delta n(\mathbf{r})}, \quad V_{\text{H}}(\mathbf{r}) = \frac{\delta E_{\text{H}}[n(\mathbf{r})]}{\delta n(\mathbf{r})}, \quad V_{\text{xc}}(\mathbf{r}) = \frac{\delta E_{\text{xc}}[n(\mathbf{r})]}{\delta n(\mathbf{r})}.$$

The Kohn-Sham equations can be solved iteratively to obtain the ground state electron density and other properties connected to the electronic structure, such as the total ground state energy and charge distribution. The self-consistent loop is presented in figure 3.1. The exchange correlation functional  $E_{\text{xc}}[n(\mathbf{r})]$  is generally unknown, and has to be designed to mimic the interacting system of electrons as closely as possible. Despite of this, DFT calculations give results fairly close to experimental values. This is mainly due to the exchange-correlation energy being much smaller than the other energy terms on an absolute scale [20].

#### 3.4.1 Exchange-correlation approximations

The exchange-correlation functional  $E_{\text{xc}}$  should in principle contain all of the many-body interactions of the interacting electronic system that are left out from the fictitious non-interacting system. The exchange should account for that the electronic wavefunctions  $\psi_n^{\text{ele}}(\mathbf{r}; \mathbf{R})$  change sign when two electrons are exchanged, which is a general property of fermionic systems [23]. The correlation should account for that the motion of each electron depends on the positions of the other electrons. The exchange-correlation functional should also account for the difference in kinetic energy of the interacting and non-interacting systems and that the classic Coulomb interaction term  $E_{\text{H}}$  includes that every electron interacts with itself, which needs to be removed.

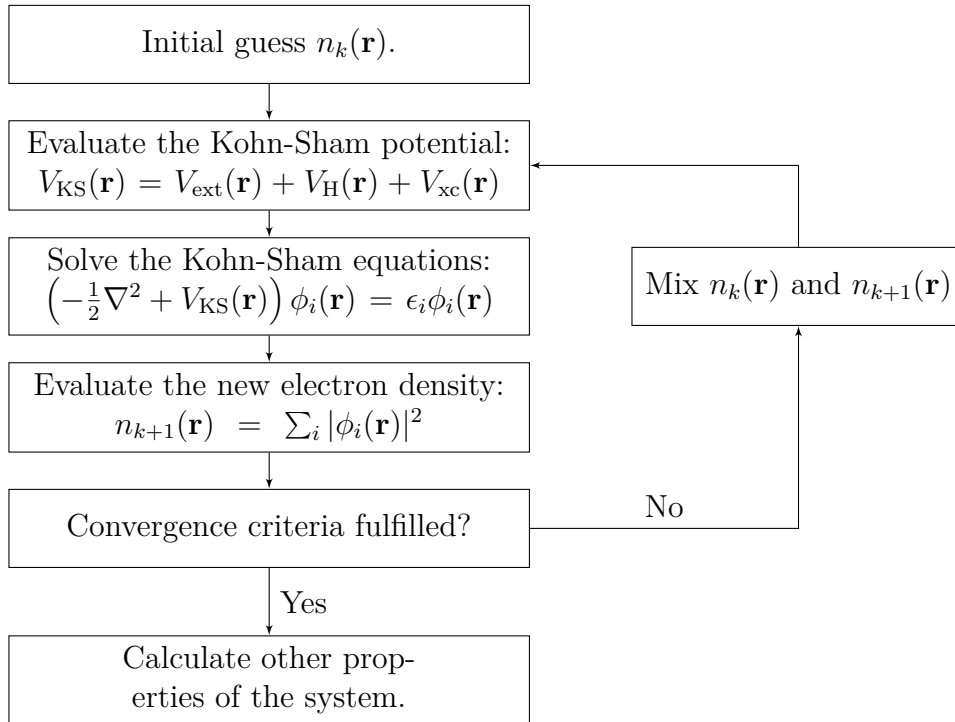


**Figure 3.1:** Self-consistent loop for determining when the electron density is converged.

There are several ways in which the exchange correlation functional can be approximated. The simplest of which is the local density approximation (LDA) [28], where the exchange-correlation is only a functional of the electron density.

$$E_{\text{xc}}^{\text{LDA}}[n(\mathbf{r})] = \int \epsilon_{\text{xc}}^{\text{LDA}}[n(\mathbf{r})]n(\mathbf{r})d\mathbf{r}$$

Here  $\epsilon_{\text{xc}}$  is the exchange-correlation energy density of the electron gas. LDA gives the exact value of  $E_{\text{xc}}$  in the limit of a homogeneous electron gas.

In a refinement of the LDA, one can consider the densities of up and down spin electrons separately, instead of the just the total density of electrons, to treat spin polarization. This is called the local spin density approximation (LSDA) [29]. Here, the exchange-correlation is a functional of both the density of up and down spin electrons.

$$E_{\text{xc}}^{\text{LSDA}}[n_{\uparrow}(\mathbf{r}), n_{\downarrow}(\mathbf{r})] = \int \epsilon_{\text{xc}}^{\text{LSDA}}[n_{\uparrow}(\mathbf{r}), n_{\downarrow}(\mathbf{r})]n(\mathbf{r})d\mathbf{r}$$

The LDA and LSDA give reasonable results for slowly varying electron gases such as metals, but give significant errors when calculating bond energies [21]. Because of this, approximations where the gradient of the electron gas is considered are needed. These approximations are called generalized gradient approximations (GGA) [30, 31], and give results much closer to the experimental values than the LDA and LSDA [32]. Here one introduces an enhancement factor  $F_{\text{xc}}$  so that the exchange-correlation functional of GGA (for one spin density) is

$$E_{\text{xc}}^{\text{GGA}}[n(\mathbf{r})] = \int \epsilon_{\text{xc}}^{\text{GGA}}[n(\mathbf{r})]F_{\text{xc}}[n(\mathbf{r}), \nabla n(\mathbf{r})]n(\mathbf{r})d\mathbf{r}.$$

One GGA functional is called PBE, named after the inventors Perdew, Burke and Ernzerhof [33]. There are also other exchange-correlation approximations that go beyond GGA and take even more effects into consideration. For example, in order to model van der Waals interactions one can add the D3 scheme to the PBE functional [34].

#### 3.4.2 Plane wave expansion of the Kohn-Sham orbitals

In an infinite lattice, one can define a primitive unit cell, with lattice parameters  $\mathbf{a}_1, \mathbf{a}_2, \mathbf{a}_3$ , as the smallest cell for which every point  $\mathbf{r}$  is equivalent to  $\mathbf{r}'$  if they fulfil the following equation [35].

$$\mathbf{r} = \mathbf{r}' + u_1\mathbf{a}_1 + u_2\mathbf{a}_2 + u_3\mathbf{a}_3, \quad u_1, u_2, u_3 \in \mathbb{Z}$$

The reciprocal space primitive vectors are defined as [35]

$$\mathbf{b}_1 = 2\pi \frac{\mathbf{a}_2 \times \mathbf{a}_3}{\mathbf{a}_1 \cdot (\mathbf{a}_2 \times \mathbf{a}_3)}, \quad \mathbf{b}_2 = 2\pi \frac{\mathbf{a}_3 \times \mathbf{a}_1}{\mathbf{a}_2 \cdot (\mathbf{a}_3 \times \mathbf{a}_1)}, \quad \mathbf{b}_3 = 2\pi \frac{\mathbf{a}_1 \times \mathbf{a}_2}{\mathbf{a}_3 \cdot (\mathbf{a}_1 \times \mathbf{a}_2)}. \quad (3.2)$$

The reciprocal lattice vectors  $\mathbf{G}$  are defined from  $\mathbf{b}_i$ .

$$\mathbf{G} = v_1\mathbf{b}_1 + v_2\mathbf{b}_2 + v_3\mathbf{b}_3, \quad v_1, v_2, v_3 \in \mathbb{Z}$$

The primitive unit cell for which the reciprocal lattice point is at the center of the cell is called the first Brillouin zone [35].

In 1928, Bloch showed that a wavefunction of an electron in a periodic potential can be written as

$$\psi_{\mathbf{k}}(\mathbf{r}) = e^{i\mathbf{k}\cdot\mathbf{r}}u_{\mathbf{k}}(\mathbf{r})$$

where the Bloch function  $u_{\mathbf{k}}(\mathbf{r})$  has the periodicity of the potential. This is known as Bloch's theorem [36]. Because of this, it is sufficient to consider only one unit cell when describing the wavefunctions of an infinite periodic system [35].

To solve the Kohn-Sham equations in practice, the Kohn-Sham orbitals have to be expanded in some basis set. For periodic structures, plane waves are often used [37]. Using Bloch's theorem, the plane wave expansion of the Kohn-Sham orbitals can be expressed as

$$\phi_j^{\mathbf{k}}(\mathbf{r}) = \sum_{\mathbf{G}} c_{j,\mathbf{k}+\mathbf{G}} e^{i(\mathbf{k}+\mathbf{G})\cdot\mathbf{r}}$$

where the summation goes over all the reciprocal lattice vectors  $\mathbf{G}$ . However, in practice the summation goes to a predetermined value, often stated in terms of cut-off energy  $E_{\text{cut-off}} = \hbar^2 (\mathbf{k} + \mathbf{G})^2 / 2$ . A higher cut-off energy means that faster variations of the Kohn-Sham orbitals are described.

#### 3.4.3 Pseudo potentials

The wavefunctions are varying rapidly close to the nucleus [38]. This means that the plane wave approach is not viable close to the nuclei. To deal with this, one can

use pseudo potentials to describe the interactions between the valence electrons and the core.

One such pseudo potential approach is the projector augmented-wave method (PAW) [38], where the core electrons are frozen. The valence electron wavefunctions are linearly transformed into pseudo wavefunctions using Kohn-Sham orbitals of isolated atoms as a basis. The transformation operator transforms the wavefunctions inside of spheres close to every nuclei, whereas the identity transform is used outside of the spheres. The pseudo wavefunctions closely resemble atomic wavefunctions inside of the spheres, while they are equal to the Kohn-Sham orbitals outside the spheres. The pseudo wavefunctions are continuous and have a continuous derivative at the interface of the spheres.

#### 3.4.4 Sampling the first Brillouin zone

The electron density in an infinite periodic system is obtained by integrating the square modulus of all of the occupied Kohn-Sham orbitals over the first Brillouin zone. Direct integration is, however, not computationally possible. One can instead sample the wavefunctions at specific  $\mathbf{k}$ -points of the Brillouin zone [37]. This gives the following expression for the electron density [39].

$$n(\mathbf{r}) = \sum_{\mathbf{k} \in 1\text{BZ}} \omega_{\mathbf{k}} \sum_j f_j^{\mathbf{k}} |\phi_j^{\mathbf{k}}(\mathbf{r})|^2$$

The first sum is over the selected points  $\mathbf{k}$  in the first Brillouin zone and the second sum is over all of the occupied Kohn-Sham orbitals.  $\omega_{\mathbf{k}}$  are weight factors proportional to the number of equivalent points in the first Brillouin zone, the sum of all weight factors is normalized to 1.  $f_j^{\mathbf{k}}$  is the occupation number of Kohn-Sham orbital  $\phi_j^{\mathbf{k}}(\mathbf{r})$  at point  $\mathbf{k}$ . It is usually preferred to select points of high symmetry, such as the center of the first Brillouin zone, named the  $\Gamma$ -point.

It is clear from equation (3.2) that the size of the reciprocal unit cell is inversely proportional to the size of the real space unit cell. Because of this, having a large unit cell in real space will decrease the number of required  $\mathbf{k}$ -points to obtain convergence [39]. Thus, instead of increasing the number of  $\mathbf{k}$ -points, it is possible to use a larger unit cell to obtain convergence.



# 4

## Calculating zeolite properties

In this chapter, the approaches on how to obtain different properties from the DFT calculations are presented.

### 4.1 Obtaining atomic structures

It is not only the electron density that needs to be relaxed, but also the positions of the nuclei. This is done by treating the nuclei classically, where the force on nuclei  $k$  can be expressed as

$$\mathbf{F}_k = -\frac{\partial E}{\partial \mathbf{R}_k}. \quad (4.1)$$

To obtain these forces, the Hellmann-Feynman theorem is used. It states that the gradient in energy  $E_\lambda$  with respect to some parameter  $\lambda$  is the expectation value of the gradient of the Hamiltonian  $\hat{H}_\lambda$  of the system with respect to  $\lambda$  [40, 41].

$$\frac{\partial E_\lambda}{\partial \lambda} = \left\langle \psi_\lambda \left| \frac{\partial \hat{H}_\lambda}{\partial \lambda} \right| \psi_\lambda \right\rangle$$

Here  $\psi_\lambda$  is an eigenfunction of the Hamiltonian  $\hat{H}_\lambda$ , which depends on  $\lambda$ .

When applying this theorem to DFT calculations, the parameter  $\lambda$  is set as the coordinate of nuclei  $k$ . Within the Born-Oppenheimer approximation, the force on nuclei  $k$ , with atomic number  $Z_k$ , is obtained by the following equation [42].

$$\mathbf{F}_k = -\frac{\partial E}{\partial \mathbf{R}_k} = -\left\langle \psi \left| \frac{\partial \hat{H}}{\partial \mathbf{R}_k} \right| \psi \right\rangle = \int \frac{Z_k(\mathbf{r} - \mathbf{R}_k)}{|\mathbf{r} - \mathbf{R}_k|^3} n(\mathbf{r}) d\mathbf{r} + \sum_{k \neq m} \frac{Z_k Z_m (\mathbf{R}_k - \mathbf{R}_m)}{|\mathbf{R}_k - \mathbf{R}_m|^3}$$

Here the sum in the second term is over all of the other nuclei in the unit cell.

For a converged electron density  $n(\mathbf{r})$ , the forces on each nuclei can be calculated. The nuclei are thereafter moved according to some algorithm, for example the conjugate gradient method [43]. The electron density is recalculated with updated atomic positions. This is done until some convergence criteria is fulfilled, for example the largest force on a nuclei not exceeding a certain value.

### 4.2 Vibrational frequencies

The vibrational frequencies of the counter ion-NH<sub>3</sub> complexes were needed for calculating various properties of the systems. For example the zero-point correction of

the energies obtained in the DFT calculations (section 4.3.1), the stretch frequency shift of a  $\text{H}^+$  counter ion bound to an O atom of a zeolite on CO adsorption (section 4.3.2) and the vibrational entropy of the Cu-NH<sub>3</sub> complexes (section 4.6.2). Here the general theory of calculating the frequencies is presented, followed by a discussion on how to distinguish between the vibrational, rotational and translational frequencies for the complexes in the zeolites.

### 4.2.1 Derivation of frequencies in an atomic structure

Consider the energy of a system  $E(\mathbf{R})$ , which can be expanded around the energy of the system at equilibrium  $E(\mathbf{R}_0)$  [44, 45]. An  $N$  body system has  $3N$  degrees of freedom in total, so there are  $3N$  ways in which the nuclei can be displaced.

$$E(\mathbf{R}) = E(\mathbf{R}_0) + \sum_k^{3N} \left. \frac{\partial E}{\partial R_k} \right|_{\mathbf{R}_0} \Delta R_k + \frac{1}{2} \sum_k^{3N} \sum_m^{3N} \left. \frac{\partial^2 E}{\partial R_k \partial R_m} \right|_{\mathbf{R}_0} \Delta R_k \Delta R_m + \mathcal{O}((\Delta R)^3)$$

Here  $\Delta R$  are small displacements from the equilibrium  $\mathbf{R}_0$ . Within a harmonic approximation, terms of order three and higher are neglected. Notice that  $E(\mathbf{R}_0)$  is constant and that the first order derivatives are zero since the energy is expanded around equilibrium.

What remains is the sum of second order derivatives. One can from the second order derivatives construct a  $3N \times 3N$  Hessian matrix  $\mathbf{H}$ . Each matrix element  $H_{k,m}$  can be interpreted as a force constant between two coordinates  $R_k$  and  $R_m$  [44]. Using equation (4.1), one can relate the energy of the system to force component  $F_k$  on nuclei  $k$  in the direction of  $R_m$ .

$$H_{k,m} := \left. \frac{\partial^2 E}{\partial R_k \partial R_m} \right|_{\mathbf{R}_0} = - \left. \frac{\partial F_k}{\partial R_m} \right|_{\mathbf{R}_0}$$

The matrix elements can be approximated using the finite difference method by displacing each nuclei in all three dimensions and evaluating the force components on them.

From the above analysis, the equation of motion for this  $3N$ -dimensional system, within a harmonic approximation, can be written as follows [44].

$$\frac{d^2 \mathbf{R}}{dt^2} = -\mathbf{A} \mathbf{R}$$

Here  $A_{k,m} = H_{k,m}/M_k$  is a one over mass-weighted Hessian matrix element with  $M_k$  being the mass of nuclei  $k$ . The obtained eigenvalues when diagonalizing the mass-weighted Hessian matrix are the eigenfrequencies  $\omega_k$  of the nuclei squared. The eigenenergies are [45]

$$E_{k,n} = \hbar \omega_k \left( n + \frac{1}{2} \right), \quad n \in \mathbb{N}.$$

### 4.2.2 Vibrational frequencies in the zeolites

The vibrational frequencies were needed for the zero-point correction energy (section 4.3.1), the stretch frequency shift of OH on CO adsorption (section 4.3.2), and the vibrational entropy of the Cu-NH<sub>3</sub> complexes (section 4.6.2).

During the simulations, the zeolites were constrained so that only the frequencies of the counter ion-NH<sub>3</sub> complexes were calculated. This was done because calculating all the frequencies of the zeolites would have been too time consuming. However, this is not a serious approximation as the frequency changes of the zeolites are negligible when an NH<sub>3</sub> molecule is adsorbed [7].

In the case of a free linear  $N$  atomic complex, there are  $3N - 5$  vibrational frequencies, while in the case of a free non-linear  $N$  atomic complex there are  $3N - 6$  [45]. This is because there are three translational and two rotational frequencies in the first case, while there are three translational and three rotational frequencies in the second case. However, when a complex is adsorbed to a zeolite surface, the situation becomes trickier. All the translational and rotational modes are now constrained to something between their free versions and vibrational modes. In the case of only one atom being adsorbed to a zeolite surface, there is one pure vibrational frequency corresponding to moving orthogonally to the zeolite surface. It is this stretch frequency that is considered for the H<sup>+</sup> counter ion in section 4.3.2.

To keep things consistent, it was decided not to include the pseudo rotational/vibrational and translational/vibrational frequencies when calculating the zero-point correction energy and the vibrational entropy. Otherwise there would be a huge difference in vibrational entropy between a complex adsorbed to a zeolite surface and one that is not. The complex not adsorbed would make up for it in rotational and translational entropy, but they are complicated to evaluate in the zeolites and are not considered here [46]. In the case of the zero-point correction, the rotational and translational frequencies are not important, as their energy contribution is small. This means that the adsorption energies are virtually the same independent of how the rotational and translational frequencies are treated.

## 4.3 Acquiring the adsorption energies of NH<sub>3</sub>

The adsorption energies of NH<sub>3</sub> were calculated as

$$\Delta E_{\text{ads}} = E_{\text{S+NH}_3} - (E_{\text{S}} + E_{\text{NH}_3}).$$

Here  $E_{\text{S+NH}_3}$  is the ground state energy of a system with an NH<sub>3</sub> molecule adsorbed,  $E_{\text{S}}$  is the ground state energy of the same system without the NH<sub>3</sub> molecule adsorbed and  $E_{\text{NH}_3}$  is the ground state energy of a gas phase NH<sub>3</sub> molecule. The calculated adsorption energies are sequential. For example, the adsorption energy of the fourth NH<sub>3</sub> molecule in a zeolite is calculated with respect to the same zeolite with three NH<sub>3</sub> molecules adsorbed.

The dissociation energies of H<sub>2</sub>O into OH and H, were calculated as

$$\Delta E_{\text{dis}} = E_{\text{S+OH+H}} - E_{\text{S+H}_2\text{O}}.$$

Here  $E_{\text{S+OH+H}}$  is the ground state energy of a system with an OH molecule and a H atom adsorbed and  $E_{\text{S+H}_2\text{O}}$  is the ground state energy of the same system with a H<sub>2</sub>O molecule adsorbed. A negative dissociation energy means that dissociation of H<sub>2</sub>O is energetically favourable.

For all of the different configurations, many different starting positions of the NH<sub>3</sub> and H<sub>2</sub>O molecules and counter ions were tested, for the systems then to be relaxed. The lowest acquired ground state energy was selected to calculate the adsorption and dissociation energies with.

### 4.3.1 Zero-point correction of ground state energies

A consequence of Heisenberg's uncertainty principle is that every quantum system fluctuates even in its ground state [47]. The vibrational energy of a system of atoms with  $N_{\text{vib}}$  vibrational modes is the sum of all vibrational eigenenergies.

$$E_{\text{vib}} = \sum_k^{N_{\text{vib}}} E_{k,n} = \sum_k^{N_{\text{vib}}} \hbar\omega_k \left( n_k + \frac{1}{2} \right), \quad n_k \in \mathbb{N}$$

The lowest possible vibrational energy is obtained for all  $n_k = 0$ , that is

$$E_{\text{vib-GS}} = \sum_k^{N_{\text{vib}}} \frac{\hbar\omega_k}{2}.$$

This term was added to the corresponding ground state energy of each system as a zero-point correction.

### 4.3.2 Comparison to OH frequency shift on CO adsorption

The Brønsted acidity of a site is defined as the tendency of the site to donate a proton [13, 48]. It can be measured both by the adsorption energy of NH<sub>3</sub> of the site and the shift of the OH stretch frequency when adsorbing a CO molecule to the H<sup>+</sup> counter ion [1]. A higher adsorption energy of NH<sub>3</sub> indicates a higher acidity of the site since the proton is then easily removed and adsorbed to the NH<sub>3</sub>. The frequency shift is defined as

$$\Delta\omega_{\text{OH}} = \omega_{\text{OH}}[\text{OH}] - \omega_{\text{OH}}[\text{OH-CO}].$$

Here  $\omega_{\text{OH}}[\text{OH}]$  is the frequency without the CO molecule adsorbed and  $\omega_{\text{OH}}[\text{OH-CO}]$  the frequency with the CO molecule adsorbed. A higher shift indicates a more acidic Brønsted site as the potential well of the H<sup>+</sup> counter ion flattens out more on the CO adsorption.

Previous studies have shown that there is a linear dependence between the frequency shift of OH and the adsorption energy of NH<sub>3</sub> at a Brønsted site when changing dopant atom [49]. To verify this, the frequency shift was calculated for all four considered dopant atoms in CHA, BEA, MFI and AIPO.

## 4.4 Oxidation states of dopant atoms

The oxidation state of an atom can be closely related to the nearest neighbour bond lengths via the Bond valence sum method [50, 51]. This method is motivated empirically and is reasonably accurate for systems with limited electronic asymmetries or steric strains. For each bond a “bond valence” can be calculated as

$$S = \exp\left(\frac{R_0 - R}{b}\right).$$

Here  $R$  is the length of the bond, while  $R_0$  is determined from a reference system and  $b$  is an empirical parameter. The sum of all bond valences for an atom is equal to the oxidation state  $V$  of the atom.

$$V = \sum_i S_i = \sum_i \exp\left(\frac{R_0 - R_i}{b}\right) \quad (4.2)$$

$R_0$  represents the bond length for which a bond valence is equal to one. It can be solved from equation (4.2) as

$$R_0 = b \ln\left(\frac{V}{\sum_i \exp(-R_i/b)}\right). \quad (4.3)$$

What remains is to obtain the value of  $b$ . It has however been determined to 0.37 Å for most types of bonds and is usually set to this value [50].

If one first applies equation (4.3) to a system where both the oxidation state and bond lengths of an atom are known,  $R_0$  can be determined. Then the oxidation state of the same atom in a system with similar kinds of bonds can be determined from equation (4.2). This was done for all considered dopant atoms in CHA, BEA, MFI and AIPO to determine the oxidation states of the dopant atoms when there are no counter ions in the systems. The values of  $R_0$  were calculated in the systems that had one  $H^+$  counter ion adsorbed at the dopant atom.

## 4.5 Bond orders from the electron density

The bond order reveals the strength of a bond. The higher the bond order, the stronger is the bond. However, there is no universal definition of bond order. In the atomic charge analysis method DDEC6, the bond order is defined as a rate of delocalization of electrons between two atoms [52]. This type of bond order can be calculated using the DDEC6 method, as described below [52].

Every atom is given an electron density  $n_j(\mathbf{r}_j)$  and a spin magnetization density vector  $\mathbf{m}_j(\mathbf{r}_j)$ . Here  $\mathbf{r}_j$  is the spatial coordinate with respect to the center of atom  $j$ . These atomic densities can be calculated from the total spin-polarized electron density  $n(\mathbf{r})$ , obtained from DFT calculations [53]. One of many constraints on the

#### 4. Calculating zeolite properties

---

atomic electron densities is that the sum of all of them should be approximately equal the total electron density.

$$\sum_j n_j(\mathbf{r}_j) \approx n(\mathbf{r})$$

A four-vector for each atom can be formed from the densities as

$$\mathbf{n}_j(\mathbf{r}_j) = (n_j(\mathbf{r}_j), \mathbf{m}_j(\mathbf{r}_j)).$$

Each component of this vector is then spherically averaged around the center of its corresponding atom to make the method less susceptible to change of basis set and exchange-correlation functional. The averaged vector is

$$\mathbf{n}_j^{\text{avg}}(r_j) = (n_j^{\text{avg}}(r_j), \mathbf{m}_j^{\text{avg}}(r_j)).$$

Around each electron is a region which cannot be occupied by other electrons due to exchange-correlation effects of the electrons, this region is called the exchange hole. In the DDEC6 method, the exchange holes are customized in regards to their sizes so that consistent results are obtained when calculating the bond orders. These customized holes are called dressed exchange holes.

Assuming that the dressed exchange holes are perfect Dirac delta functions, the bond order between atom  $A$  in the reference unit cell and any atom  $j$  would be equal to their contact exchange  $\text{CE}_{A,j}$ , which is defined as

$$\text{CE}_{A,j} = 2 \oint \frac{\mathbf{n}_A^{\text{avg}}(r_A) \cdot \mathbf{n}_j^{\text{avg}}(r_j)}{\mathbf{n}^{\text{avg}}(\mathbf{r}) \cdot \mathbf{n}^{\text{avg}}(\mathbf{r})} n(\mathbf{r}) d^3\mathbf{r}$$

where

$$\mathbf{n}^{\text{avg}}(\mathbf{r}) = \sum_j \mathbf{n}_j^{\text{avg}}(r_j)$$

is the sum of all spherically averaged atomic electron and magnetization density vectors.

The bond order of the bond between atom  $A$  and  $j$  has to be corrected for the dressed exchange holes not being perfect Dirac delta functions. The correction term is called  $\Lambda_{A,j}$ , which makes the bond order between atom  $A$  and  $j$

$$B_{A,j} = \text{CE}_{A,j} + \Lambda_{A,j}.$$

The correction term fulfills  $0 \leq \Lambda_{A,j} \leq \text{CE}_{A,j}$  and can be split up into three different factors as

$$\Lambda_{A,j} = \chi_{A,j}^{\text{pairwise}} \chi_{A,j}^{\text{coordination}} \chi_{A,j}^{\text{constraint}}.$$

Here  $\chi_{A,j}^{\text{pairwise}}$  considers pairwise interactions,  $\chi_{A,j}^{\text{coordination}}$  considers the coordination numbers of the atoms and  $\chi_{A,j}^{\text{constraint}}$  considers the constraints on the property

$$B_{A,A} = N_A - \frac{1}{2} \text{SBO}_A$$

of atom  $A$ . Here

$$N_A = \oint n_A(\mathbf{r}_A) d^3\mathbf{r}$$

is the number of electrons allocated to atom  $A$  and

$$\text{SBO}_A = \sum_{j \neq A} B_{A,j}$$

is the sum of all bond orders to atom  $A$ .

Bond orders were calculated in a variety of systems to find different ways of relating the bond orders to the adsorption energies of  $\text{NH}_3$ .

## 4.6 Thermodynamics from DFT calculations

DFT calculations are performed at zero temperature and pressure. The results can be related to finite temperatures and pressures by using thermodynamics. This was done to obtain phase diagrams of the  $\text{Cu}(\text{NH}_3)_x$  phases in the structures and temperature desorption curves for a few of the simulated configurations.

### 4.6.1 Partition function of molecules in an ideal gas

The partition function of a molecule at temperature  $T$  with energy levels  $E_i$  is [54]

$$z = \sum_i \exp(-E_i/k_B T).$$

Here  $k_B$  is the Boltzmann constant. In an ideal gas, one can reasonably assume that all degrees of freedom of the molecules are independent, so the partition function of each molecule can be factorized into different parts for different degrees of freedom [54]. Here translational, vibrational, rotational and electronic degrees of freedom are considered, so the partition function of each molecule takes the following form.

$$z = z_{\text{tra}} z_{\text{vib}} z_{\text{rot}} z_{\text{ele}}$$

The translational partition function can, when approximating that the molecule occupies a cube of volume  $V$ , be evaluated by

$$z_{\text{tra}} = \left( \frac{mk_B T}{2\pi\hbar^2} \right)^{3/2} V.$$

Here  $m$  is the mass of the molecule and  $\hbar$  is Planck's reduced constant [54].

The vibrational partition function within a harmonic approximation, described in section 4.2.1, is

$$z_{\text{vib}} = \prod_k \frac{\exp\left(-\frac{\hbar\omega_k}{2k_B T}\right)}{1 - \exp\left(-\frac{\hbar\omega_k}{k_B T}\right)}. \quad (4.4)$$

Here  $\omega_k$  are the vibrational eigenfrequencies of the molecule [54].

The rotational partition function differs for a linear and non-linear molecule, they are within a rigid-rotor approximation

$$z_{\text{rot}}^{\text{lin}} = \frac{1}{\sigma} \left( \frac{2k_B T}{\hbar^2} \right) I, \quad z_{\text{rot}}^{\text{non-lin}} = \frac{\sqrt{\pi}}{\sigma} \left( \frac{2k_B T}{\hbar^2} \right)^{3/2} \sqrt{I_x I_y I_z}.$$

Here  $\sigma$  is the symmetry factor of the molecule, and  $I_i$  are the moments of inertia around the principal axes of the molecule [54].

Since energies of the excited electronic states are much higher than  $k_B T$  at temperatures considered in this thesis, the electronic partition function can be approximated as

$$z_{\text{ele}} = g_0 \exp(-E_0/k_B T)$$

where  $g_0$  is a degeneracy factor and  $E_0$  is the ground state electron energy [54].

The total partition function of an ideal gas with  $N$  molecules relates to the partition function of each molecule of the gas as [54]

$$Z = \frac{1}{N!} z^N.$$

### 4.6.2 Gibbs free energy of adsorption

The Gibbs free energy is the energy needed to create a thermodynamic system in an environment at constant pressure  $P$  and temperature  $T$ . It is a function of the enthalpy  $H$ , entropy  $S$  and temperature of the system [55].

$$G = H - TS \tag{4.5}$$

In the case of  $\text{NH}_3$  molecules being adsorbed to a zeolite, the Gibbs free energy of the system is a function of pressure, temperature and number of adsorbed  $\text{NH}_3$  molecules  $N$ . The  $\text{NH}_3$  gas that the zeolite adsorbs  $\text{NH}_3$  from acts as a reservoir, so the Gibbs free energy of the gas can be expressed as a chemical potential  $\mu_{\text{NH}_3}$ .

$$G_{\text{gas}}(P, T, N) = N\mu_{\text{NH}_3}(P, T)$$

This means that the change in Gibbs free energy when a clean zeolite adsorbs  $N$   $\text{NH}_3$  molecules is [56]

$$\Delta G_{\text{ads}} = - (G(P, T, N) - G(P, T, 0) - N\mu_{\text{NH}_3}(P, T)). \tag{4.6}$$

Here  $G(P, T, N)$  is the Gibbs free energy of the zeolite with  $N$  adsorbed  $\text{NH}_3$  molecules and  $G(P, T, 0)$  is the Gibbs free energy of the same zeolite with no adsorbed molecules.

The chemical potential  $\mu$  of an ideal gas can be split into two terms of which only one depends on pressure [54].

$$\mu(P, T) = \mu(P_0, T) + k_B T \ln \left( \frac{P}{P_0} \right)$$

Here  $P_0$  is a reference pressure. Now one can fit experimental values of the enthalpy and entropy at this reference pressure and varying temperatures to obtain the chemical potential of the  $\text{NH}_3$  gas.

$$\mu_{\text{NH}_3}(P, T) = E_{\text{NH}_3} + \Delta H(P_0, T) - T\Delta S(P_0, T) + k_B T \ln \left( \frac{P}{P_0} \right)$$

Here  $\Delta H(P_0, T)$  and  $\Delta S(P_0, T)$  are the experimental values used [57] and  $E_{\text{NH}_3}$  is the ground state energy of a  $\text{NH}_3$  molecule calculated with DFT.

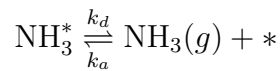
As stated in section 4.2.2, only the vibrational entropy of the complexes in the zeolites is evaluated, this is done using equation (4.4). From this, the entropy of the systems can be calculated [54].

$$S = k_B T \left( \frac{\partial \ln(Z)}{\partial T} \right)_{N,V} + k_B \ln(Z)$$

The enthalpies of the systems are approximated by the energies calculated using DFT. From this, the Gibbs free energies of the zeolites at certain pressures and temperatures can be calculated using equation (4.5). The number of adsorbed  $\text{NH}_3$  molecules that gives the lowest value of  $\Delta G_{\text{ads}}$  in equation (4.6) is the preferred phase at that pressure and temperature.

### 4.6.3 Temperature programmed desorption curves

To be able to compare the adsorption energies with experimental values, a macroscopic property that can be measured experimentally had to be calculated from the DFT simulations. One way of doing this is to calculate temperature programmed desorption (TPD) curves from the calculated adsorption energies [58, 59]. The TPD calculations were performed by considering the following reaction.



Here  $*$  is an empty adsorption site,  $\text{NH}_3^*$  is  $\text{NH}_3$  adsorbed to the zeolite and  $\text{NH}_3(g)$  is a gas molecule of  $\text{NH}_3$ .  $k_d$  is the desorption rate constant and  $k_a$  the adsorption rate constant. Assuming a mean-field approximation, the probability  $\theta$  of a binding site being covered obeys the following equation.

$$\frac{d\theta}{dt} = k_a \frac{P_g}{P_0} (1 - \theta) - k_d \theta$$

Here  $P_g$  is the pressure of  $\text{NH}_3$  in the gas phase and  $P_0$  is a reference pressure. The ratio between the desorption and adsorption rate constants is the equilibrium

constant, which can be expressed as

$$\frac{k_d}{k_a} = \exp\left(-\frac{\Delta G}{k_B T}\right) = \exp\left(-\frac{\Delta H}{k_B T}\right) \exp\left(\frac{\Delta S}{k_B}\right).$$

Here  $\Delta G$ ,  $\Delta H$  and  $\Delta S$  are the changes in Gibbs free energy, enthalpy and entropy on  $\text{NH}_3$  desorption, respectively. Assuming equilibrium between the gas phase and the adsorbed  $\text{NH}_3$ , one can obtain the gas concentration  $C_g$  of  $\text{NH}_3$  by using the ideal gas law.

$$C_g = \frac{\theta}{1 - \theta} \frac{P_0}{k_B T} \exp\left(-\frac{\Delta H}{k_B T}\right) \exp\left(\frac{\Delta S}{k_B}\right)$$

Considering mass balance between the amount of  $\text{NH}_3$  flowing into and out of the zeolite, the following equation holds.

$$F C_g = -A_0 W \frac{d\theta}{dt} = -\beta A_0 W \frac{d\theta}{dT}$$

Here  $F$  is the flow rate of the gas carrying  $\text{NH}_3$  through the zeolite,  $A_0$  is the adsorption site concentration,  $W$  is the mass of the zeolite sample and  $\beta = dT/dt$  is the heating rate. This gives a new expression for the gas concentration of  $\text{NH}_3$ .

$$C_g = -\frac{\beta A_0 W}{F} \frac{d\theta}{dT} = \frac{\theta}{1 - \theta} \frac{P_0}{k_B T} \exp\left(-\frac{\Delta H}{k_B T}\right) \exp\left(\frac{\Delta S}{k_B}\right)$$

Now the probability of a binding site being covered as a function of temperature can be obtained iteratively.

$$\theta_{i+1} = \theta_i + \left(\frac{d\theta}{dT}\right)_i \Delta T$$

From this, the gas concentration of  $\text{NH}_3$  as a function of temperature can be obtained.

The simulations were started at  $-200^\circ\text{C}$  so that virtually no molecules desorbed right at the start of the simulations. The heating rate was  $3\text{ K min}^{-1}$  and the flow rate of the carrier gas was  $3\text{ cm}^3\text{ s}^{-1}$ . Since the temperature at which the structures lose some of their catalytic capacities permanently is about  $800^\circ\text{C}$  for CHA [60],  $760^\circ\text{C}$  for BEA [61],  $600^\circ\text{C}$  for MFI [62] and  $1000^\circ\text{C}$  for AlPO [63], there is no reason to consider the TPD curves above those temperatures. One of the reasons that BEA and MFI are less hydrothermally stable than CHA and AlPO are their larger pore sizes [64].

In the case of  $\text{NH}_3$  being adsorbed to Cu counter ions, the simulations were started with four  $\text{NH}_3$  adsorbed to every ion. In the case of  $\text{NH}_3$  being adsorbed to  $\text{H}^+$  counter ions, the simulations were started with one  $\text{NH}_3$  adsorbed to every ion. The value of change of entropy on  $\text{NH}_3$  desorption was set to  $\Delta S = 150\text{ J K}^{-1}\text{ mol}^{-1}$ . This value corresponds to about 2/3 of the gas phase entropy and has been measured for various zeolites in a wide variety of conditions [59]. The change in enthalpy is just the adsorption energy of  $\text{NH}_3$ .

## 4.7 Computational setup of DFT calculations

The energy of the gas phase  $\text{NH}_3$  was calculated in a unit cell of  $15.0 \cdot 15.1 \cdot 15.2 \text{ \AA}^3$ , with one molecule per cell.

The DFT simulations were performed using the Vienna Ab-Initio Simulation Package (VASP) [65, 66, 67, 68]. The exchange-correlation functional used was spin-polarized PBE-D3 [33]. The PBE functional was used in conjunction with the D3 scheme to include van der Waals interactions [34]. The Kohn-Sham orbitals were expanded in a plane wave basis with a cut of energy of 480 eV and the valence-core interaction was treated with the PAW method. Only the  $\Gamma$ -point was sampled in reciprocal space. The convergence criteria for the electronic loop was set to  $10^{-5}$  eV.

The nuclei were relaxed by using the conjugate gradient method [43] in VASP [65], with a convergence criteria of the largest force on each nuclei not exceeding  $0.03 \text{ eV \AA}^{-1}$ . The cell parameters were kept constant during the simulations. When calculating the forces on the nuclei during the vibrational analysis, each unconstrained nuclei were displaced  $0.015 \text{ \AA}$  both ways in all three dimensions.

This VASP setup was used to be able to compare the result with reference [7], with the addition of PBE-D3 for description of van der Waals interactions, instead of PBE-cx. This change was made because previous research has shown that PBE-cx does not give a satisfactory description of the O-Cu interaction during  $\text{O}_2$  dissociation [69], which is a vital part of reaction (1.1).

The bond orders were calculated by applying the DDEC6 method in the program Chargemol [70].

All of the calculations were performed on the computational clusters Hebbe and Vera provided by C3SE for a total of 302847 computational hours.



# 5

## Results

In this chapter, the calculated adsorption energies together with TPD curves and phase diagrams are presented. The visualizations of the zeolites are restricted to the Al case, except when differences to other dopant atoms are presented. For AIPO, the visualizations are of the structures doped with Si. The threshold for an O-Cu bond is set to 2.4 Å.

### 5.1 Cell volumes of the structures

The DFT simulations were performed for the primitive unit cell in the case of BEA and MFI, while the cells with 108 atoms were used for CHA and AIPO. However, when studying the effect of dopant density in CHA in section 5.3, cells with 36 and 288 atoms were also used. The systems were periodic in all three dimensions.

For all considered structures, the cell volumes of the undoped unit cells were optimized by plotting different volumes as a function of the corresponding energy of the cell and making a second degree fit. The original cells, except for the CHA cells with 36 and 288 atoms, were taken from references [11, 12], so the fractions and angles between the cell parameters were the same as for them in all simulations. The 288 atom CHA cell is just an extension of the 36 atom cell, which was originally taken from reference [71].

The fractions of the cell parameters used in the calculations are not exactly the same as the experimental ones. However, the cell parameters should not affect the calculated adsorption energies of NH<sub>3</sub> much since the energies with and without the NH<sub>3</sub> were calculated with the same cell parameters. The energy dependence on the cell parameters should therefore cancel as long as the parameters are within a few percent of the experimental ones.

The energies of undoped CHA, BEA, MFI and AIPO for different cell volumes are presented in figure 5.1, together with second degree fits. The fitted lowest energy cell volume with corresponding parameters ( $a$ ,  $b$ ,  $c$ ) and angles ( $\angle bc$ ,  $\angle ac$ ,  $\angle ab$ ) between parameters for these unit cells and the 36 atom CHA unit cell are presented in table 5.1. A summary of cell volumes, parameters, angles between parameters from some experimental studies of CHA, BEA, MFI and AIPO are presented in table 5.2.

## 5. Results

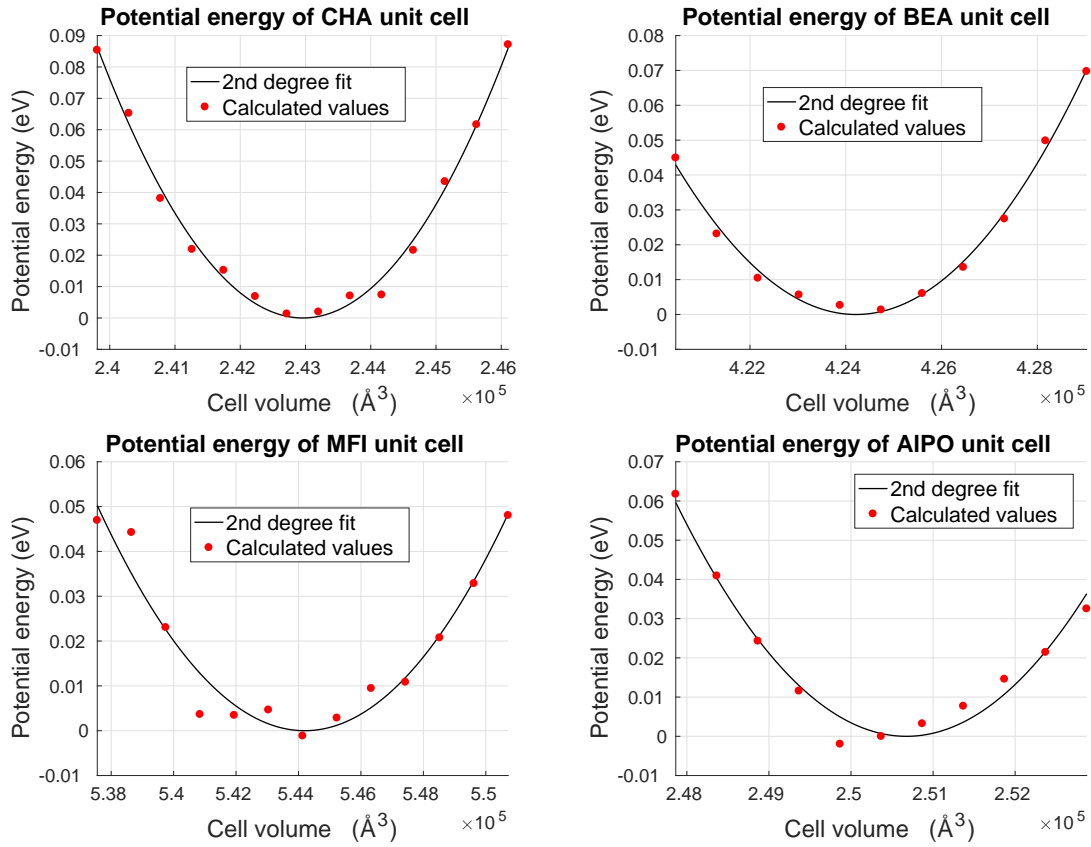


**Figure 5.1:** Energy as a function of cell volume for CHA, BEA, MFI and AIPO.

**Table 5.1:** Properties of the fitted lowest energy unit cells of CHA-36, CHA-108, BEA, MFI and AIPO.

	Volume ( $\text{\AA}^3$ )	$a$ ( $\text{\AA}$ )	$b$ ( $\text{\AA}$ )	$c$ ( $\text{\AA}$ )	$\angle bc$	$\angle ac$	$\angle ab$
CHA-36	808.91	9.344	9.344	9.344	94.2°	94.2°	94.2°
CHA-108	2429.6	13.64	13.64	15.08	90.0°	90.0°	120.0°
BEA	4242.1	12.65	12.65	26.50	90.0°	90.0°	90.0°
MFI	5442.0	20.29	19.94	13.46	90.0°	90.0°	90.0°
AIPO	2506.8	13.88	13.88	15.02	90.0°	90.0°	120.0°

**Table 5.2:** Properties of experimentally measured unit cells of CHA-36, CHA-108, BEA, MFI and AIPO.

	Volume ( $\text{\AA}^3$ )	$a$ ( $\text{\AA}$ )	$b$ ( $\text{\AA}$ )	$c$ ( $\text{\AA}$ )	$\angle bc$	$\angle ac$	$\angle ab$	Ref.
CHA-36	823.5	9.40	9.40	9.40	94.2°	94.2°	94.2°	[10]
CHA-108	2470.6	13.77	13.77	15.04	90.0°	90.0°	120.0°	[10]
BEA	4159	12.6	12.6	26.2	90.0°	90.0°	90.0°	[72]
BEA	4156	12.5	12.5	26.6	90.0°	90.0°	90.0°	[73]
MFI	5365.2	20.07	19.92	13.42	90.0°	90.0°	90.0°	[74]
MFI	5309.2	19.92	19.96	13.36	90.0°	90.0°	90.0°	[75]
AIPO	2435.3	13.72	13.72	14.93	90.0°	90.0°	120.0°	[76]

The calculated lowest energy CHA cell with 108 atoms in table 5.1 is within 0.12% of three times the volume of the 36 atom cell. This mainly comes down to rounding errors and the limited number of tested volumes giving room for some uncertainty. However, all of the calculated lowest energy cell parameters are in close proximity with experimentally measured cell parameters. There are clear differences between the experimental cell parameters for BEA and MFI from the different references. The differences probably stem from there being different ratios of Si/dopant atoms in the experimental cells, while there are no dopant atoms in the calculated lowest energy cells. Another uncertainty stems from the fact that the experimental zeolites probably contain H<sub>2</sub>O [10].

## 5.2 Investigated dopant configurations

The CHA, BEA and MFI zeolites were all doped with either Al, B, Fe or Ga, while AlPO was doped with Si or Ti when replacing P and Mg or Zn when replacing Al. In the case of having one dopant atom in the unit cell, H<sup>+</sup>, Cu(I) and Cu(II) bound to (OH)<sup>-</sup> were used as counter ions. For H<sup>+</sup>, adsorption of one NH<sub>3</sub> molecule was considered, while for Cu(I) up to four NH<sub>3</sub> and for Cu(II) with (OH)<sup>-</sup> up to three NH<sub>3</sub> were considered. In the case of having two dopant atoms in the cell, Cu(II) with up four NH<sub>3</sub> was considered. This was done for all eight types of dopant atoms.

In CHA, all Si positions are equivalent. Thus, the position of the dopant atom is irrelevant when there is only one. Only one distribution of two dopant atoms was tested for B, Fe and Ga, opposite each other in a six-membered ring, while 17 were tested for Al. The CHA unit cell with the two dopant positions tested for all four dopant atoms is visualized in figure 5.2. The 17 different dopant distributions in Al doped CHA are presented in section 5.7.

For AlPO, all positions of one dopant atom are also equivalent, while in the configuration with two dopant atoms they were both placed in two of the three possible positions in a six-membered ring. The unit cell with two dopant atoms that was used for Si and Ti is visualized in figure 5.3. When doping with Mg and Zn, the positions were the same, but with the positions of Al and P exchanged.

For BEA and MFI, only some positions of Si atoms are equivalent. In the case of there only being one dopant atom, a site of high symmetry was chosen in BEA and the most kinetically active site was chosen in MFI [77]. The second dopant atoms were positioned so that the configurations should resemble two dopant atoms opposite each other in a six-membered ring in CHA. Because of the high number of atoms in the unit cells of BEA and MFI, it could take a couple of days to relax the structures running on one computational node. To decrease the required computational time, atoms far away from the reaction sites were constrained. In resemblance to the cell volume discussion in section 5.1, the constraints should have a low effect on the adsorption energies of NH<sub>3</sub>. The BEA and MFI unit cells with two Al dopant atoms are visualized in figure 5.4 and 5.5, respectively.

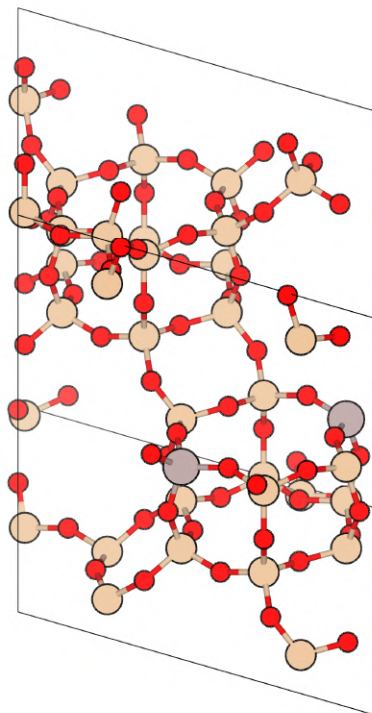


**Figure 5.2:** Positions of Al dopant atoms in the CHA unit cell. The left Al atom was used when only having one dopant atom.

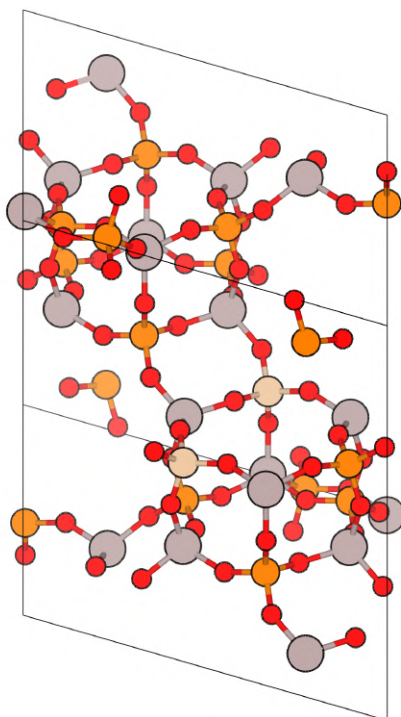


**Figure 5.3:** Positions of Si dopant atoms in the AIPO unit cell. The left Si atom was used when only having one dopant atom.

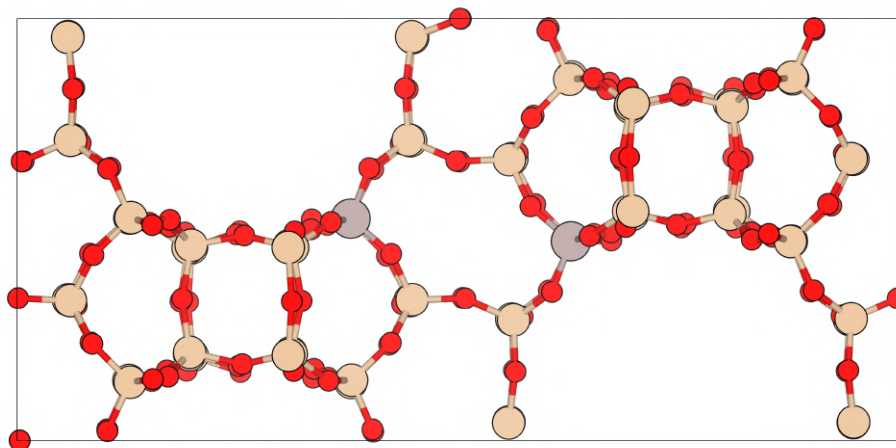


**Figure 5.4:** Positions of Al dopant atoms in the BEA unit cell. The right Al atom was used when only having one dopant atom.

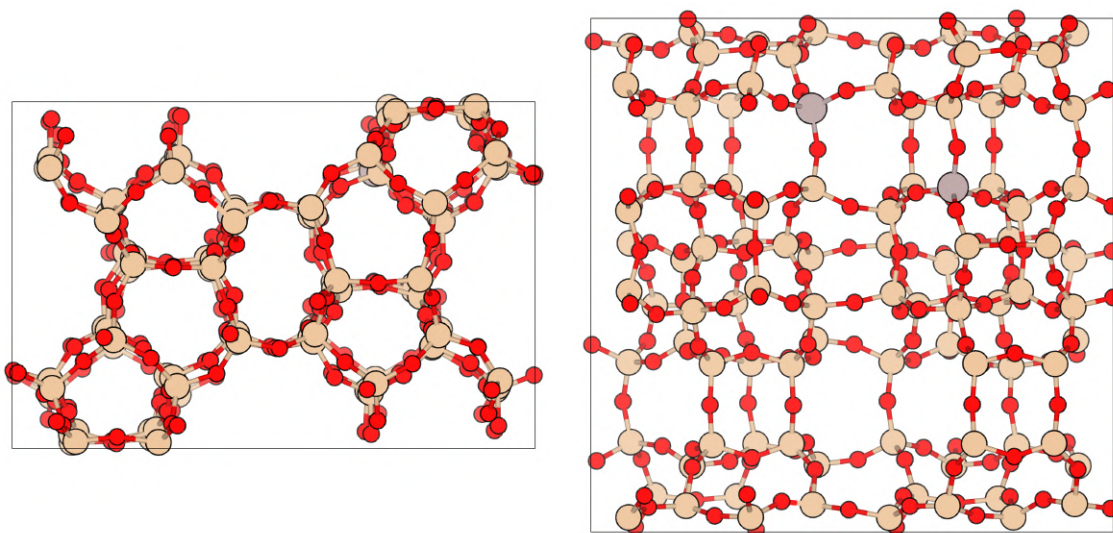


**Figure 5.5:** Two views of the positions of Al dopant atoms in the MFI unit cell. The right Al atom was used when only having one dopant atom.

### 5.3 $\text{NH}_3$ adsorption at Brønsted sites

The adsorption energies of  $\text{NH}_3$  at the lowest energy Brønsted sites were calculated for CHA, BEA, MFI and AIPO with four types of dopant atoms. The site is the same for all dopant atoms within all zeolite frameworks, except for B doped MFI having a different site than the other MFI zeolites. The lowest energy Brønsted sites in CHA, BEA and MFI with Al as a dopant atom and AIPO with Si as a dopant atom are presented in figure 5.6. The same configurations, but with one  $\text{NH}_3$  adsorbed to the Brønsted sites are presented in figure 5.7.

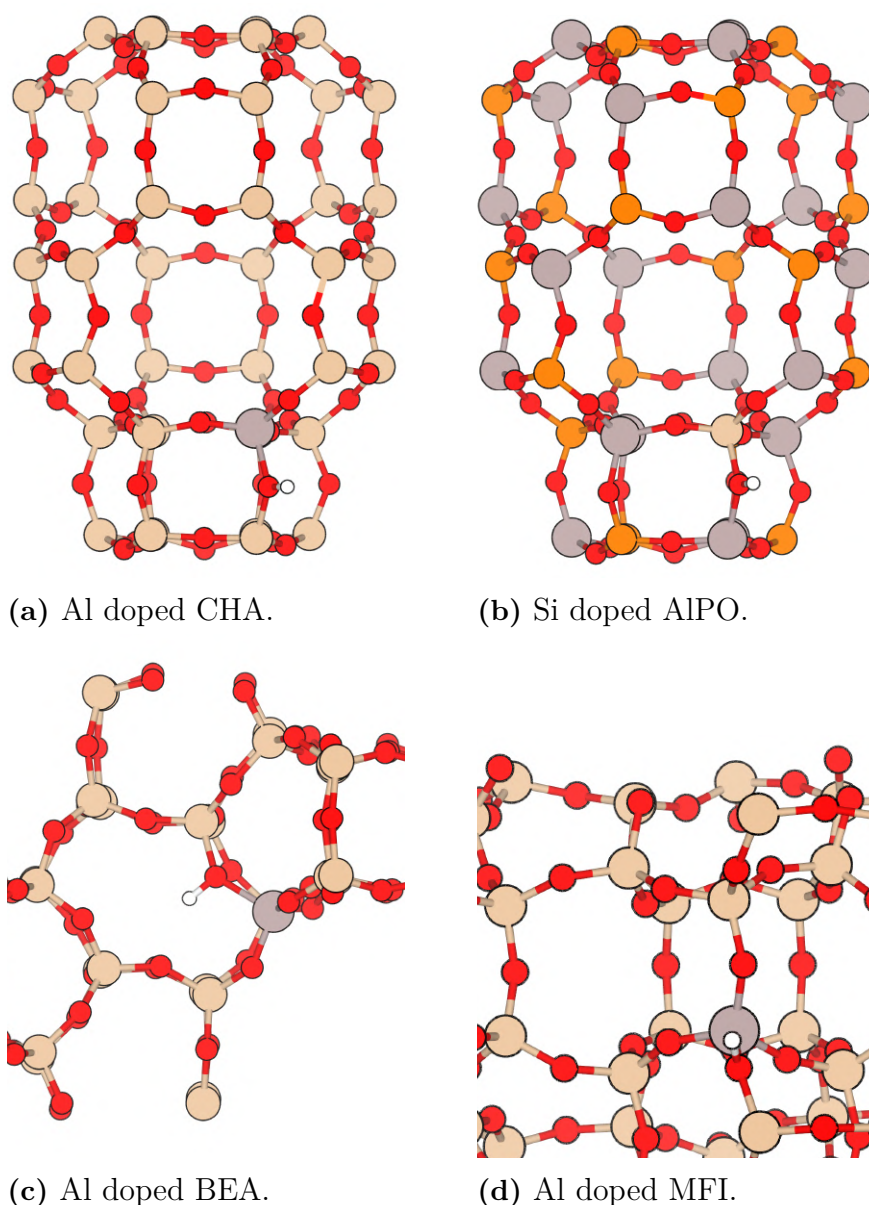


**Figure 5.6:** The lowest energy Brønsted sites in Al doped CHA, BEA and MFI and Si doped AIPO.

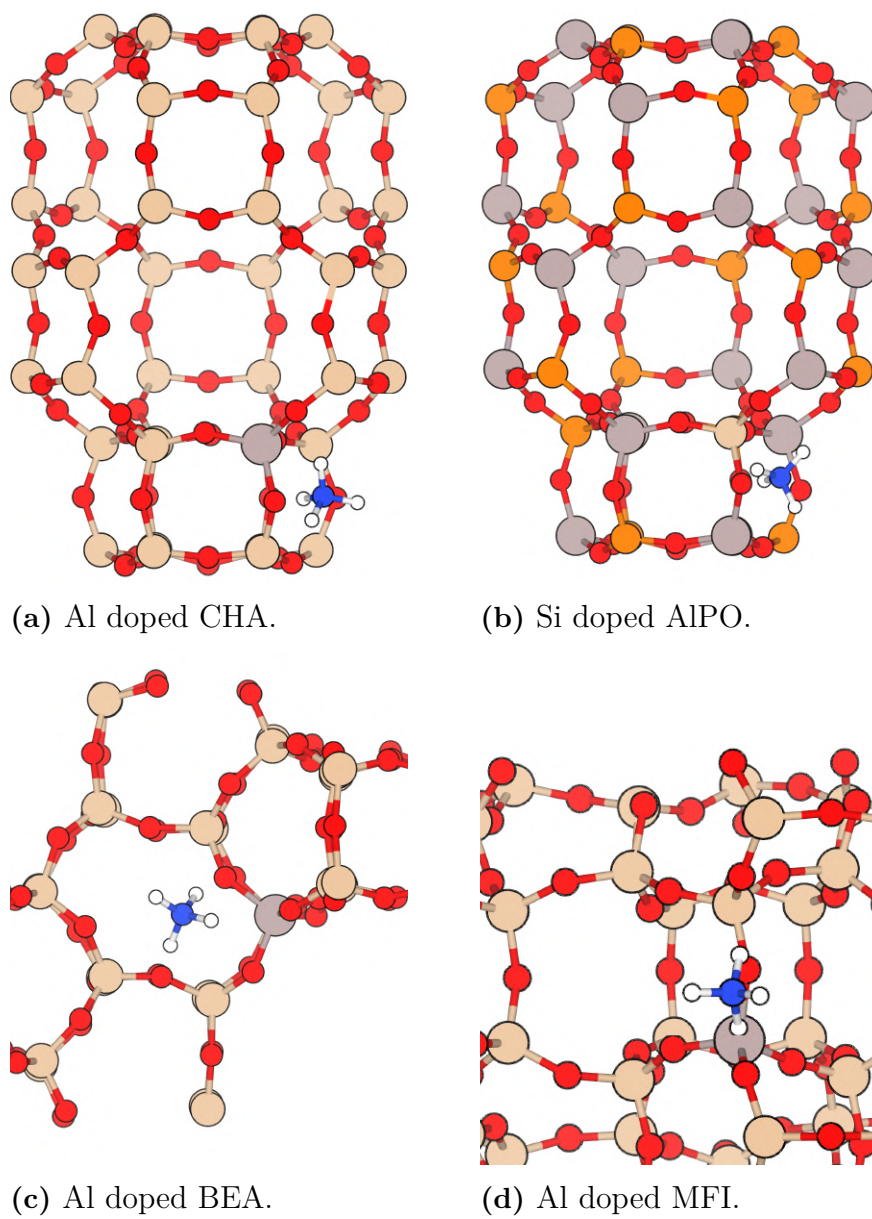


**Figure 5.7:**  $\text{NH}_3$  adsorbed to the lowest energy Brønsted sites in Al doped CHA, BEA and MFI and Si doped AIPO.

The lowest energy Brønsted site in B doped MFI is at the O atom left of the dopant atom, from the same perspective as in figure 5.6d. The difference probably comes from this O atom being able to distance itself further away from the B dopant atom when  $H^+$  is adsorbed, than the O atom that has the lowest energy Brønsted site for the other dopant atoms. The O atoms of the Brønsted sites break the bond to the B dopant atom in all zeolites, but not the other dopant atoms. Thus, having a long O-B distance is energetically preferable in B doped structures with a  $H^+$  counter ion adsorbed.

The values of the adsorption energies at the preferred Brønsted sites are presented in table 5.3. The second column states the Si/dopant ratios for the zeolites and the (Al+P)/dopant ratio for AIPO. The standard CHA unit cell of 108 atoms has a ratio of 35, while the other cells have ratios of 11 and 95.

**Table 5.3:** The adsorption energy of  $NH_3$  at the lowest energy Brønsted sites in CHA, BEA, MFI and AIPO with four different kinds of dopant atoms.

	Ratio	$E_{ads}^{Al}$	$E_{ads}^{Ga}$	$E_{ads}^{Fe}$	$E_{ads}^B$	(eV)
CHA	11	-1.54	-1.45	-1.35	-0.95	
CHA	35	-1.49	-1.41	-1.31	-0.91	
CHA	95	-1.47	-1.42	-1.32	-0.91	
MFI	95	-1.43	-1.35	-1.28	-0.91	
BEA	63	-1.23	-1.12	-1.03	-0.86	

	Ratio	$E_{ads}^{Mg}$	$E_{ads}^{Zn}$	$E_{ads}^{Si}$	$E_{ads}^{Ti}$	(eV)
AIPO	35	-1.62	-1.49	-1.36	-1.18	

For all three zeolites, the order of dopant atoms is Al, Ga, Fe to B when going from highest to lowest adsorption energy. This means that the B dopant atom gives the least acidic, while Al gives the most acidic Brønsted sites of the dopant atoms tested. As stated in section 4.3.2, a higher acidity of the site indicates that the proton is easily removed from the zeolite and adsorbed to the  $NH_3$ . This means that if a  $H^+$  counter ion is tightly bound to an O atom, it should have a high bond order to that atom, and induce a low adsorption energy of  $NH_3$ . The relationships between the adsorption energies of  $NH_3$  and the bond orders of the O-H bonds are presented in section 5.3.1.

For all dopant atoms, CHA-11 has the highest and BEA the lowest adsorption energies. Therefore, the position of the dopant atoms in the BEA cell is the least acidic, while the position in the CHA-11 cell is the most acidic. The differences between different zeolite frameworks stem from the long range van der Waals forces being different. In BEA, the lowest energy position of  $H^+$  is in the six-membered ring. When  $NH_3$  is adsorbed, it cannot fit in the ring, so the  $(NH_4)^+$  complex has its lowest energy position outside the ring. This is less energetically favourable than in CHA and MFI, where  $(NH_4)^+$  is not far displaced from the lowest energy  $H^+$  positions.

It is clear that CHA-11 has more acidic Brønsted sites than CHA-35 and CHA-95, so a higher dopant concentration gives higher Brønsted site acidity. The small differences in the adsorption energies of CHA-35 and CHA-95 is probably due to the dopant concentration influence on the acidity being saturated at such low concentrations. Previous studies also show that the adsorption energy increases for a higher dopant density [7, 78, 79].

### 5.3.1 Comparison to O-H bond order

The bond orders of the O-H bonds of the lowest energy Brønsted sites without  $\text{NH}_3$  adsorbed were compared to the adsorption energies of  $\text{NH}_3$  on the same sites. Here the same Brønsted site was used for B doped MFI as for the other dopant atoms to be able to compare the results. The values for the considered dopant atoms in CHA, BEA and MFI, together with linear fits and  $R^2$  values, are presented in figure 5.8.

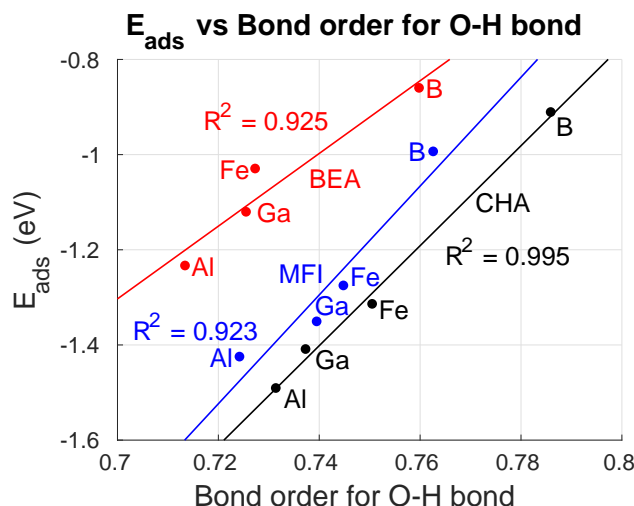


**Figure 5.8:** Adsorption energy of  $\text{NH}_3$  as a function of bond order of the O-H bond without  $\text{NH}_3$  adsorbed, when exchanging dopant atom in CHA, BEA and MFI.

The relationships are fairly well described by the linear fits, with  $R^2$  values of 0.995, 0.925 and 0.923. As visualized in figure 5.8, no correlation was found between the different zeolite frameworks. The results can be qualitatively explained by that a tighter O-H bond imply a higher bond order and that the  $\text{H}^+$  counter ion is harder to remove from the zeolite surface, which induces a lower  $\text{NH}_3$  adsorption energy.

### 5.3.2 Oxidation states of dopant atoms

It is assumed that the dopant atoms have oxidation states of +3 in CHA, BEA and MFI, while Mg and Zn have +2 and Si and Ti have +4 in AlPO, when a  $\text{H}^+$  counter ion is adsorbed to a nearby O. From this, the oxidation states when a counter ion is not present could be calculated according to the Bond valence sum method in section 4.4. The calculated oxidation states are presented in table 5.4.

**Table 5.4:** Oxidation states of dopant atoms in CHA, BEA, MFI and AIPO without any counter ion adsorbed.

	Al	B	Ga	Fe
CHA	+3.10	+3.07	+3.11	+4.11
BEA	+3.11	+3.07	+3.09	+3.79
MFI	+3.10	+3.07	+3.08	+4.00

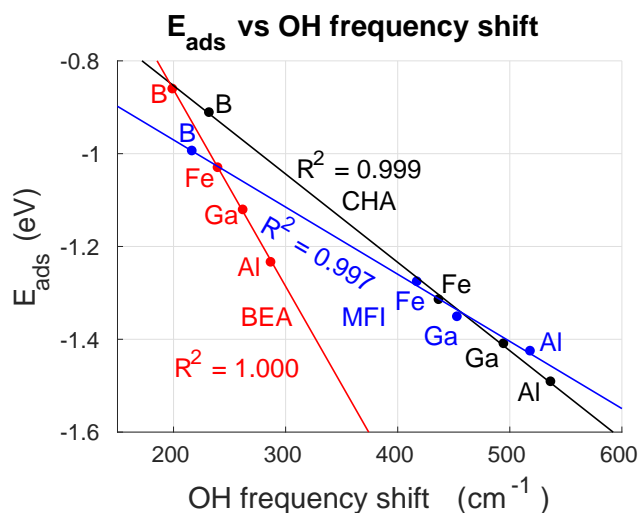
  

	Mg	Zn	Si	Ti
AIPO	+2.11	+2.25	+4.13	+4.10

All dopant atoms, except Fe, are at their maximum oxidation states when the  $H^+$  counter ion is present, so their oxidation states do not change much without a counter ion present. Fe can take an oxidation state of up to +7, so it changes to approximately +4 when the counter ion is removed, filling the role of Si.

### 5.3.3 Comparison to OH frequency shift on CO adsorption

The OH stretch frequency shifts when introducing a CO molecule were compared to the adsorption energies of  $NH_3$  as a mean of determining the acidity of the Brønsted sites. Here the same Brønsted site was also used for B doped MFI as for the other dopant atoms to be able to compare the results. The relationships between the frequency shifts and adsorption energies for the considered dopant atoms in CHA, BEA and MFI are presented in figure 5.9, together with linear fits and  $R^2$  values of the fits.



**Figure 5.9:** Adsorption energy of  $NH_3$  as a function of OH stretch frequency shift when introducing a CO molecule at Brønsted sites, when exchanging dopant atom in CHA, BEA and MFI.

The linear fits are very good, with  $R^2$  values of 0.999, 1.000 and 0.997. This is in good agreement with previous studies [49]. No correlation is found between different zeolite frameworks. The reason for the difference in frequency shift between different

dopants being smaller in BEA, than in the two other zeolites, is probably that the  $H^+$  counter ion is moved from its lowest energy position, when CO is introduced. The counter ion moves because CO does not fit into the six-membered ring, where  $H^+$  has its lowest energy position. A comparison was also made for AIPO, but it was found that the method is not applicable since either Al or P atoms are replaced. By testing more than two dopant atoms replacing the same atom, the method might be applicable also in AIPO.

The structures with CO adsorbed to the lowest energy Brønsted sites for Al doped CHA, BEA and MFI and Si doped AIPO are presented in figure 5.10.

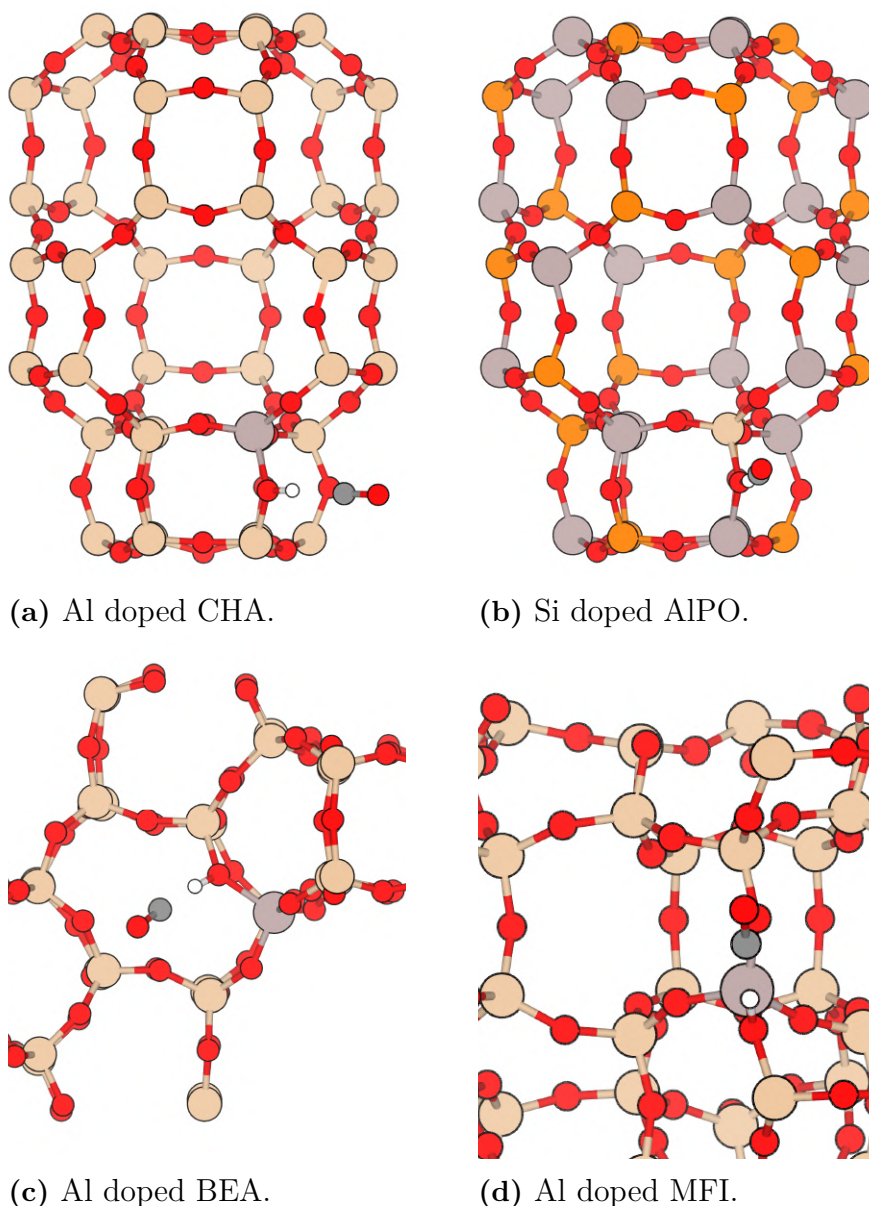


**Figure 5.10:** CO adsorbed to the lowest energy Brønsted sites in Al doped CHA, BEA and MFI and Si doped AIPO.

### 5.3.4 TPD curves for Brønsted site desorption

TPD curves for  $\text{NH}_3$  desorption from the lowest energy Brønsted sites in all considered structures are presented in figure 5.11.

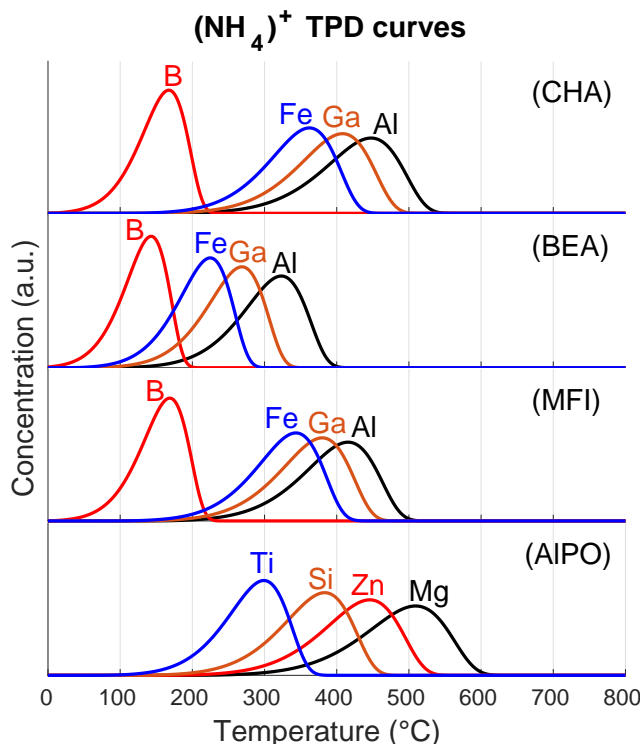


**Figure 5.11:** TPD curves for  $\text{NH}_3$  desorption from the lowest energy Brønsted sites in CHA, BEA, MFI and AIPO for all considered dopant atoms.

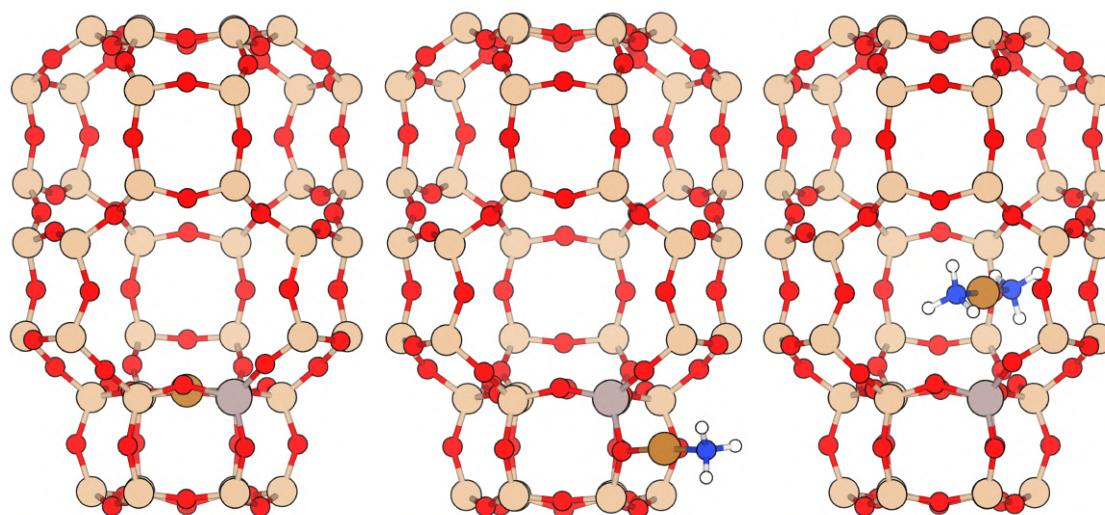
As expected, a higher adsorption energy corresponds to a TPD peak at a higher temperature. Among the zeolites, Al doped CHA can store  $\text{NH}_3$  at highest temperatures, while Mg doped AIPO has an even higher capability.

Experimental studies have assigned TPD peaks at about 420 °C, 340 °C, 380 °C and 400 °C to desorption from Brønsted sites in Al doped CHA, BEA and MFI and Si doped AIPO, respectively [7, 80, 81, 82]. However, for BEA, MFI and AIPO the experimental heating rates were 10 K min<sup>-1</sup>, instead of 3 K min<sup>-1</sup> and for BEA and MFI the experimental flow rate of the carrier gas was 0.6 cm<sup>3</sup> s<sup>-1</sup>, instead of 3 cm<sup>3</sup> s<sup>-1</sup>. This shifts the experimental TPD peaks for BEA and MFI about 100 K towards higher temperature, which makes especially the MFI curves not correspond. However, the dopant positions probably not being the same in the simulated and experimental configurations influences the results for BEA and MFI, since very few Si positions are equivalent there. For CHA and AIPO, the experimental results are in reasonable agreement with the TPD curves presented in figure 5.11.

## 5.4 $\text{NH}_3$ adsorption on Cu(I)

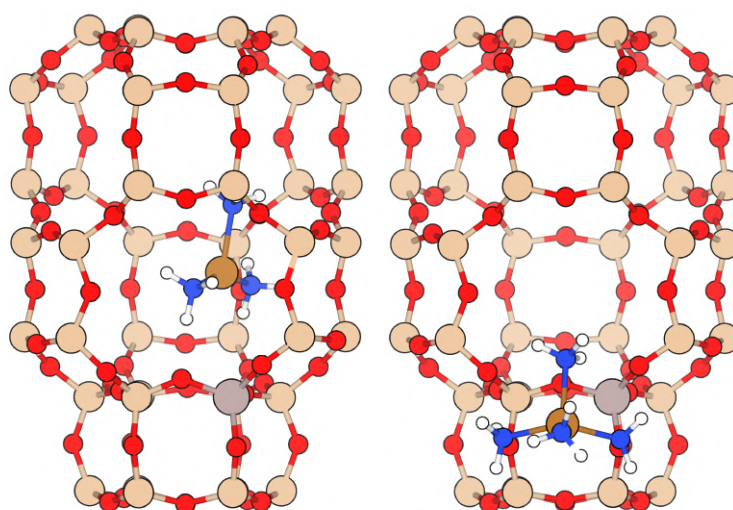
Up to four  $\text{NH}_3$  molecules were adsorbed to Cu(I) in CHA, BEA and MFI doped

with Al, B, Ga and Fe and in AlPO doped with Si, Ti, Mg and Zn. The lowest energy configurations with zero to four adsorbed  $\text{NH}_3$  in Al doped CHA, BEA and MFI and Si doped AlPO are presented in figure 5.12, 5.13, 5.14 and 5.15, respectively. Below each structure are the adsorption energies of  $\text{NH}_3$ , for all considered dopant atoms, compared to the lowest energy structures with one less  $\text{NH}_3$ .



Cu(I) in CHA.

	Al: -1.65 eV	Al: -1.14 eV
	B: -1.75 eV	B: -1.13 eV
$1 \rightarrow 0$ :	Ga: -1.69 eV	$2 \rightarrow 1$ : Ga: -1.10 eV
	Fe: -1.62 eV	Fe: -1.08 eV



	Al: -0.53 eV	Al: -0.59 eV
	B: -0.43 eV	B: -0.63 eV
$3 \rightarrow 2$ :	Ga: -0.47 eV	$4 \rightarrow 3$ : Ga: -0.61 eV
	Fe: -0.46 eV	Fe: -0.66 eV

**Figure 5.12:** The lowest energy positions of  $(\text{Cu(I)}(\text{NH}_3)_x)^+$  complexes in Al doped CHA, with corresponding  $\text{NH}_3$  adsorption energies for all considered dopant atoms.

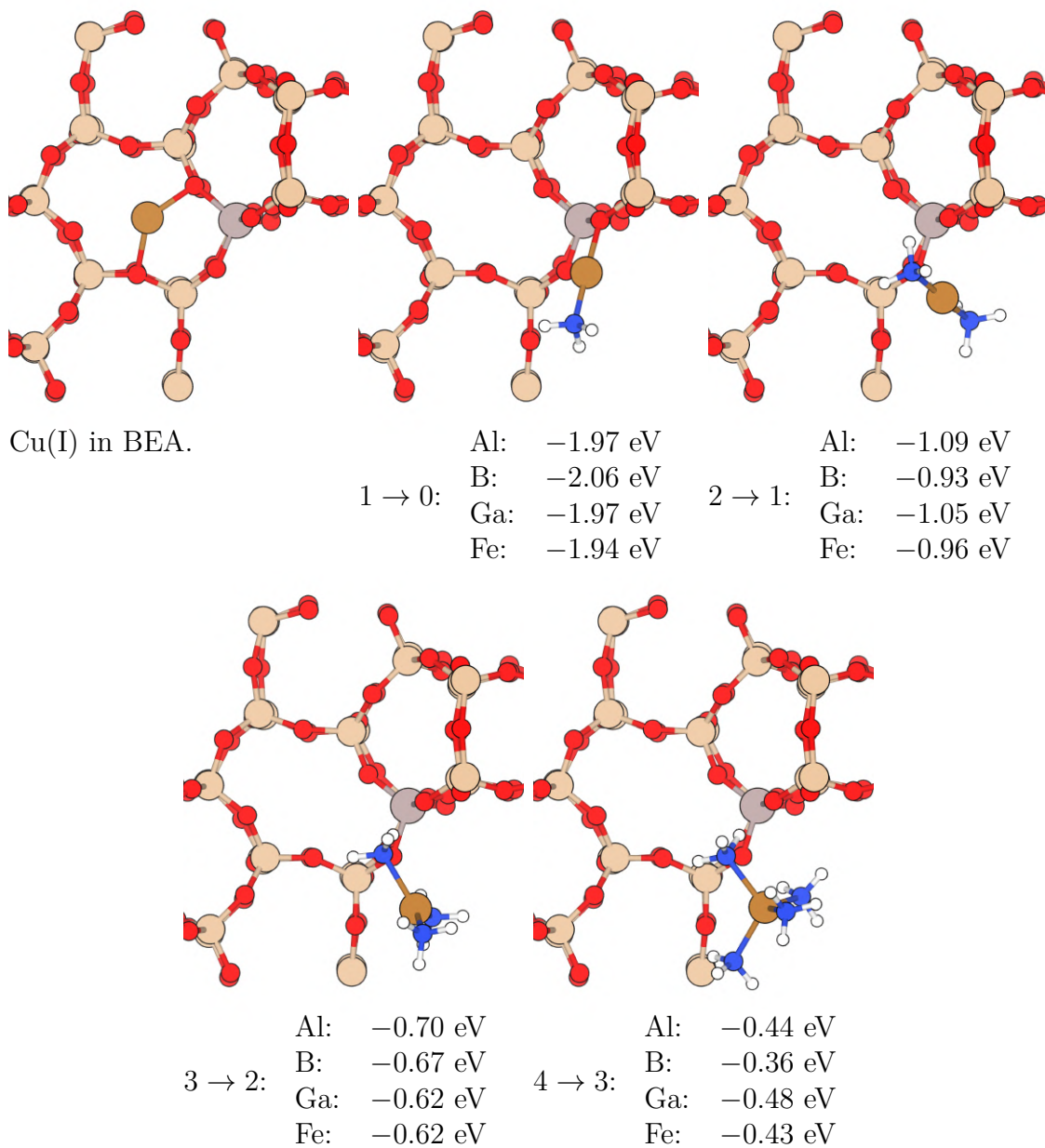
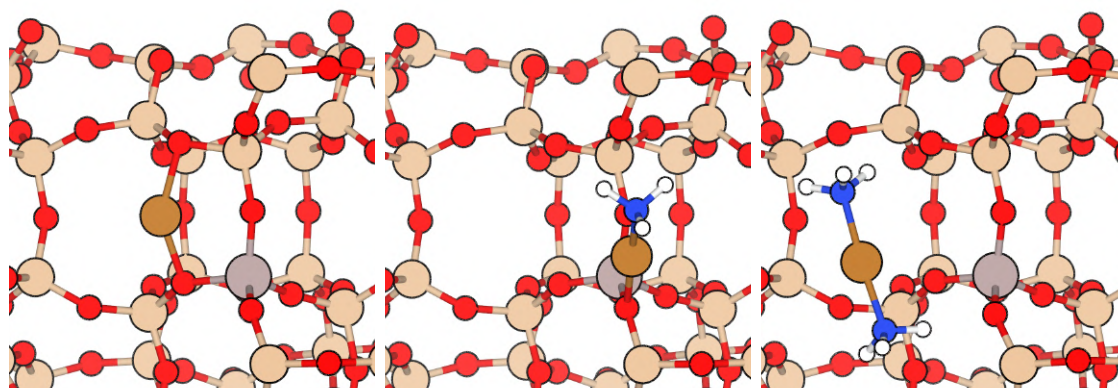
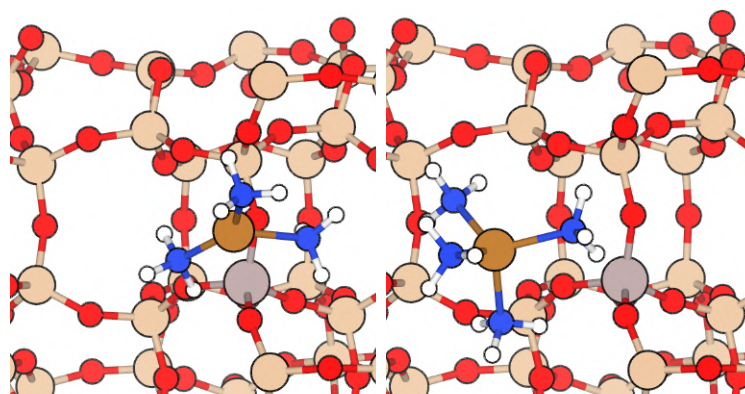


**Figure 5.13:** The lowest energy positions of  $(\text{Cu(I)}(\text{NH}_3)_x)^+$  complexes in Al doped BEA, with corresponding  $\text{NH}_3$  adsorption energies for all considered dopant atoms.



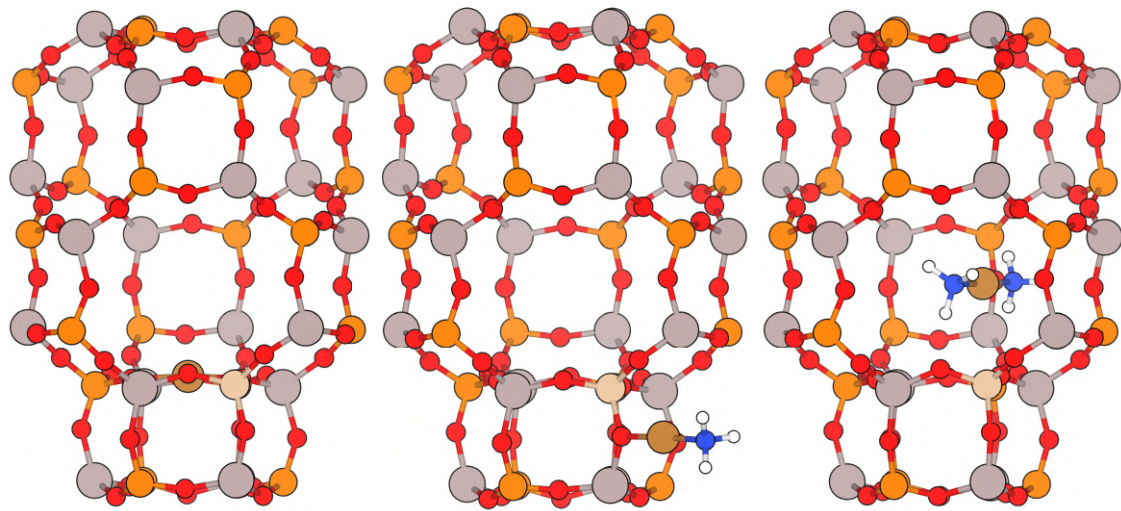
Cu(I) in MFI.

	Al: -2.05 eV		Al: -0.99 eV
	B: -2.13 eV		B: -1.08 eV
1 → 0:	Ga: -2.08 eV	2 → 1:	Ga: -0.95 eV
	Fe: -1.99 eV		Fe: -0.97 eV



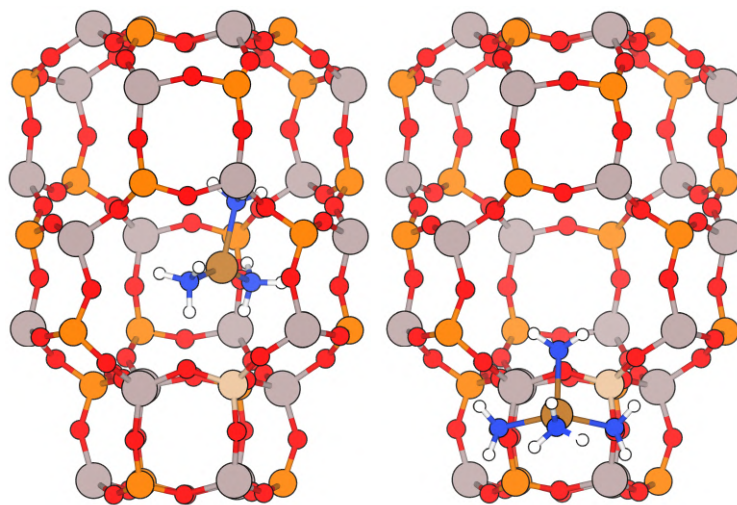
	Al: -0.66 eV		Al: -0.58 eV
	B: -0.65 eV		B: -0.49 eV
3 → 2:	Ga: -0.59 eV	4 → 3:	Ga: -0.57 eV
	Fe: -0.64 eV		Fe: -0.53 eV

**Figure 5.14:** The lowest energy positions of  $(\text{Cu(I)}(\text{NH}_3)_x)^+$  complexes in Al doped MFI, with corresponding  $\text{NH}_3$  adsorption energies for all considered dopant atoms.



Cu(I) in AlPO.

	Mg: -1.62 eV	Mg: -1.23 eV
	Zn: -1.64 eV	Zn: -1.20 eV
$1 \rightarrow 0:$	Si: -1.70 eV	$2 \rightarrow 1:$
	Ti: -1.65 eV	Si: -1.08 eV
		Ti: -0.87 eV



	Mg: -0.45 eV	Mg: -0.55 eV
	Zn: -0.44 eV	Zn: -0.56 eV
$3 \rightarrow 2:$	Si: -0.41 eV	$4 \rightarrow 3:$
	Ti: -0.43 eV	Si: -0.57 eV
		Ti: -0.69 eV

**Figure 5.15:** The lowest energy positions of  $(\text{Cu(I)}(\text{NH}_3)_x)^+$  complexes in Si doped AlPO, with corresponding  $\text{NH}_3$  adsorption energies for all considered dopant atoms.

In all considered structures,  $\text{Cu(I)}$  and  $(\text{Cu(I)}\text{NH}_3)^+$  are preferably adsorbed to the zeolite frameworks, while  $(\text{Cu(I)}(\text{NH}_3)_2)^+$ ,  $(\text{Cu(I)}(\text{NH}_3)_3)^+$  and  $(\text{Cu(I)}(\text{NH}_3)_4)^+$  are not. All of the lowest energy positions of the lone  $\text{Cu(I)}$  counter ion are in the six-membered rings. For all structures, the  $\text{NH}_3$  of the lowest energy  $(\text{Cu(I)}\text{NH}_3)^+$  complex binds to  $\text{Cu(I)}$  so that it sits opposite an O atom of the structure that the complex is adsorbed to. The shapes of the four  $(\text{Cu(I)}(\text{NH}_3)_x)^+$  complexes are presented in figure 5.16.

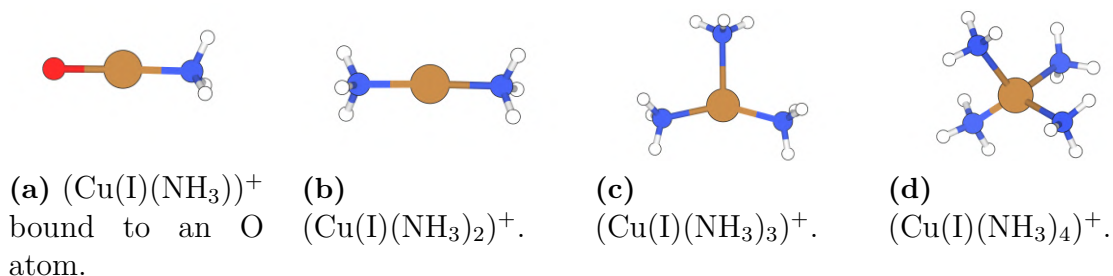


**Figure 5.16:**  $(\text{Cu(I)}(\text{NH}_3)_x)^+$  complexes in the structures.

There are no noticeable differences in the lowest energy positions for different dopant atoms, except for  $(\text{Cu(I)}(\text{NH}_3))^+$  in B doped CHA being bound to a different O atom than in the other CHA zeolites. The number of O-Cu bonds in all considered structures are presented in table 5.5.

**Table 5.5:** Number of O bonds to a  $\text{Cu(I)}$  counter ion in CHA, BEA, MFI and AIPO for all considered dopant atoms with zero to four adsorbed  $\text{NH}_3$ .

	0 $\text{NH}_3$	1 $\text{NH}_3$	2 $\text{NH}_3$	3 $\text{NH}_3$	4 $\text{NH}_3$
CHA-Al/B	3	1	0	0	0
CHA-Ga/Fe	2	1	0	0	0
BEA-Al	2	1	0	0	0
BEA-B/Fe	3	2	0	0	0
BEA-Ga	3	1	0	0	0
MFI	2	1	0	0	0
AIPO	2	1	0	0	0

In the cases of there being differences in the number of bonds for different types of dopant atoms within the same zeolite frameworks, the  $(\text{Cu(I)}(\text{NH}_3)_x)^+$  complexes are in the same positions, except for  $(\text{Cu(I)}(\text{NH}_3))^+$  in B doped CHA. However, the complexes either have one O atom a little bit closer or further away than 2.4 Å.

The adsorption energies of  $\text{NH}_3$  in all considered structures are presented in figure 5.17. For example, the adsorption of a third  $\text{NH}_3$  molecule to a structure with two  $\text{NH}_3$  is considered at 3 of the “Adsorbed  $\text{NH}_3$ ” axis.

## 5. Results

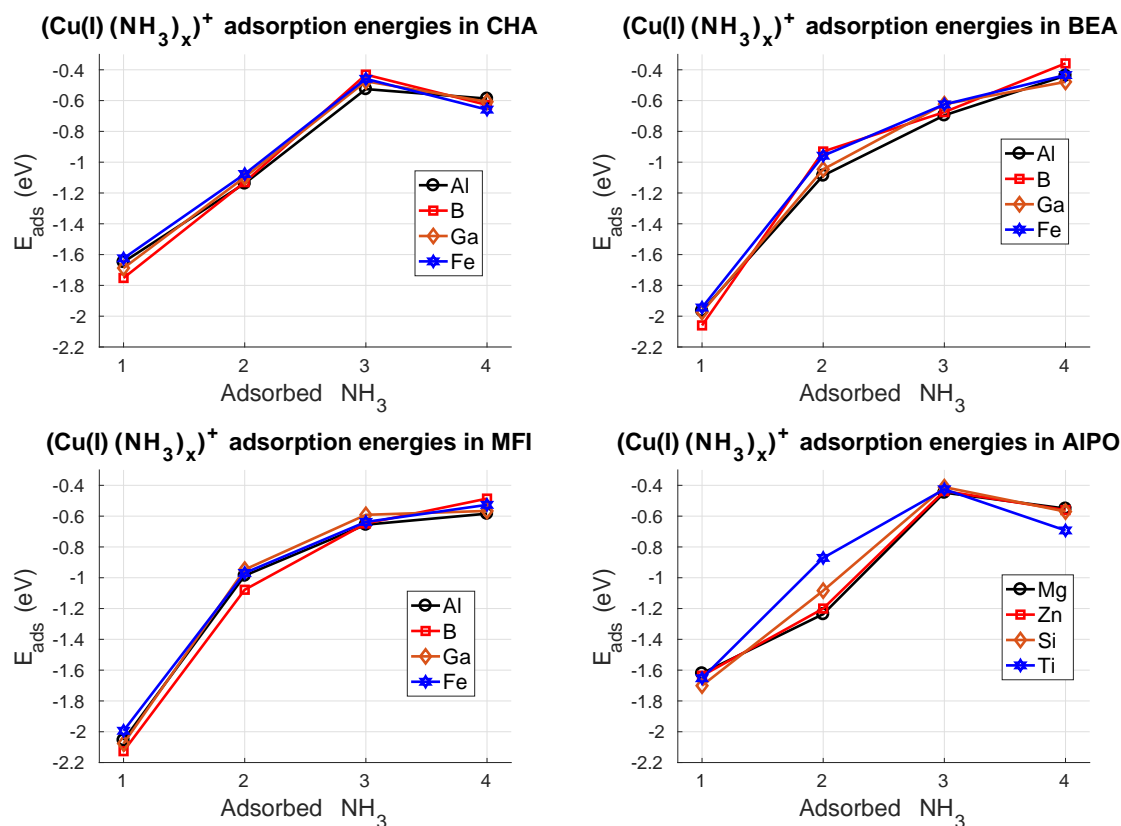


**Figure 5.17:** The sequential adsorption energies of  $\text{NH}_3$  on  $\text{Cu(I)}$  for all considered dopant atoms in CHA, BEA, MFI and AIPO.

In all zeolites, the type of dopant atom does not change the adsorption energies more than about 0.2 eV. The differences are larger in AIPO than in the zeolites, with two major factors likely being that different types of atoms are replaced and that the Ti atom is much larger than the Si atom. The  $\text{NH}_3$  molecule that is most tightly bound to the structures is in all cases the first one.

### 5.4.1 Comparison to O-Cu bond order

A relationship was found between the bond order of the O-Cu bond and the adsorption energy of the first  $\text{NH}_3$  molecule to the  $\text{Cu(I)}$  counter ion in the zeolites. The bond orders are of the structures with the  $\text{NH}_3$  adsorbed, contrary to the Brønsted case. When there are no  $\text{NH}_3$  adsorbed, the  $\text{Cu(I)}$  counter ion forms bonds with multiple O atoms of the zeolites, as visualized in figures 5.12, 5.13 and 5.14. This makes it hard to relate the bond orders to the adsorption energy. The adsorption energy of a  $\text{NH}_3$  molecule to  $\text{Cu(I)}$  as a function of the O-Cu bond order in CHA, BEA and MFI, together with linear fits and  $R^2$  values, are presented in figure 5.18.

The  $R^2$  values of 0.904, 0.983 and 0.844 show that a correlation exists. The results are harder to explain than the Brønsted case in section 5.3.1. There was found to be no correlation between the bond order of N-Cu and the adsorption energy since only one electron pair of N is involved in the bond. However, previous studies have shown that a strengthened bond on one side of an atom can loosen the bond on the other side [83]. So a higher bond order of the O-Cu bond can induce a looser bond

$\text{NH}_3$  to the Cu counter ion and that its adsorption energy therefore is lower.

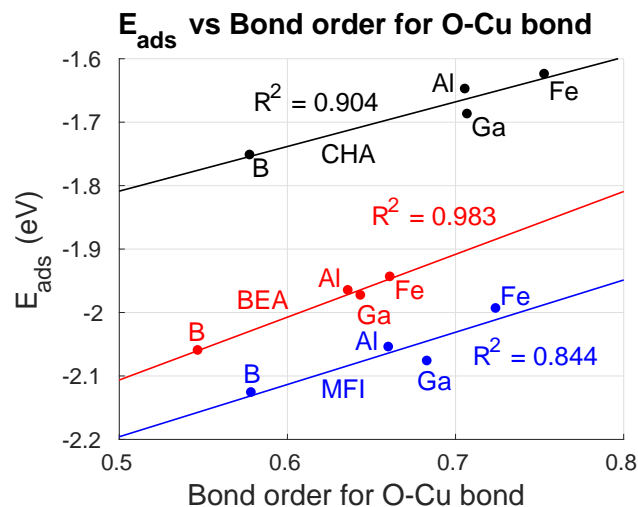


**Figure 5.18:** Adsorption energy of  $\text{NH}_3$  as a function of bond order of the O-Cu bond, when exchanging dopant atom in CHA, BEA and MFI.

#### 5.4.2 Phase diagrams for Al/Si doped structures

Phase diagrams for  $(\text{Cu(I)}(\text{NH}_3)_x)^+$  phases were obtained for CHA, BEA and MFI doped with Al and AIPO doped with Si. They are presented in figure 5.19.

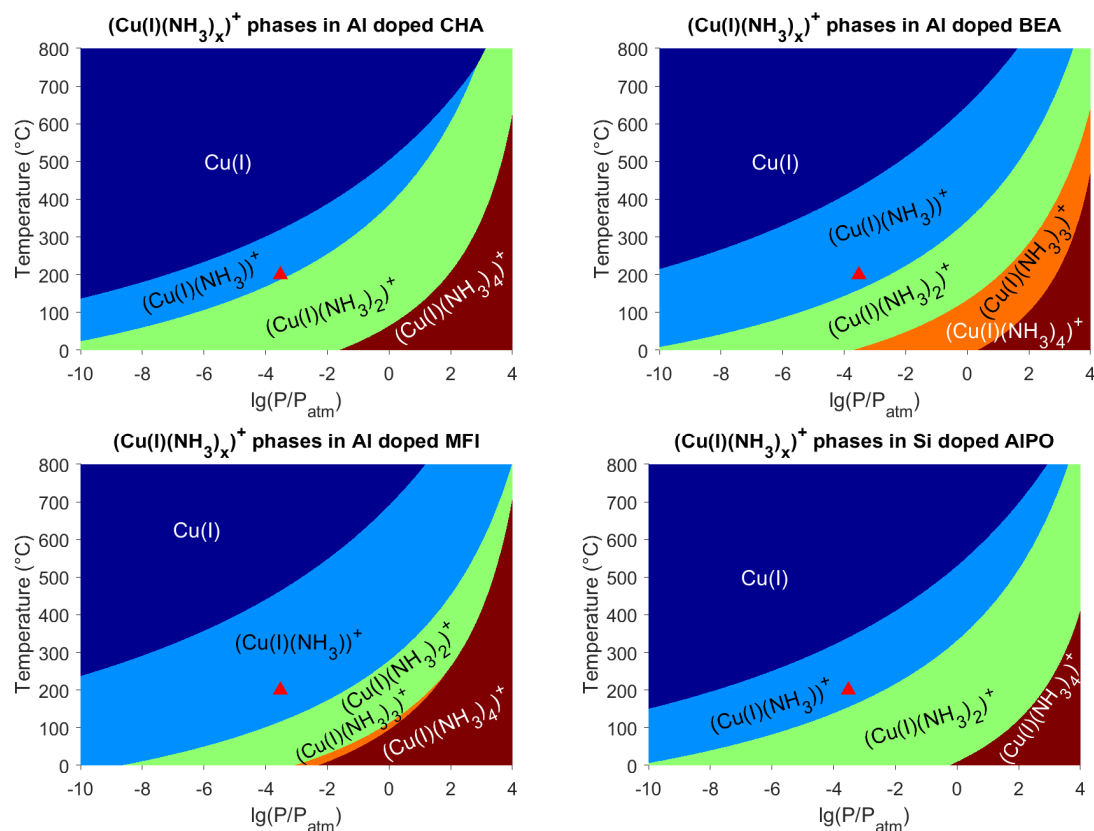


**Figure 5.19:**  $(\text{Cu(I)}(\text{NH}_3)_x)^+$  phase diagrams for Al doped CHA, BEA and MFI and Si doped AIPO. The triangle indicates standard operating conditions at 300 ppm  $\text{NH}_3$  and a temperature of 200 °C.

The preferred phases varies a lot between the structures. However, for all cases only the phases with zero to two adsorbed  $\text{NH}_3$  are present around the standard operating conditions. Qualitatively, higher adsorption energies mean that phases with more adsorbed  $\text{NH}_3$  are more preferred at higher temperatures and lower pressures.

### 5.4.3 TPD curves for Al/Si doped structures

TPD curves for desorption of the fourth, third, second and first  $\text{NH}_3$  molecules bound to Cu(I) counter ions were obtained for CHA, BEA and MFI doped with Al and AIPO doped with Si. The starting configurations were fully loaded with four  $\text{NH}_3$  adsorbed to every Cu(I) counter ion. The concentrations for each sequential desorbed  $\text{NH}_3$  and their corresponding total concentrations of desorbed  $\text{NH}_3$  from the Cu(I) counter ions are presented in figure 5.20.

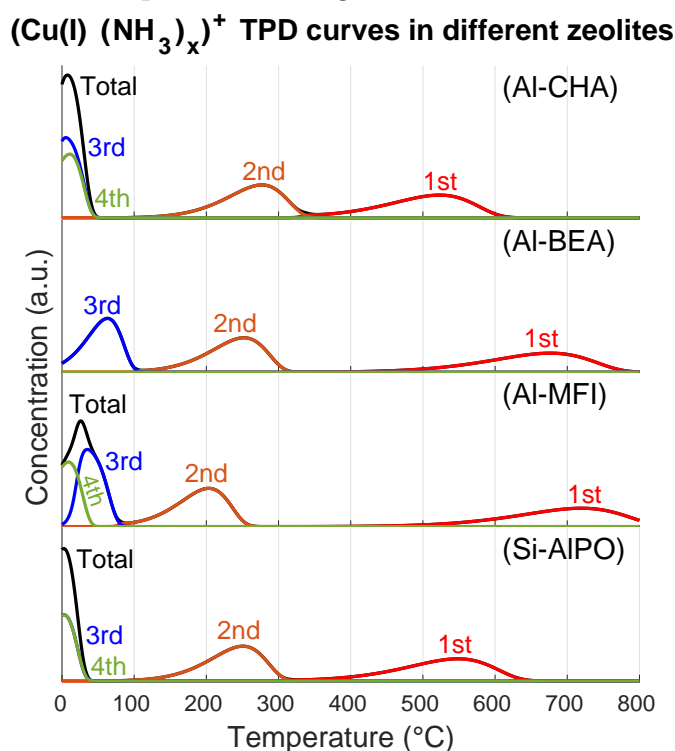


**Figure 5.20:** TPD curves for desorption of  $\text{NH}_3$  from Al doped CHA, BEA and MFI and Si doped AIPO.

In analogy to the phase diagrams in figure 5.19, it is clear that the fourth and third  $\text{NH}_3$  desorb at temperatures below standard operating conditions. The largest differences are obtained for desorption of the first  $\text{NH}_3$  molecules as they show the largest differences in adsorption energies. Since the adsorption energies of the third  $\text{NH}_3$  are lower than the adsorption energies of the fourth  $\text{NH}_3$  in CHA and AIPO, the third  $\text{NH}_3$  desorb almost immediately after the fourth.

## 5.5 $\text{NH}_3$ adsorption on Cu(II)

Up to four  $\text{NH}_3$  molecules were adsorbed to Cu(II) in CHA, BEA and MFI doped

with Al, B, Ga and Fe and in AlPO doped with Si, Ti, Mg and Zn. The lowest energy configurations with zero to four adsorbed  $\text{NH}_3$  in Al doped CHA, BEA and MFI and Si doped AlPO are presented in figure 5.21, 5.22, 5.23 and 5.24, respectively. The distribution of Al dopant atoms in CHA in figure 5.21 is the same as for the B, Ga and Fe dopants. The 16 other Al distributions in CHA are presented in section 5.7. Below each structure are the adsorption energies of  $\text{NH}_3$ , for all considered dopant atoms, compared to the lowest energy structures with one less  $\text{NH}_3$ .

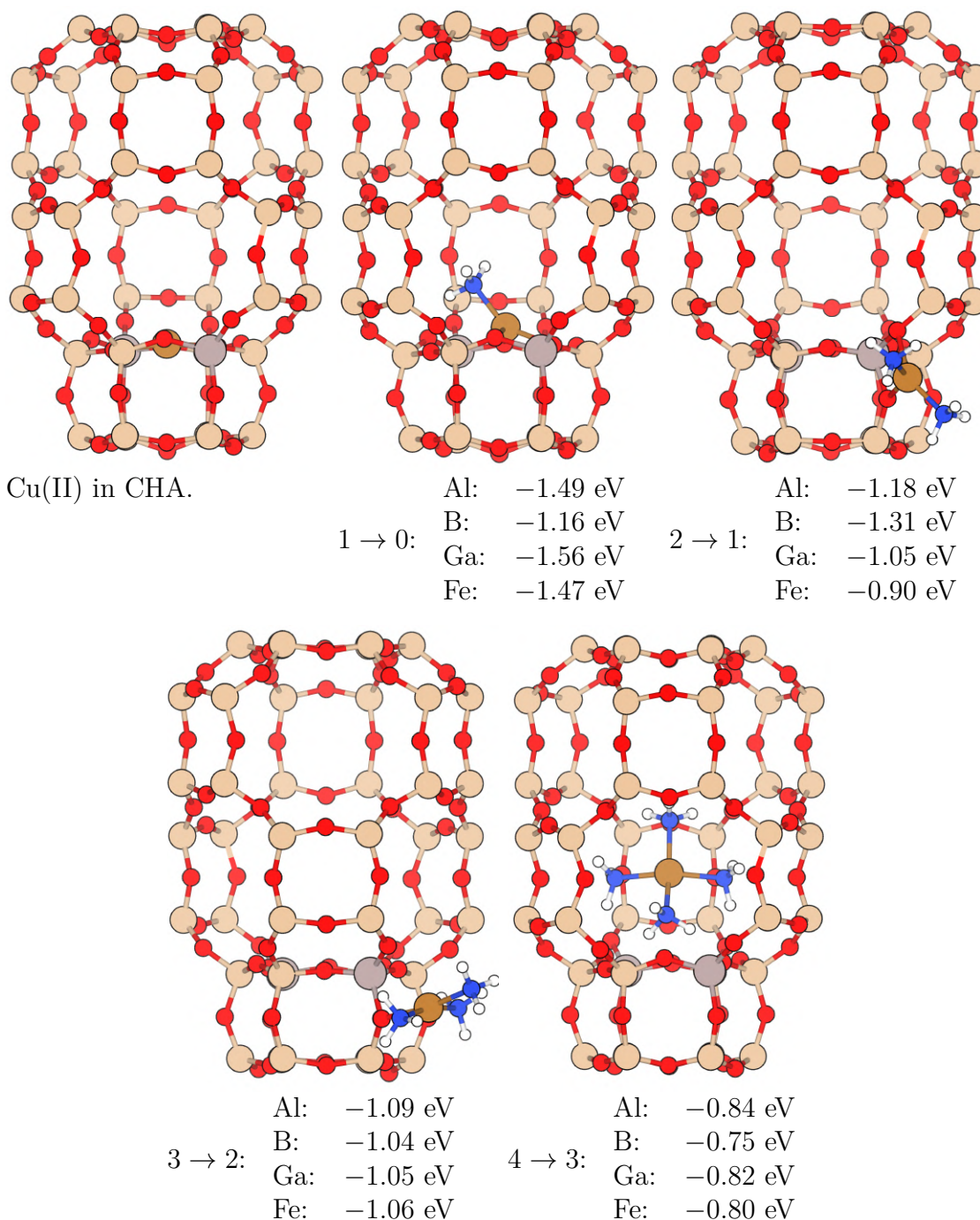
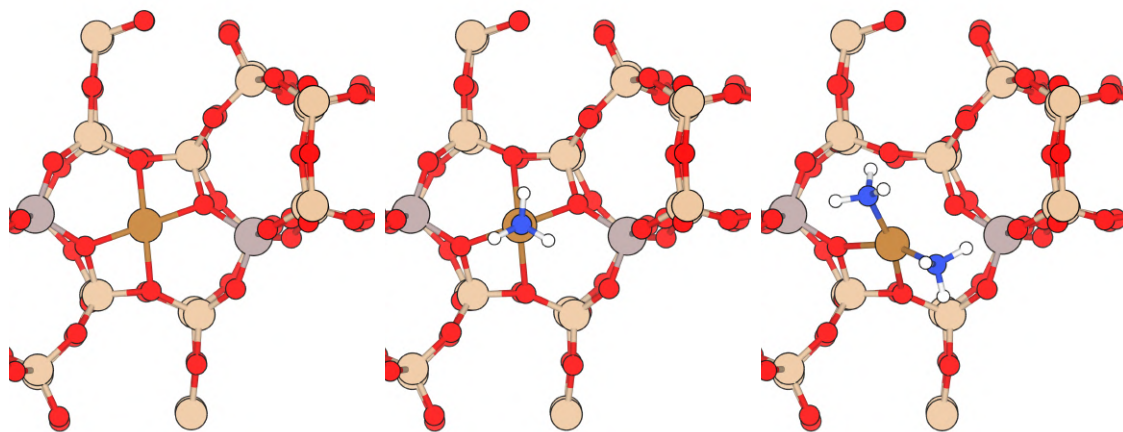


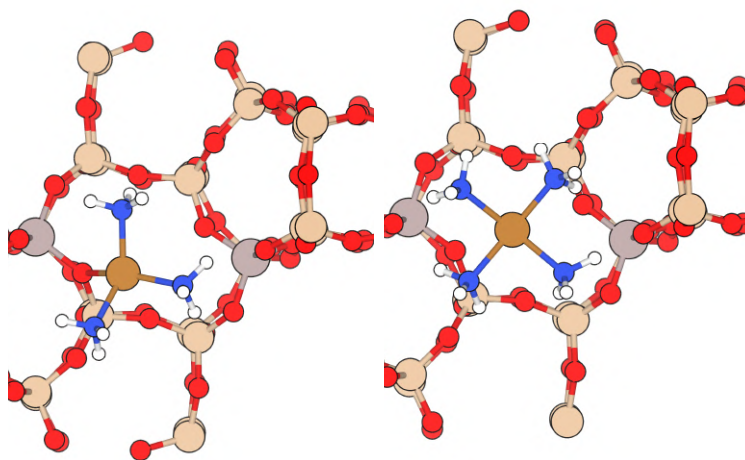
**Figure 5.21:** The lowest energy positions of  $(\text{Cu(II)}(\text{NH}_3)_x)^{2+}$  complexes in Al doped CHA, with corresponding  $\text{NH}_3$  adsorption energies for all considered dopant atoms.

The structure with  $(\text{Cu(II)})(\text{NH}_3)_3^{2+}$  in figure 5.21 is rotated  $180^\circ$  compared to the other ones. However, when adsorbed at the other Al dopant atom the energy is within 0.01 eV of the lowest energy one, since the positions are symmetric. The energy difference comes from the structures not being equally converged.



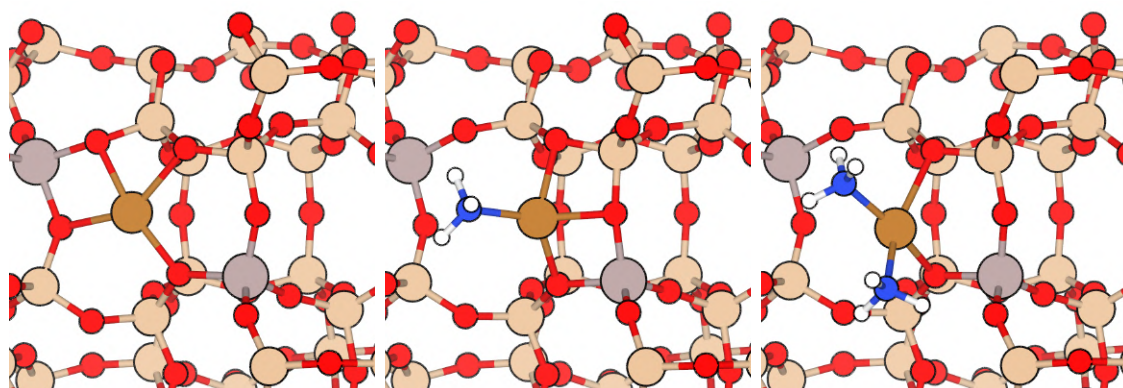
Cu(II) in BEA.

	Al: -1.29 eV	Al: -1.32 eV
	B: -1.10 eV	B: -1.33 eV
$1 \rightarrow 0$ :	Ga: -1.33 eV	$2 \rightarrow 1$ :
	Fe: -1.40 eV	Fe: -1.15 eV



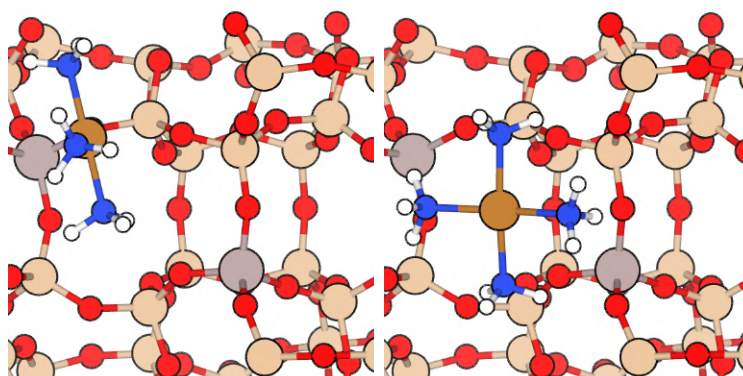
	Al: -0.69 eV	Al: -1.22 eV
	B: -0.70 eV	B: -1.28 eV
$3 \rightarrow 2$ :	Ga: -0.67 eV	$4 \rightarrow 3$ :
	Fe: -0.67 eV	Fe: -1.15 eV

**Figure 5.22:** The lowest energy positions of  $(\text{Cu(II)})(\text{NH}_3)_x^{2+}$  complexes in Al doped BEA, with corresponding  $\text{NH}_3$  adsorption energies for all considered dopant atoms.



Cu(II) in MFI.

	Al: -1.69 eV	Al: -1.40 eV
	B: -1.43 eV	B: -1.56 eV
1 → 0:	Ga: -1.43 eV	2 → 1: Ga: -1.43 eV
	Fe: -1.51 eV	Fe: -1.15 eV



	Al: -1.04 eV	Al: -1.19 eV
	B: -0.75 eV	B: -1.38 eV
3 → 2:	Ga: -0.92 eV	4 → 3: Ga: -1.24 eV
	Fe: -0.81 eV	Fe: -1.22 eV

**Figure 5.23:** The lowest energy positions of  $(\text{Cu(II)})(\text{NH}_3)_x)^{2+}$  complexes in Al doped MFI, with corresponding  $\text{NH}_3$  adsorption energies for all considered dopant atoms.

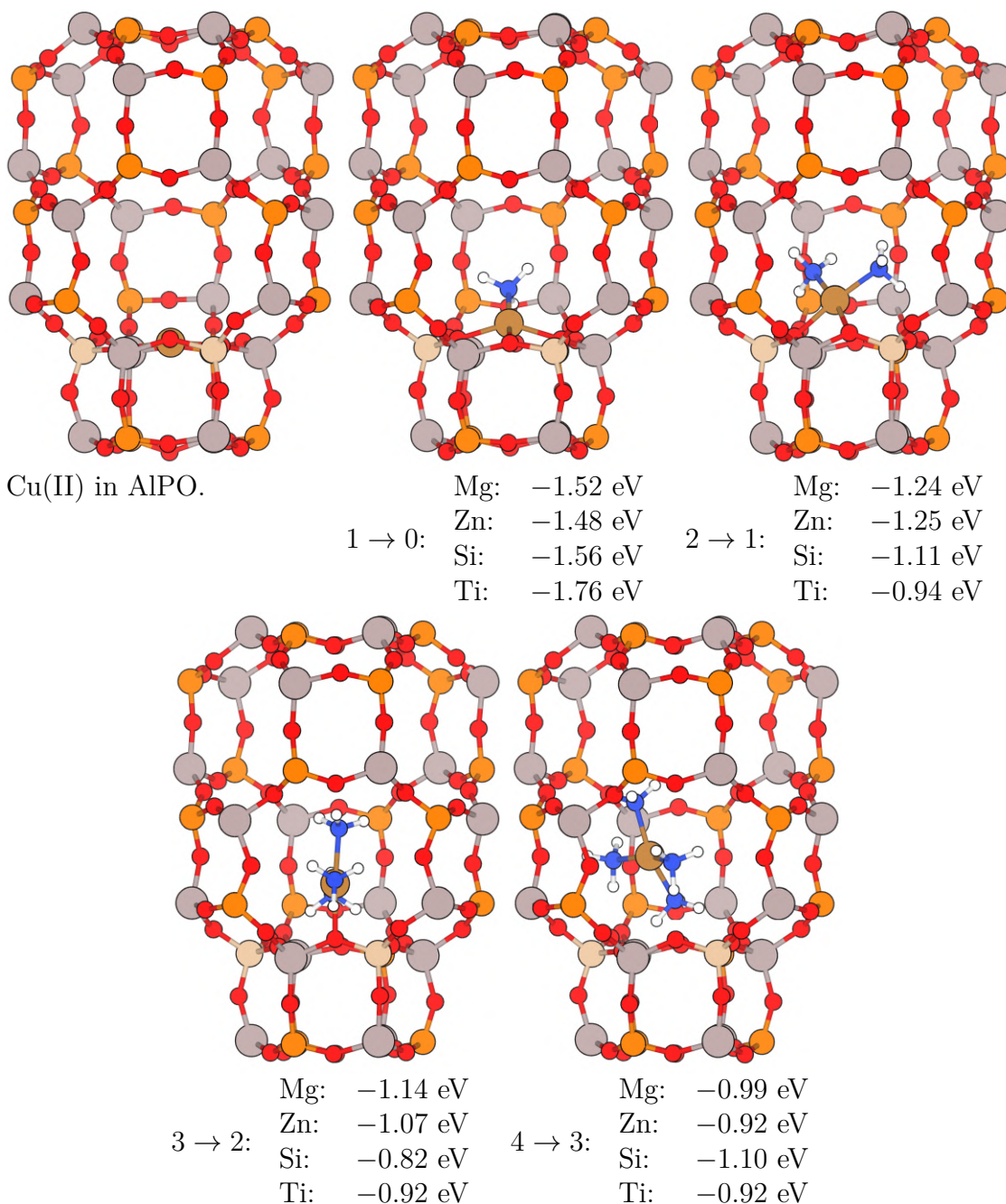


**Figure 5.24:** The lowest energy positions of  $(\text{Cu(II)(NH}_3)_x)^{2+}$  complexes in Si doped AlPO, with corresponding  $\text{NH}_3$  adsorption energies for all considered dopant atoms.

In all considered structures,  $\text{Cu(II)}$  to  $(\text{Cu(II)(NH}_3)_3)^{2+}$  are preferably adsorbed to the zeolite frameworks, while  $(\text{Cu(II)(NH}_3)_4)^{2+}$  is not. All of the lowest energy positions of the lone  $\text{Cu(II)}$  counter ion are in the six-membered rings, similarly to  $\text{Cu(I)}$ . The shape of the  $(\text{Cu(II)(NH}_3)_x)^{2+}$  complex varies considerably between the frameworks, however it is always in the six-membered rings. In CHA, the  $(\text{Cu(II)(NH}_3)_2)^{2+}$  complex forms a semi-tetrahedral configuration with the O atoms of the zeolite, while in BEA, MFI (except Fe doped) and AlPO the  $\text{NH}_3$  molecules are opposite of O atoms of the structures, forming planar configurations. These two shapes are visualized in figure 5.25a and 5.25b, respectively.

In CHA, MFI and AIPO the lowest energy shapes of  $(\text{Cu(II)}(\text{NH}_3)_3)^{2+}$  are as in figure 5.25c, with two  $\text{NH}_3$  opposite each other and one  $\text{NH}_3$  opposite an O atom of the structures. For BEA however, a more tetrahedral like shape is the lowest energy one, which was visualized in figure 5.22. The shape of the lowest energy  $(\text{Cu(II)}(\text{NH}_3)_4)^{2+}$  complex is the same in all considered structures, it is visualized in figure 5.25d.

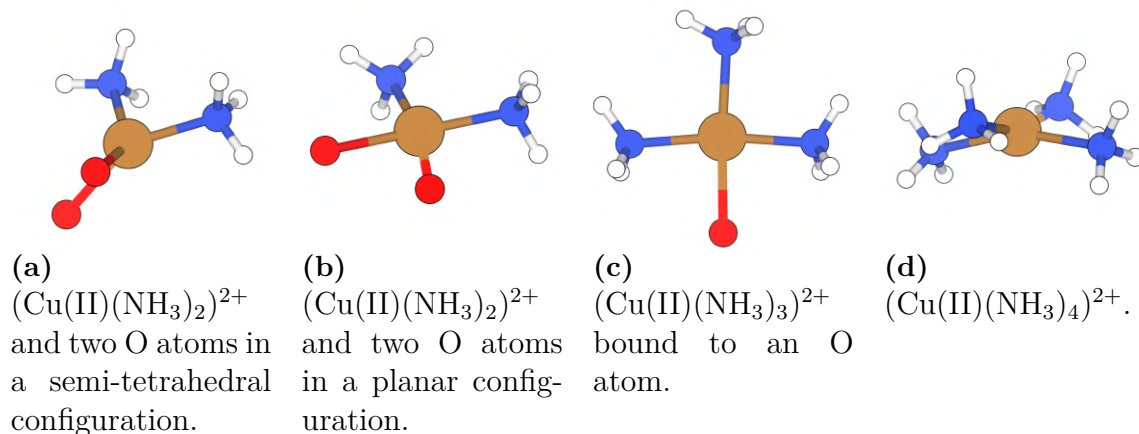


**Figure 5.25:**  $(\text{Cu(II)}(\text{NH}_3)_x)^{2+}$  complexes in the structures.

The number of O-Cu bonds in all considered structures are presented in table 5.6.

**Table 5.6:** Number of O bonds to a Cu(II) counter ion in CHA, BEA, MFI and AIPO for all considered dopant atoms with zero to four adsorbed  $\text{NH}_3$ .

	0 $\text{NH}_3$	1 $\text{NH}_3$	2 $\text{NH}_3$	3 $\text{NH}_3$	4 $\text{NH}_3$
CHA-Al	4	3	2	1	0
CHA-B-Ga	4	3	2	1	0
CHA-Fe	3	3	2	1	0
BEA-Al/B	4	4	2	1	0
BEA-Ga	4	4	3	1	0
BEA-Fe	4	2	3	1	0
MFI-Al/B/Ga	4	3	2	1	0
MFI-Fe	4	2	1	1	0
AIPO-Mg/Zn/Si	4	3	2	1	0
AIPO-Ti	3	3	2	1	0

The adsorption energies of  $\text{NH}_3$  in all considered structures are presented in figure 5.26. Compared to the  $(\text{Cu(I)}(\text{NH}_3)_x)^+$  complexes in section 5.4, the adsorption energies and number of bonds varies considerably between different types of dopant atoms. For CHA and BEA, the differences are mainly for the first and second adsorbed  $\text{NH}_3$ , which means that the type of dopant atom matters the most for the lowest energy configurations with zero or one adsorbed  $\text{NH}_3$ . The reason for BEA having lower adsorption energies of the third adsorbed  $\text{NH}_3$ , than the other structures, is probably that shape of the lowest energy  $(\text{Cu(II)}(\text{NH}_3)_3)^{2+}$  complex in BEA is more tetrahedral like than the complex in figure 5.25c.

## 5. Results

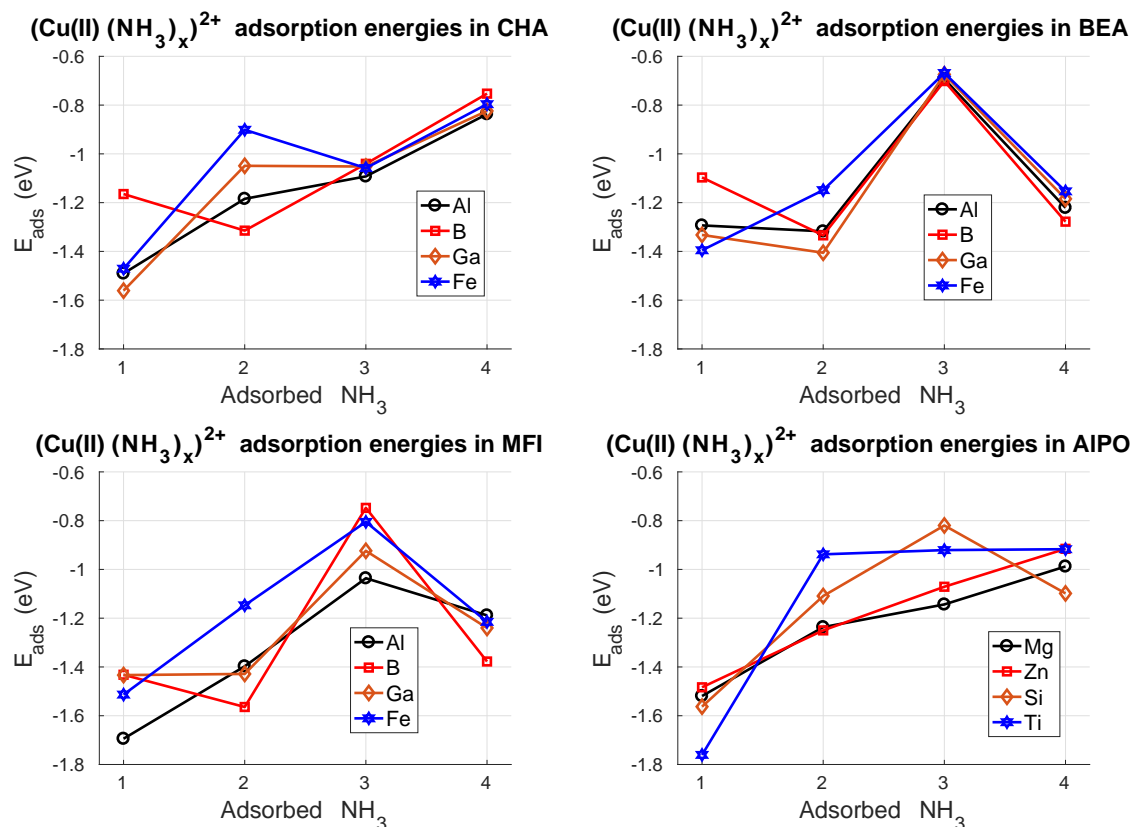


**Figure 5.26:** The sequential adsorption energies of  $\text{NH}_3$  on  $\text{Cu(II)}$  for all considered dopant atoms in CHA, BEA, MFI and AIPO.

The six-membered rings with the lowest energy positions of  $\text{Cu(II)}$  and  $(\text{Cu(II)(NH}_3)_x)^{2+}$  in Al, B, Ga and Fe doped CHA are presented in figure 5.27.

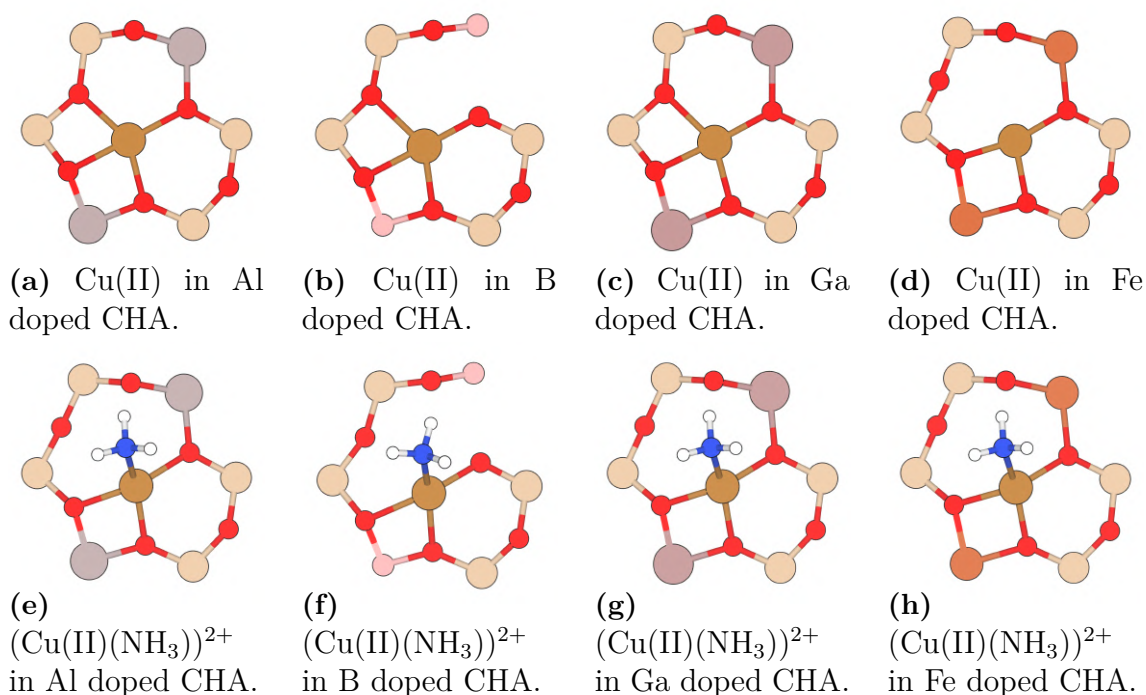


**Figure 5.27:**  $\text{Cu(II)}$  and  $(\text{Cu(II)(NH}_3)_x)^{2+}$  in Al, B, Ga and Fe doped CHA.

Here the influence of the type of dopant atom is very clear. In the B doped CHA, one of the O atoms loses its bond to a dopant atom. In Fe doped CHA, the lone Cu(II) counter ion only bonds to three O atoms, instead of four as for the other dopant atoms. These differences explain why the number of bonds and adsorption energies vary between the dopant atoms. The Al and Ga lowest energy configurations are the most similar, and they also have the most similar adsorption energies. The reason for Cu(II) only binding to three O atoms in Fe doped CHA is probably that Fe can take an oxidation state of up to +7, so it can share more electrons with Cu(II), which then does not need to bind to the fourth O atom.

There are also similar differences for the lowest energy configurations of Cu(II) and  $(\text{Cu(II)(NH}_3)_2)^{2+}$  for the different types of dopant atoms in BEA, which explains the differences in adsorption energies there. For MFI, there are also large differences in the adsorption energies of the third  $\text{NH}_3$  for different types of dopant atoms, which can be explained by there also being significant differences in the lowest energy positions of  $(\text{Cu(II)(NH}_3)_2)^{2+}$  in MFI. The lowest energy positions of  $(\text{Cu(II)(NH}_3)_2)^{2+}$  in the six-membered rings of Al, B, Ga and Fe doped MFI are presented in figure 5.28. The distance between the Cu(II) counter ion and the second closest O atom in the structures is also noted.

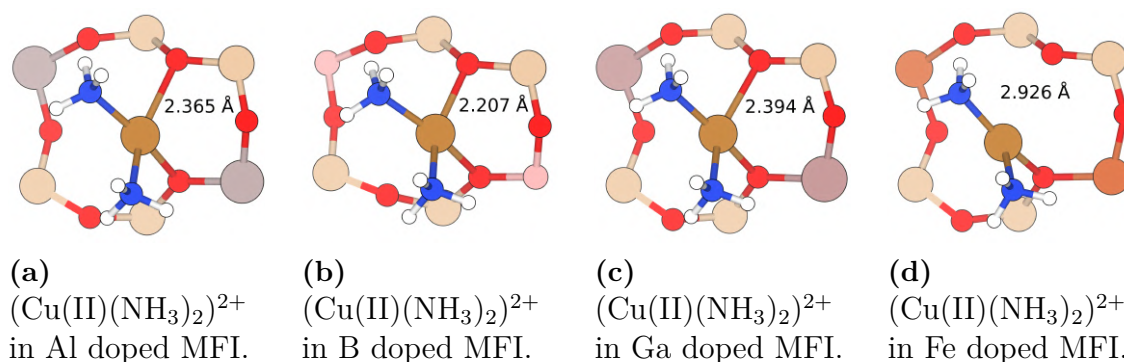


**Figure 5.28:**  $(\text{Cu(II)(NH}_3)_2)^{2+}$  complex in Al, B, Ga and Fe doped MFI.

In Al, B and Ga doped MFI, the Cu(II) counter ions are bound to two O atoms, while in Fe doped MFI it is only bound to one. It is more tightly bound to the upper O atom in B doped than in Al and Ga doped MFI. The bond length is 2.207 Å for B, 2.365 Å for Al and 2.394 Å for Ga doped MFI. The distance for Fe doped MFI is 2.926 Å, so there is clearly no bond in that case. As for Cu(II) in Fe doped CHA in figure 5.27d, the reason for this is probably that Fe can take an oxidation state of up to +7. The similarity of the Al and Ga doped bond lengths, compared to the other two, somewhat explains the adsorption energies of the third  $\text{NH}_3$  being about the same for them.

In Mg and Zn doped AlPO, the adsorption energies of  $\text{NH}_3$  are about the same. They are, however, not the same for Si and Ti doped, in which both a P atom is replaced. This can probably be explained by the Ti atom being much larger than the Si atom, which influences shapes of the lowest energy configurations considerably.

### 5.5.1 Phase diagrams for different dopant atoms in CHA

Phase diagrams for  $(\text{Cu(II)}(\text{NH}_3)_x)^{2+}$  phases were calculated for Al, B, Ga and Fe doped CHA and are presented in figure 5.29.

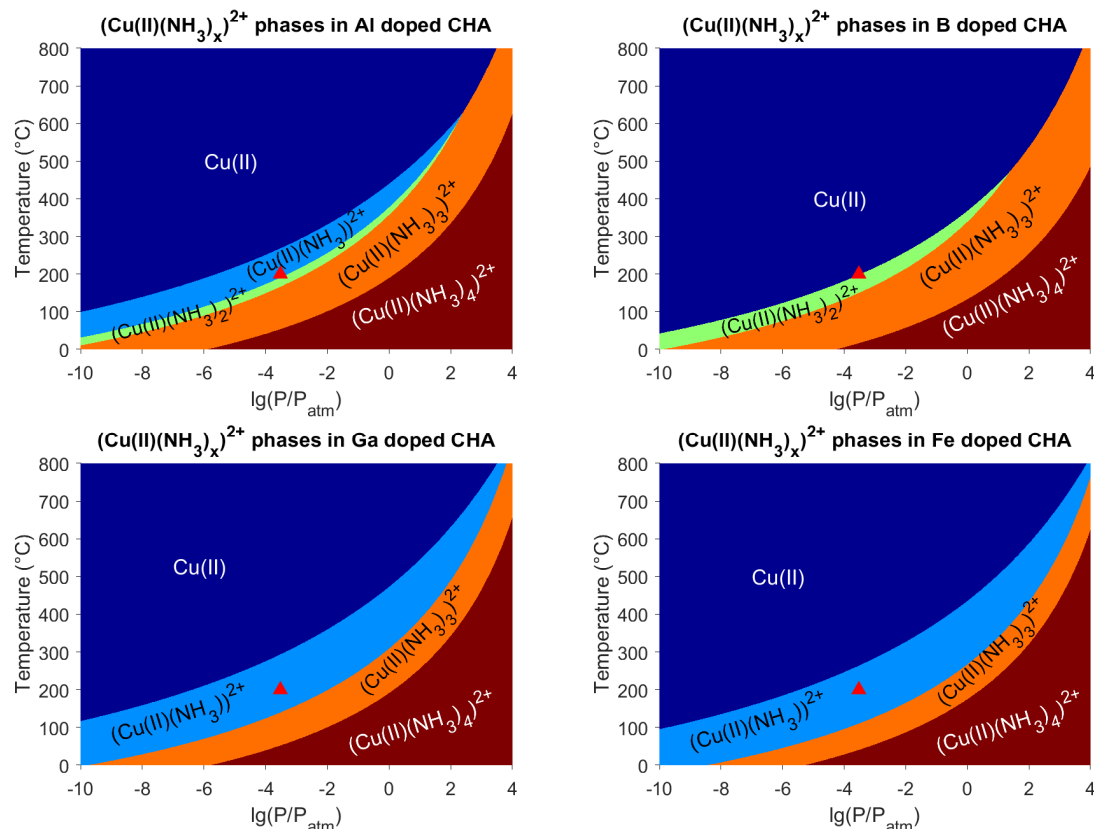


**Figure 5.29:**  $(\text{Cu(II)}(\text{NH}_3)_x)^{2+}$  phase diagrams for Al, B, Ga and Fe doped CHA. The triangle indicates standard operating conditions at 300 ppm  $\text{NH}_3$  and a temperature of 200 °C.

All of the phase diagrams are quite similar, but with the Al and B doped structures having lowest energy phases of  $(\text{Cu(II)}(\text{NH}_3)_2)^{2+}$  around the standard operating conditions due to having higher adsorption energies of the second  $\text{NH}_3$  than the Ga and Fe doped structures. B doped CHA has a low adsorption energy of the first  $\text{NH}_3$  compared to the other structures, which means that the  $(\text{Cu(II)}(\text{NH}_3))^{2+}$  phase is never the lowest energy and that the Cu(II) phase is the lowest energy even at standard operating conditions.

### 5.5.2 TPD curves for different dopant atoms in CHA

TPD curves for desorption of the fourth, third, second and first  $\text{NH}_3$  molecules bound to Cu(II) counter ions were calculated for Al, B, Ga and Fe doped CHA. The starting configurations were fully loaded with four  $\text{NH}_3$  adsorbed to every Cu(II) counter ion. The concentrations for each sequential desorbed  $\text{NH}_3$  and their corresponding total concentrations of desorbed  $\text{NH}_3$  from the Cu(II) counter ions are presented in figure 5.30.

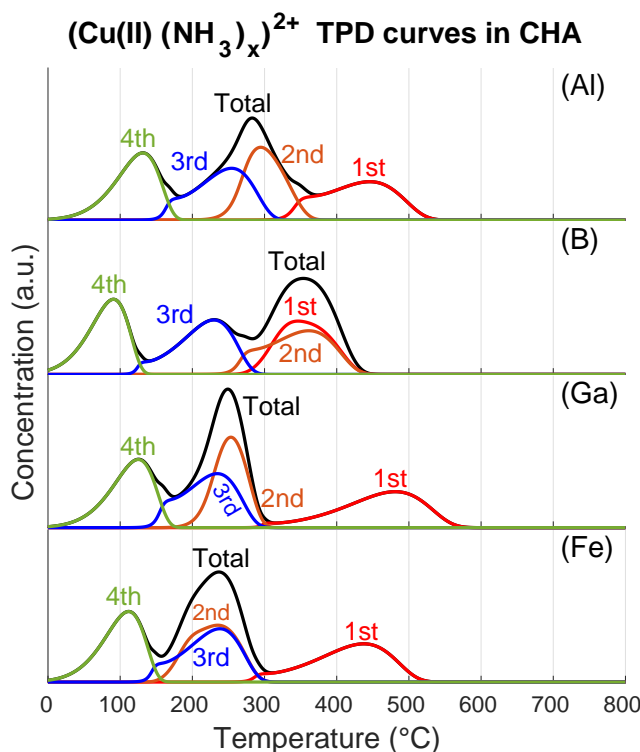
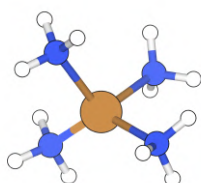


**Figure 5.30:** TPD curves for desorption of  $\text{NH}_3$  from Al, B, Ga and Fe doped CHA.

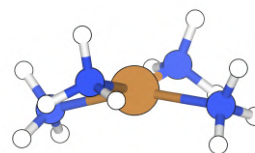
Like the phase diagrams in figure 5.29, the TPD curves are similar for the different dopant atoms. The biggest differences are for desorption of the second  $\text{NH}_3$  due to their adsorption energies differing the most. The first  $\text{NH}_3$  desorbs almost immediately after the second in B doped CHA due to its low adsorption energy.

## 5.6 $(\text{Cu(I)}(\text{NH}_3)_4)^+$ vs $(\text{Cu(II)}(\text{NH}_3)_4)^{2+}$ shapes

The  $(\text{Cu(I)}(\text{NH}_3)_4)^+$  and  $(\text{Cu(II)}(\text{NH}_3)_4)^{2+}$  complexes in the structures are all shaped as in figure 5.31a and 5.31b, respectively.



(a)  $(\text{Cu(I)}(\text{NH}_3)_4)^+$  complex.



(b)  $(\text{Cu(II)}(\text{NH}_3)_4)^{2+}$  complex.

**Figure 5.31:**  $(\text{Cu(I)}(\text{NH}_3)_4)^+$  and  $(\text{Cu(II)}(\text{NH}_3)_4)^{2+}$  complexes in the structures.

$(\text{Cu(I)}(\text{NH}_3)_4)^+$  is tetrahedral, while  $(\text{Cu(II)}(\text{NH}_3)_4)^{2+}$  is planar. The difference in shapes of the complexes comes down to the difference in number of electrons. Since Cu(I) has the electronic configuration  $[\text{Ar}] 3d^{10}$ , its 3d orbitals can hybridize with the lone electron pairs of the four  $\text{NH}_3$ . Removing one electron means that one of the 3d orbitals is not occupied and that the other ones then cannot hybridize. The tetrahedral structure is then unstable due to Jahn-Teller distortions [84].

## 5.7 Distributions of two Al dopant atoms in CHA

The reason for testing 17 different distributions of Al in CHA is because of CHA being the most used zeolite in catalytic applications today [71] and Al being its most common dopant atom, since its size is close to Si [85]. In figure 5.32, the different positions of the second Al dopant atom are noted with letters a-q on the Si atoms that were replaced, while the lone Al dopant atom in the figure is there in all 17 distributions.

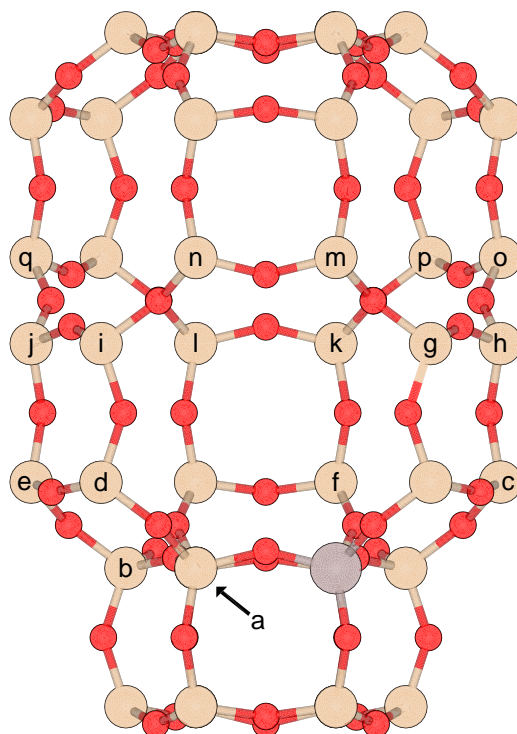


**Figure 5.32:** CHA cage with the first Al dopant atom and the 17 different options for the second one noted with letters a-q.

Atom a is the one behind the one pointed at in figure 5.32. Distribution a was also considered for B, Ga and Fe in section 5.5. Symmetry equivalent positions and positions prohibited by Löwenstein's rule were not considered [15].

The different Al dopant distributions in CHA are divided into three sub categories. The first sub category considers positions a-f of the second Al dopant in figure 5.32. Positions a and b are in the same six-membered ring as the first Al dopant, while positions c-f are one layer up. The second sub category considers positions g-l of Al dopant atoms two layers up, while the third sub category considers positions m-q of Al dopant atoms three layers up.

The lowest energy configurations for distributions a-f with one  $\text{NH}_3$  adsorbed are presented in figure 5.33. Included below each configuration are each of the  $\text{NH}_3$  adsorption energies for the dopant distributions.

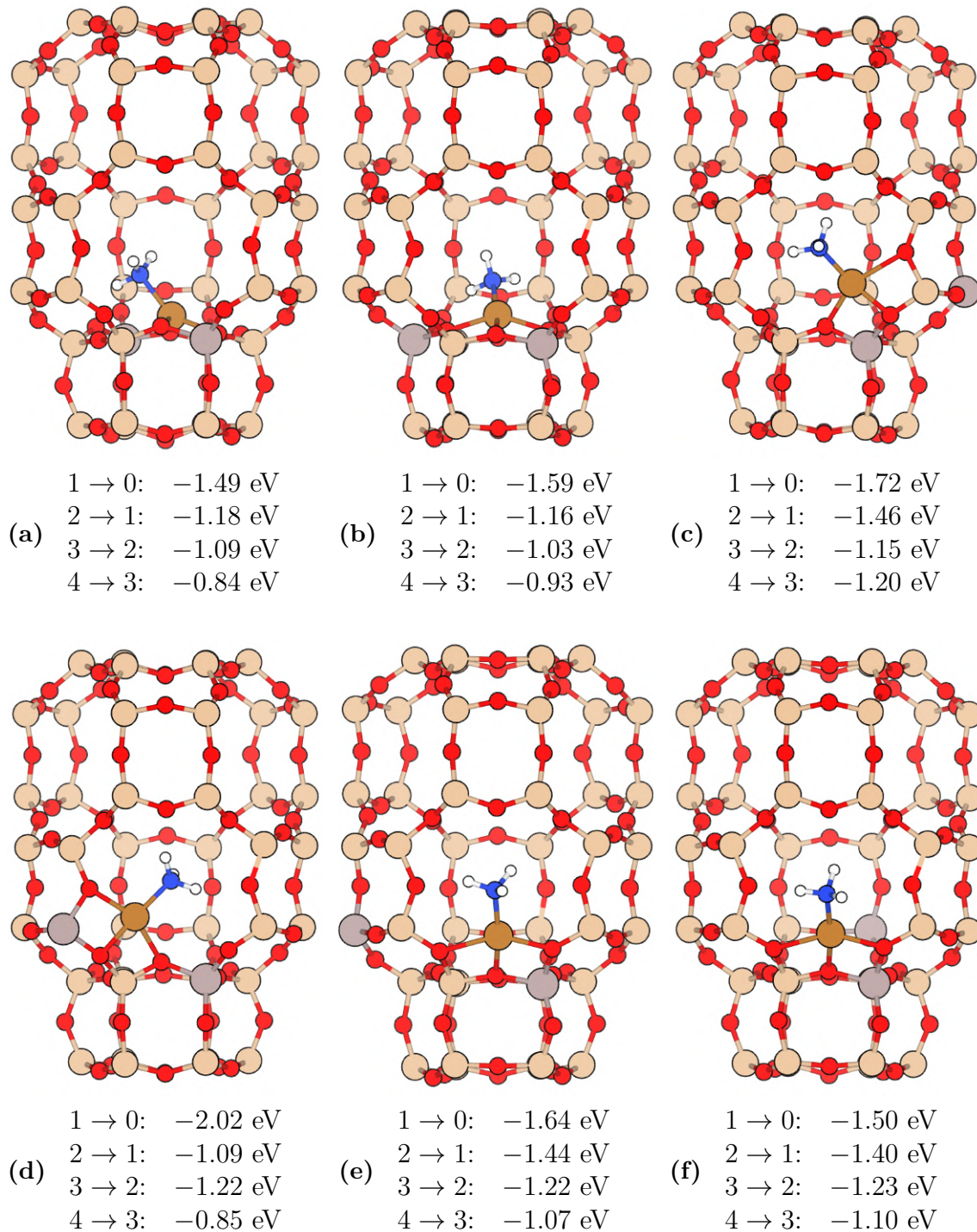


**Figure 5.33:** The lowest energy configurations for dopant distributions a-f with one  $\text{NH}_3$  adsorbed to the structures. Below each configuration are the adsorption energies of  $\text{NH}_3$  for the considered distributions.

The adsorption energies of  $\text{NH}_3$  in all considered structures are presented in figure 5.34.

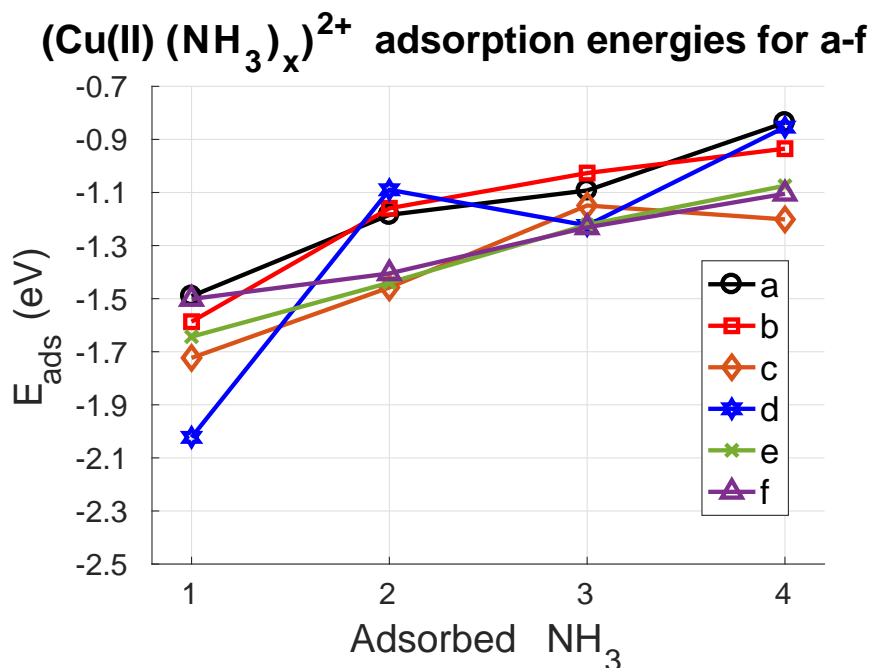


**Figure 5.34:** The sequential adsorption energies of  $\text{NH}_3$  for dopant distributions a-f.

It is clear that the positions of the dopant atoms relative to each other have a clear impact on the adsorption energies of  $\text{NH}_3$ . For distributions a and b, which were used for all dopant atoms in CHA and AIPO in section 5.5, respectively, the adsorption energies are overall lower than for all other dopant distributions in this sub category. One reason for this is that the lone  $\text{Cu(II)}$  counter ion is very stable in the six-membered ring when there are two dopant atoms there.

For distribution d, the adsorption energy of the first  $\text{NH}_3$  molecule is  $-2.02$  eV. This means that the configuration in figure 5.33d, with the  $\text{Cu(II)}$  counter ion bound to three O atoms next to dopant atoms and the  $\text{NH}_3$  molecule opposite one of the O atoms, is very favourable. This type of configuration is not possible if both dopant atoms are in the six-membered ring or in distribution c, e or f.

The lowest energy configurations for distributions g-l of the second Al dopant atom with one  $\text{NH}_3$  adsorbed are presented in figure 5.35. Included below each configuration are each of the  $\text{NH}_3$  adsorption energies for the dopant distributions.

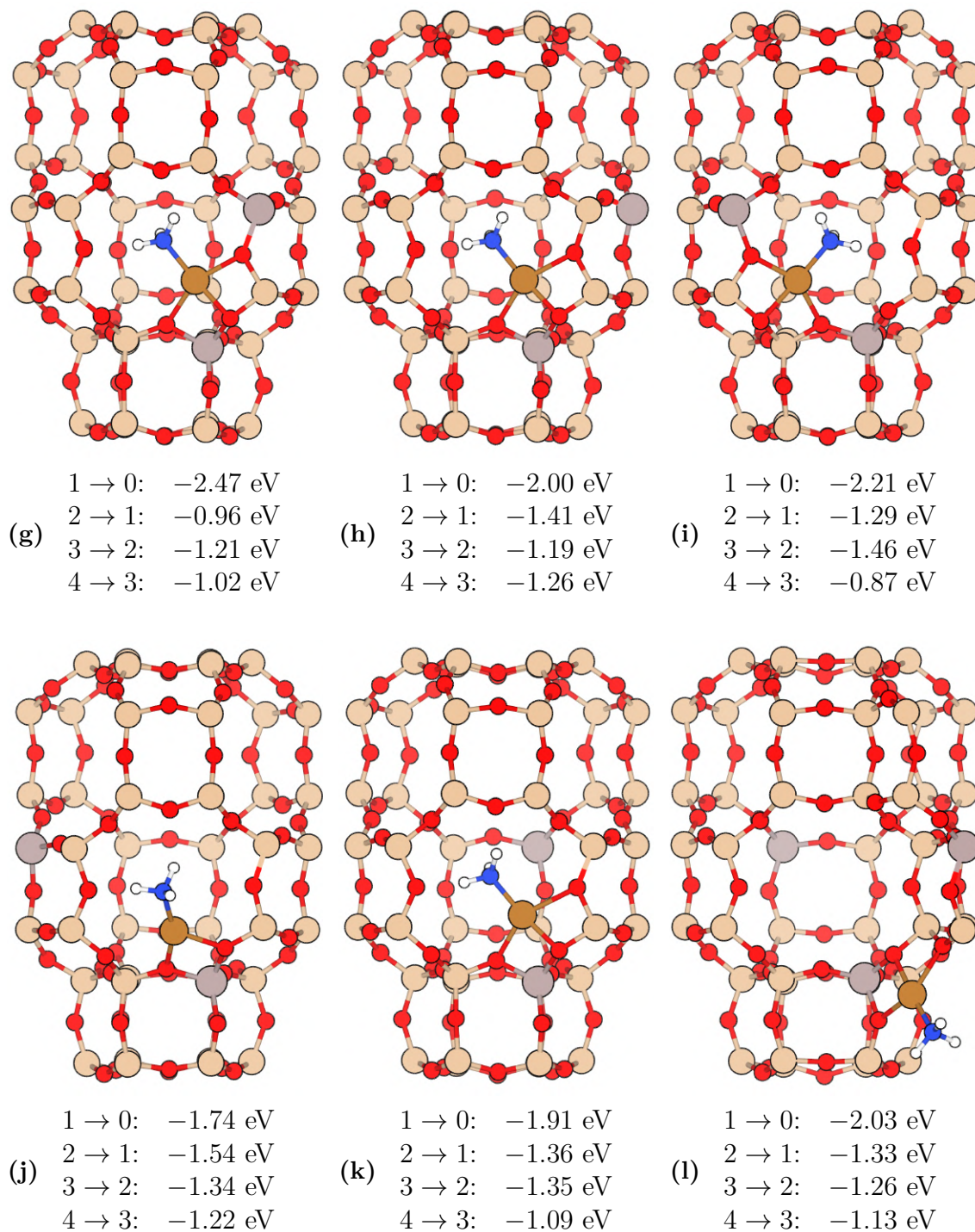


**Figure 5.35:** The lowest energy configurations for dopant distributions g-l with one  $\text{NH}_3$  adsorbed to the structures. Below each configuration are the adsorption energies of  $\text{NH}_3$  for the considered distributions.

The adsorption energies of  $\text{NH}_3$  in all considered structures are presented in figure 5.36.

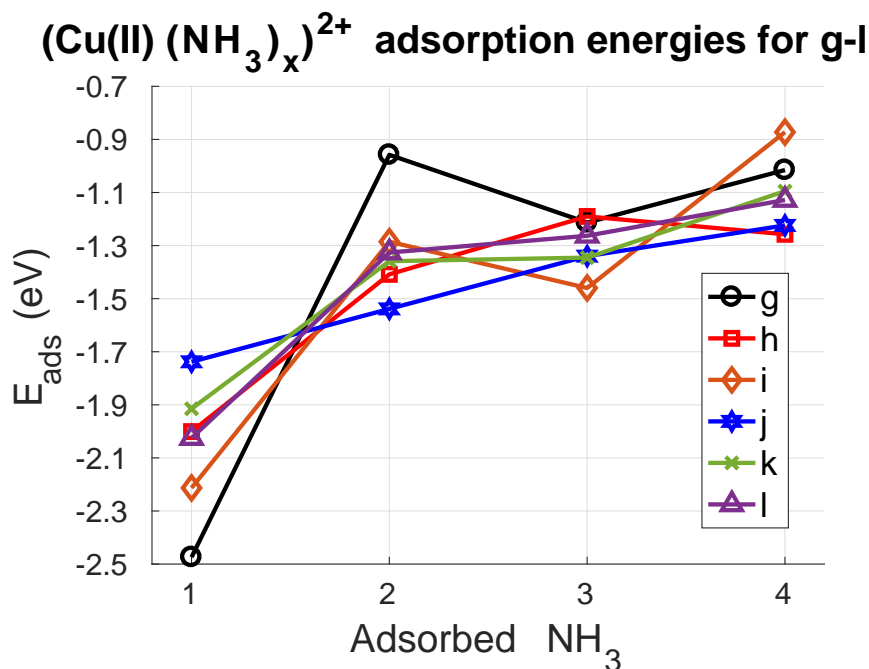


**Figure 5.36:** The sequential adsorption energies of  $\text{NH}_3$  for dopant distributions g-l.

The importance of dopant distribution becomes even clearer for sub category two than for sub category one. Here, the spread of the adsorption energies are even greater. It is mainly the adsorption energies of the first  $\text{NH}_3$  molecules that differ, which implies that there are great differences in how energetically favourable the structures with zero and one adsorbed  $\text{NH}_3$  molecules are for different distributions.

The highest adsorption energy of the entire thesis is  $-2.47$  eV, for adsorption of the first  $\text{NH}_3$  molecule in distribution g. As stated about distribution d in figure 5.33d,  $\text{Cu(II)}$  bonding to three O atoms next to the dopant atoms with  $\text{NH}_3$  opposite of an O atom is very favourable for the configurations with one adsorbed  $\text{NH}_3$ . The adsorption energies of the first  $\text{NH}_3$  are even higher for distributions g-l, than for distributions a-f, due to the increased distance between the dopant atoms making the lowest energy positions of only  $\text{Cu(II)}$  less energetically favourable.

The extra dopant atom to the left in figure 5.35l is not part of the cage, instead it is the periodic image of the second dopant atom. It is included in the figure since it is clear that the  $\text{Cu(II)}$  counter ion is influenced by it and binds closer to it than the periodic dopant atom in the cage. Distribution l is the only case where the influence of the periodic dopant atom is so substantial, but it should not be completely disregarded for any configuration.

The lowest energy configurations for distributions m-q with one  $\text{NH}_3$  adsorbed are presented in figure 5.37. Included below each configuration are each of the  $\text{NH}_3$

adsorption energies for the dopant distributions.

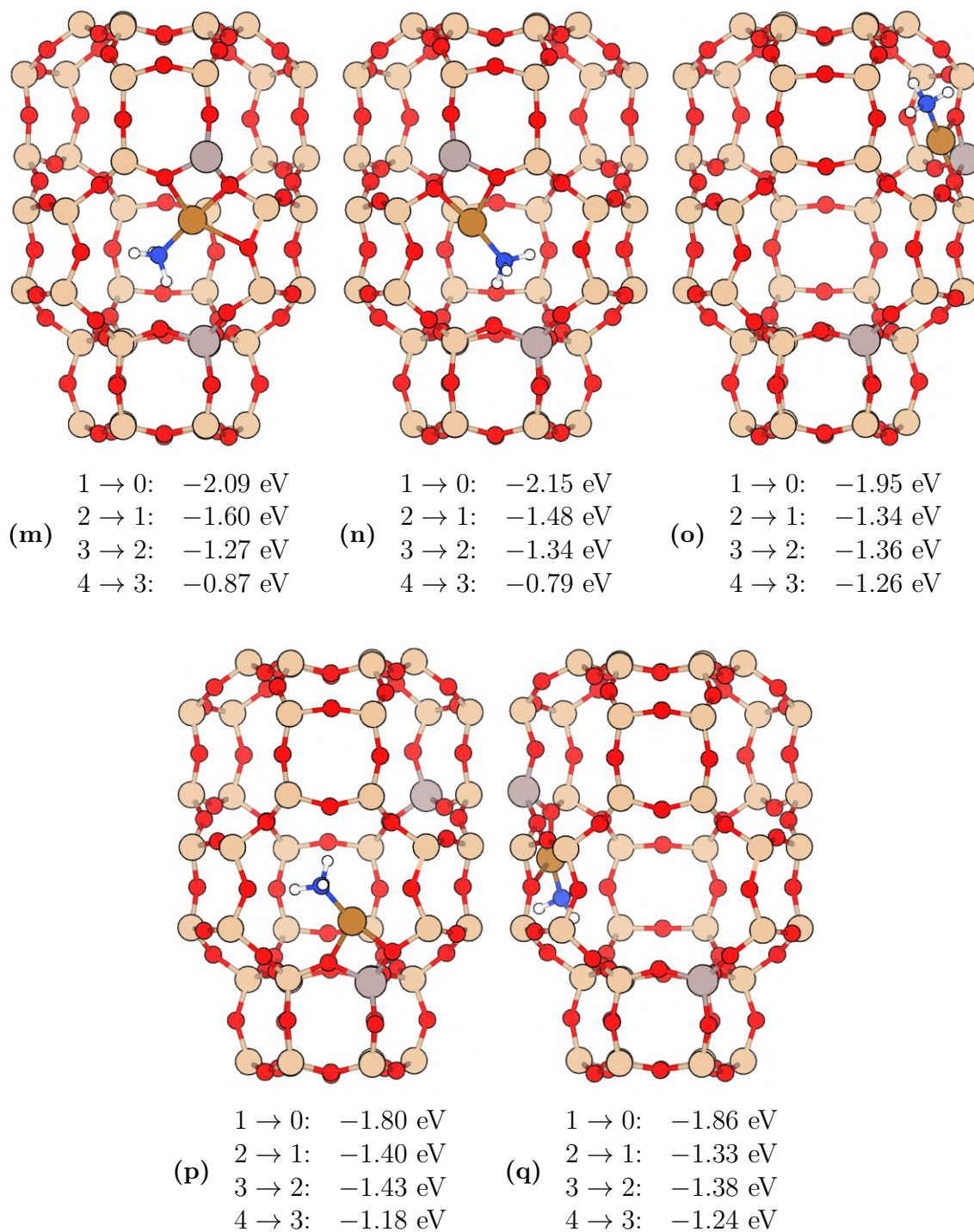


**Figure 5.37:** The lowest energy configurations for dopant distributions m-q with one  $\text{NH}_3$  adsorbed to the structures. Below each configuration are the adsorption energies of  $\text{NH}_3$  for the considered distributions.

The adsorption energies of  $\text{NH}_3$  in all considered structures are presented in figure 5.38.

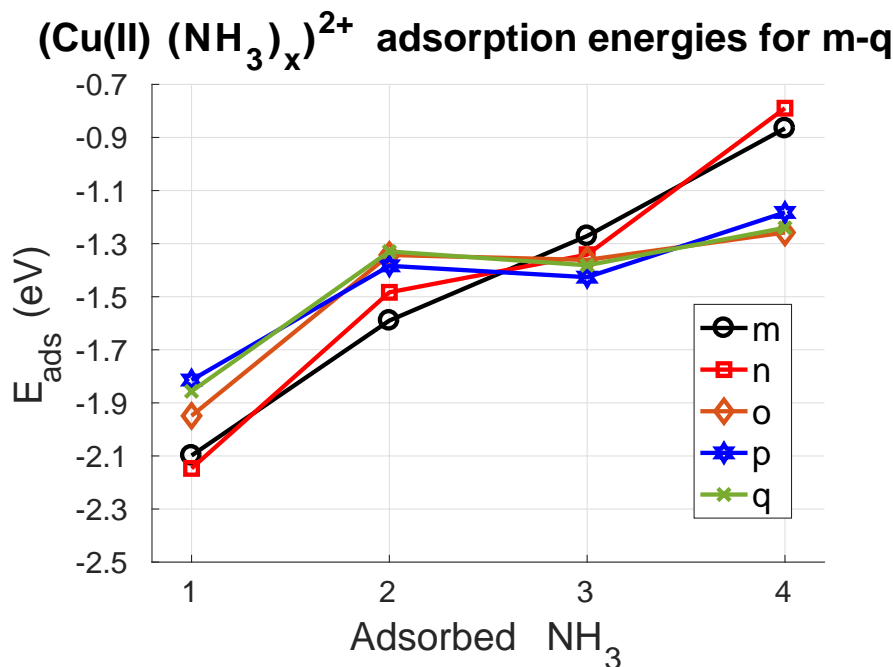


**Figure 5.38:** The sequential adsorption energies of  $\text{NH}_3$  for dopant distributions m-q.

Compared to distributions a-l, the differences are smaller between the adsorption energies of distributions m-q. One can divide this sub category further by recognising that for distributions m and n both dopant atoms are in the same eight-membered ring, while for distributions o-q they are not. The adsorption energies are very similar for m and n and for o, p and q. This shows that for dopant atoms placed far enough from each other, their exact positions do not have a large impact on the  $\text{NH}_3$  adsorption energies.

### 5.7.1 General properties of the dopant distributions

Like for the  $(\text{Cu(II)}(\text{NH}_3)_x)^{2+}$  complexes considered in section 5.5, the lowest energy positions of  $\text{Cu(II)}$  to  $(\text{Cu(II)}(\text{NH}_3)_3)^{2+}$  are adsorbed to the zeolites while the  $(\text{Cu(II)}(\text{NH}_3)_4)^{2+}$  is not. Distribution g is the only distribution for which  $\text{Cu(II)}$  without any  $\text{NH}_3$  adsorbed has its lowest energy position outside of a six-membered ring, instead it is in the same position that it is adsorbed to in figure 5.35g.

As visualized in figures 5.33, 5.35 and 5.37, the lowest energy positions of the  $(\text{Cu(II)}\text{NH}_3)^{2+}$  complex varies for different dopant atom distributions. But a similarity between all of them, except distributions a and b, are that the N of the  $\text{NH}_3$  molecule binds so that it is opposite of an O atom of the zeolite bound to the  $\text{Cu(II)}$  counter ion. The reason for this not being the case for distributions a and b is likely that sitting in the six-membered ring when there are two dopant atoms there is very energetically favourable. The six-membered ring is then in the way of  $\text{NH}_3$  being

able to bind opposite of an O atom.

The lowest energy positions of the  $(\text{Cu(II)})(\text{NH}_3)_2^{2+}$  complex varies considerably between different dopant distributions. However, there are only two lowest energy shapes of the complex. The positions for dopant distributions h and i are some of the most common and are presented in figure 5.39. Noteworthy is that for multiple dopant distributions there are other positions of the complex that are within about 0.02 eV of the lowest energy one.

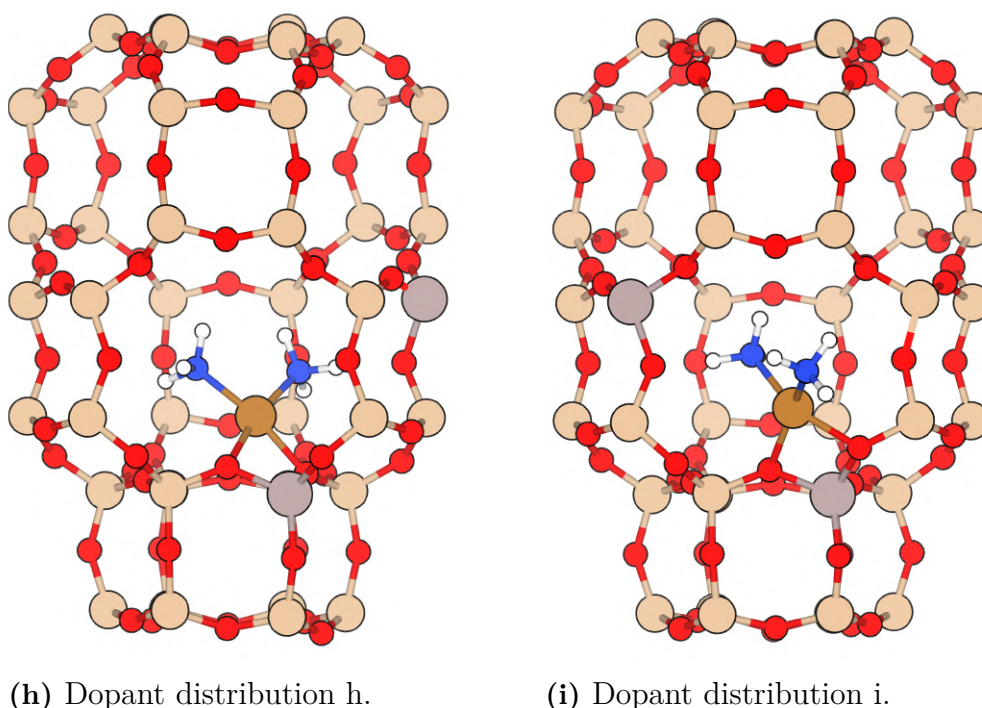


**Figure 5.39:** Lowest energy configurations of  $(\text{Cu(II)})(\text{NH}_3)_2^{2+}$  for dopant distributions h and i.

In figure 5.39h the  $\text{NH}_3$  are opposite of O atoms of the zeolite, forming a planar structure. In figure 5.39i they form a semi-tetrahedral structure with the O atoms. The  $(\text{Cu(II)})(\text{NH}_3)_2^{2+}$  complex takes one of these two shapes also in BEA, MFI and AIPO, as visualized in figures 5.25a and 5.25b in section 5.5. Thus, it is safe to say that the planar or semi-tetrahedral shapes are the lowest energy ones in most cases. The structure is only semi-tetrahedral if other atoms of the zeolite block it from being planar, so the most favourable shape is probably the planar.

The lowest energy positions of the  $(\text{Cu(II)})(\text{NH}_3)_3^{2+}$  complex for dopant distributions b and c are presented in figure 5.40. For all other dopant distributions, except distribution a in figure 5.21, the lowest energy positions of the complex are as in figure 5.40b. The shape of the complex is the same as in figure 5.25c, for all dopant distributions.

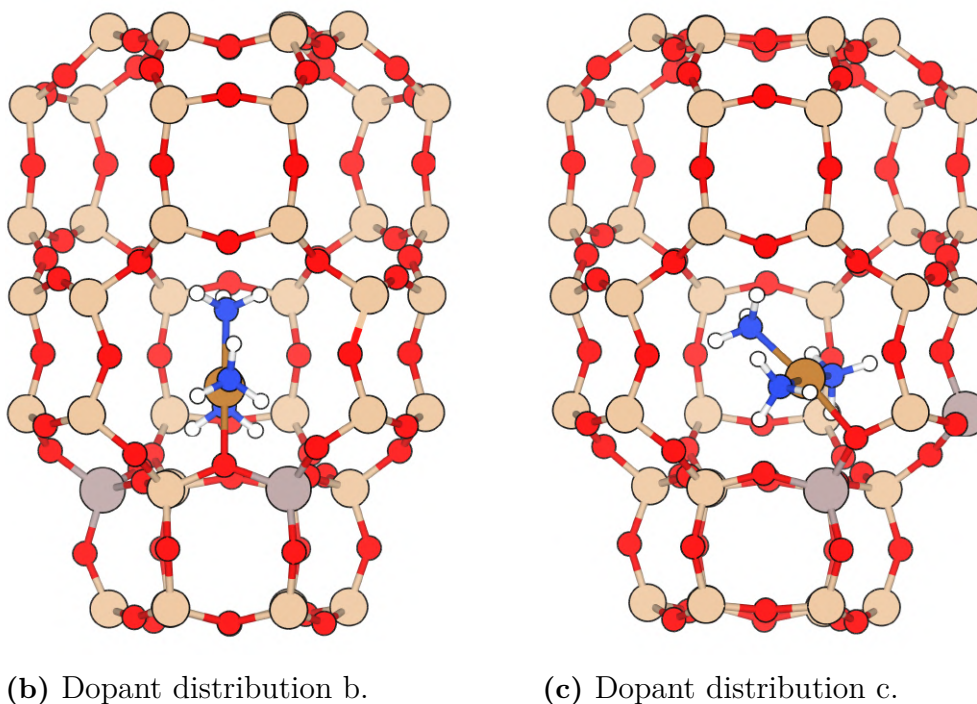


**Figure 5.40:** Lowest energy configurations of  $(\text{Cu(II)}(\text{NH}_3)_3)^{2+}$  for dopant distributions b and c.

For all dopant distributions, the lowest energy  $(\text{Cu(II)}(\text{NH}_3)_4)^{2+}$  complex is floating free within the zeolite pores and is shaped as in figure 5.25d.

The number of O-Cu bonds for all considered dopant distributions are presented in table 5.7.

**Table 5.7:** Number of O bonds to a Cu(II) counter ion for different distributions of Al dopant atoms in CHA with zero to four adsorbed  $\text{NH}_3$ .

	0 $\text{NH}_3$	1 $\text{NH}_3$	2 $\text{NH}_3$	3 $\text{NH}_3$	4 $\text{NH}_3$
a, b, c, d, e, f, h, i, j, k, l, m, q	4	3	2	1	0
g	3	3	2	1	0
n, o, p	4	2	2	1	0

Distribution g is the only case of the lone Cu(II) counter ion only being bound to three O atoms since it is not positioned in a six-membered ring. However, all lone Cu(II) counter ions that have its lowest energy position in a six-membered ring are bound to four O atoms. Regarding the number of bonds with one  $\text{NH}_3$  adsorbed, there are many cases where the longest bond is more than  $2.35 \text{ \AA}$ , while for distributions n, o and p the distance to the closest non-bonding O atom is close to  $2.4 \text{ \AA}$ . So there is only a small difference between distributions n, o and p, compared to the other ones. It is however clear that the  $(\text{Cu(II)}(\text{NH}_3))^{2+}$  complex is more loosely bound to the zeolite for a longer distance between the dopant atoms.

### 5.7.2 Phase diagrams for different Al distributions

Phase diagrams for  $(\text{Cu(II)(NH}_3)_x)^{2+}$  phases were calculated for dopant distributions a, d, g and q. They are presented in figure 5.41.

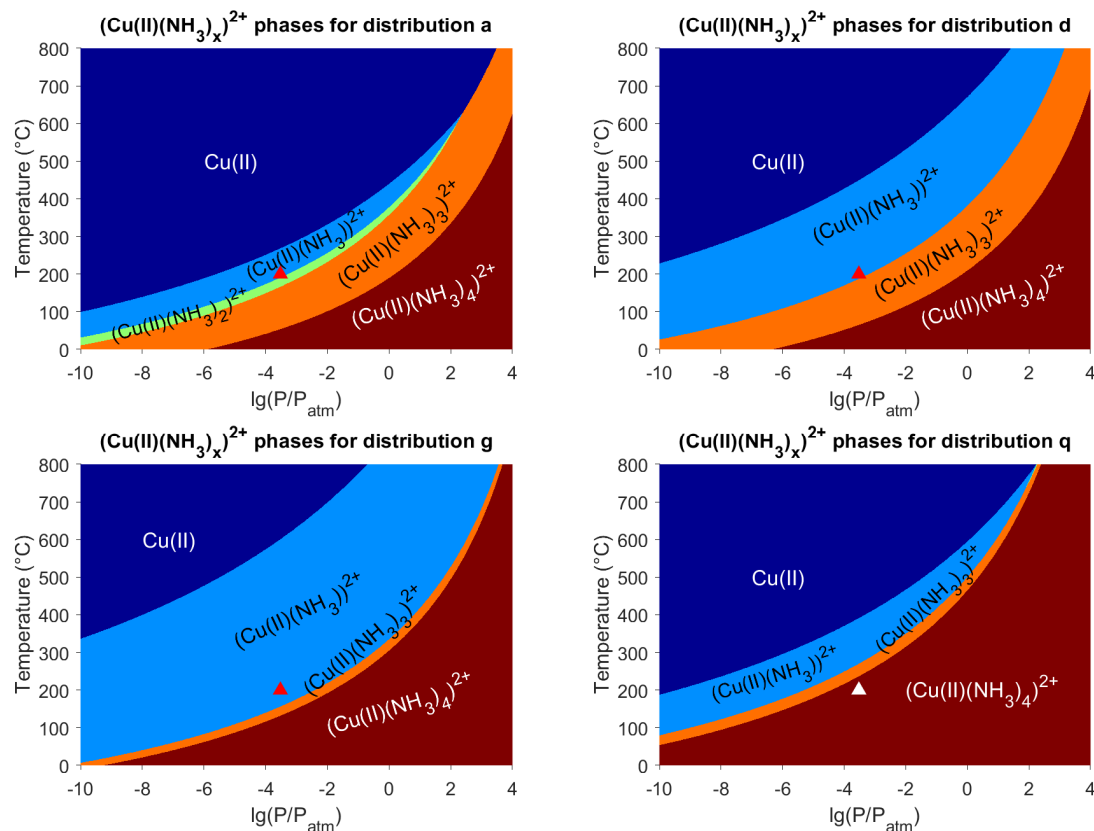
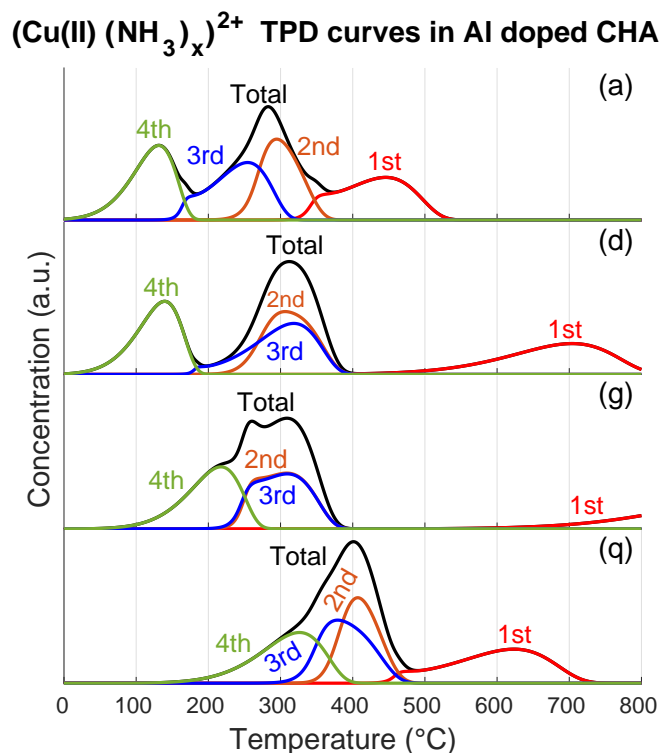


**Figure 5.41:**  $(\text{Cu(II)(NH}_3)_x)^{2+}$  phase diagrams for Al distributions a, d, g and q in CHA. The triangle indicates standard operating conditions at 300 ppm  $\text{NH}_3$  and a temperature of 200 °C.

The dopant distribution has a large impact on the preferred phases at different temperatures and pressures. For distribution g, the phase with one adsorbed  $\text{NH}_3$  is preferred even at very high temperatures and low pressures. For distribution q the phase with four adsorbed  $\text{NH}_3$  is preferred even at standard operating conditions.

### 5.7.3 TPD curves for different Al distributions

TPD curves for desorption of the fourth, third, second and first  $\text{NH}_3$  molecules bound to  $\text{Cu(II)}$  counter ions were calculated for distributions a, d, g and q. The starting configurations were fully loaded with four  $\text{NH}_3$  adsorbed to every  $\text{Cu(II)}$  counter ion. The concentrations for each sequential desorbed  $\text{NH}_3$  and their corresponding total concentrations of desorbed  $\text{NH}_3$  from the  $\text{Cu(II)}$  counter ions are presented in figure 5.42.

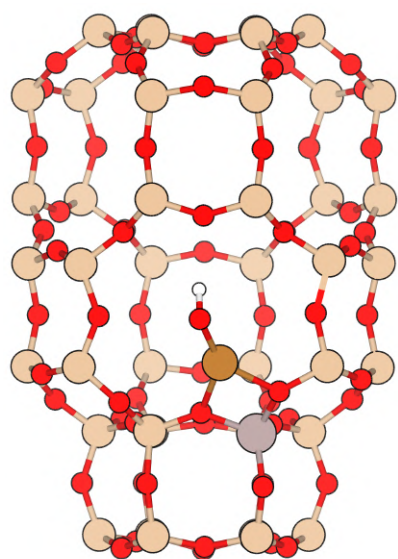
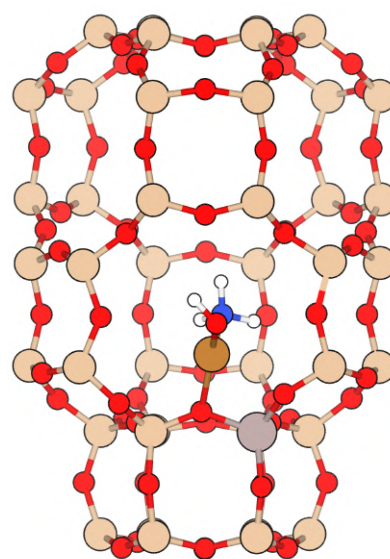


**Figure 5.42:** TPD curves for desorption of  $\text{NH}_3$  for Al distributions a, d, g and q in CHA.

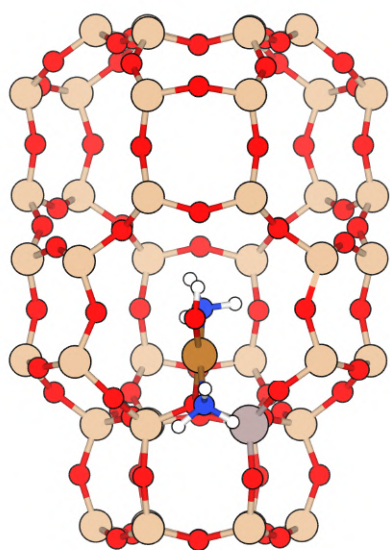
As indicated by the variety in adsorption energies for the different distributions, the TPD curves are clearly different. The adsorption energy of  $-2.47$  eV for distribution g is so high that the  $\text{NH}_3$  molecules stuck in this configuration do not desorb until at  $800^\circ\text{C}$ , which is where CHA starts to lose some of its catalytic capacity permanently [60]. This shows that too high adsorption energies are not desired.

## 5.8 $\text{NH}_3$ adsorption on $\text{Cu(II)}$ with $(\text{OH})^-$

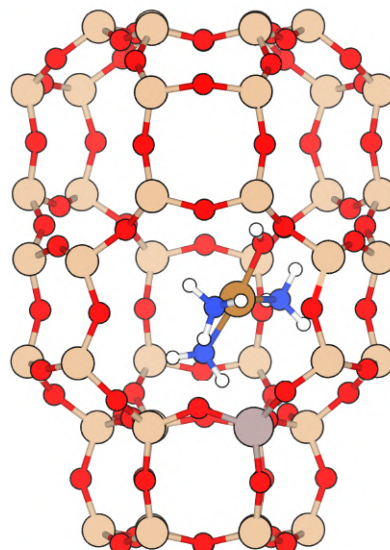
Up to three  $\text{NH}_3$  molecules were adsorbed to  $\text{Cu(II)}$  with  $(\text{OH})^-$  also adsorbed in CHA, BEA and MFI doped with Al, B, Ga and Fe and in AlPO doped with Si, Ti, Mg and Zn. The lowest energy configurations with zero to three adsorbed  $\text{NH}_3$  in Al doped CHA, BEA and MFI and Si doped AlPO are presented in figure 5.43, 5.44, 5.45 and 5.46, respectively. Below each structure are the adsorption energies of  $\text{NH}_3$ , for all considered dopant atoms, compared to the lowest energy structures with one less  $\text{NH}_3$ .

Cu(II) with  $(\text{OH})^-$  in CHA.

Al:  $-0.94$  eV  
 B:  $-0.86$  eV  
 $1 \rightarrow 0$ : Ga:  $-0.89$  eV  
 Fe:  $-0.94$  eV



Al:  $-1.10$  eV  
 B:  $-1.09$  eV  
 $2 \rightarrow 1$ : Ga:  $-1.09$  eV  
 Fe:  $-1.09$  eV



Al:  $-0.98$  eV  
 B:  $-0.89$  eV  
 $3 \rightarrow 2$ : Ga:  $-0.81$  eV  
 Fe:  $-0.78$  eV

**Figure 5.43:** The lowest energy positions of  $(\text{Cu(II)})(\text{OH})^-(\text{NH}_3)_x)^+$  complexes in Al doped CHA, with corresponding  $\text{NH}_3$  adsorption energies for all considered dopant atoms.

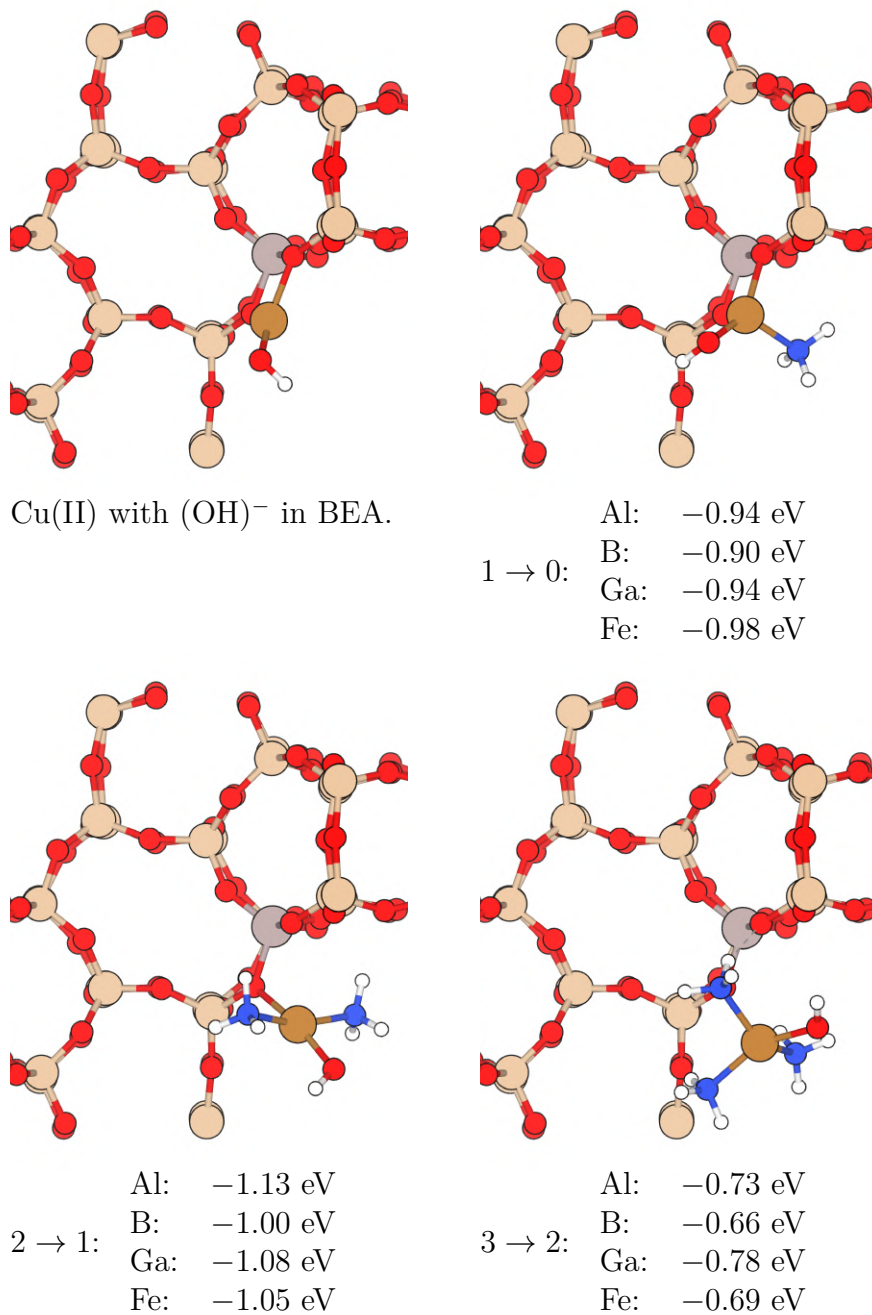


**Figure 5.44:** The lowest energy positions of  $(\text{Cu}(\text{II})(\text{OH})^-(\text{NH}_3)_x)^+$  complexes in Al doped BEA, with corresponding  $\text{NH}_3$  adsorption energies for all considered dopant atoms.

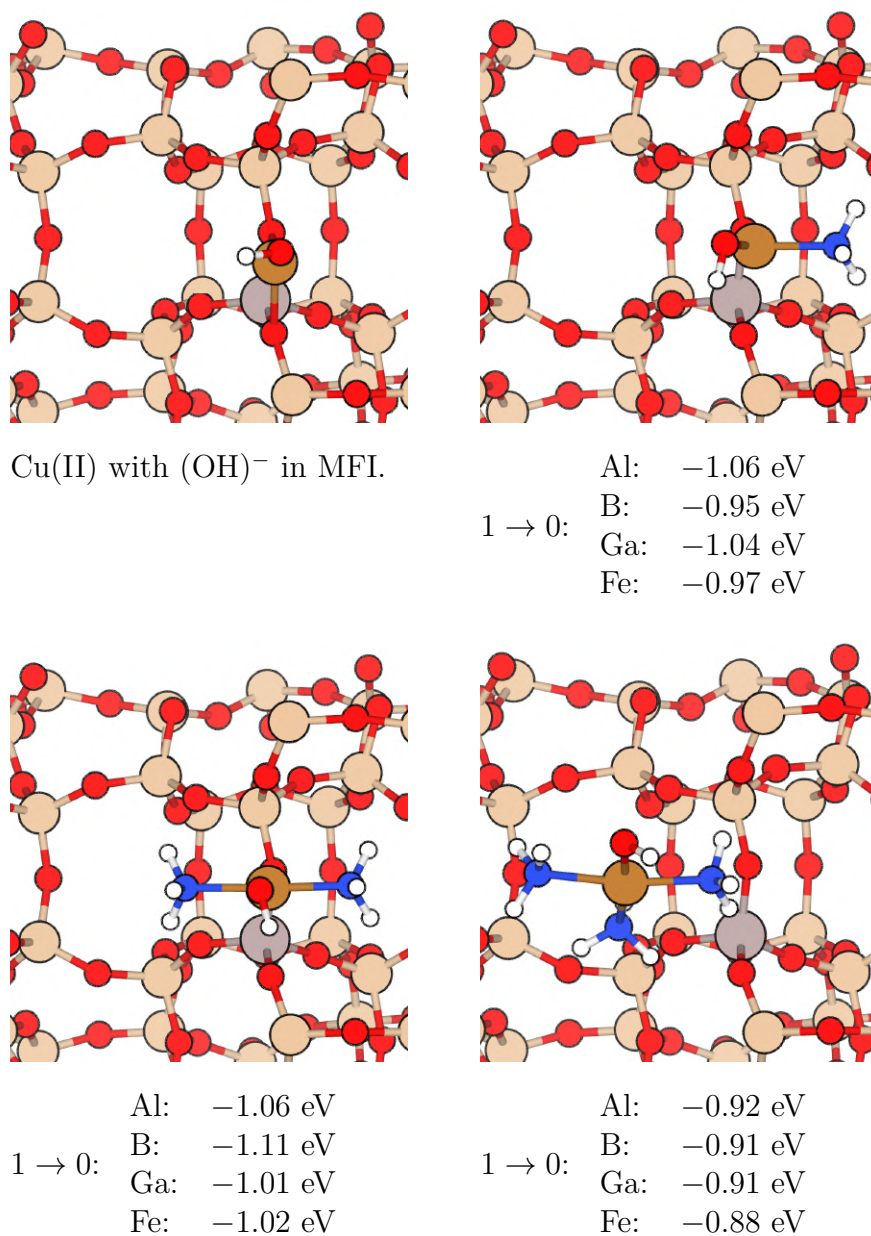


**Figure 5.45:** The lowest energy positions of  $(\text{Cu(II)})(\text{OH})^-(\text{NH}_3)_x)^+$  complexes in Al doped MFI, with corresponding  $\text{NH}_3$  adsorption energies for all considered dopant atoms.

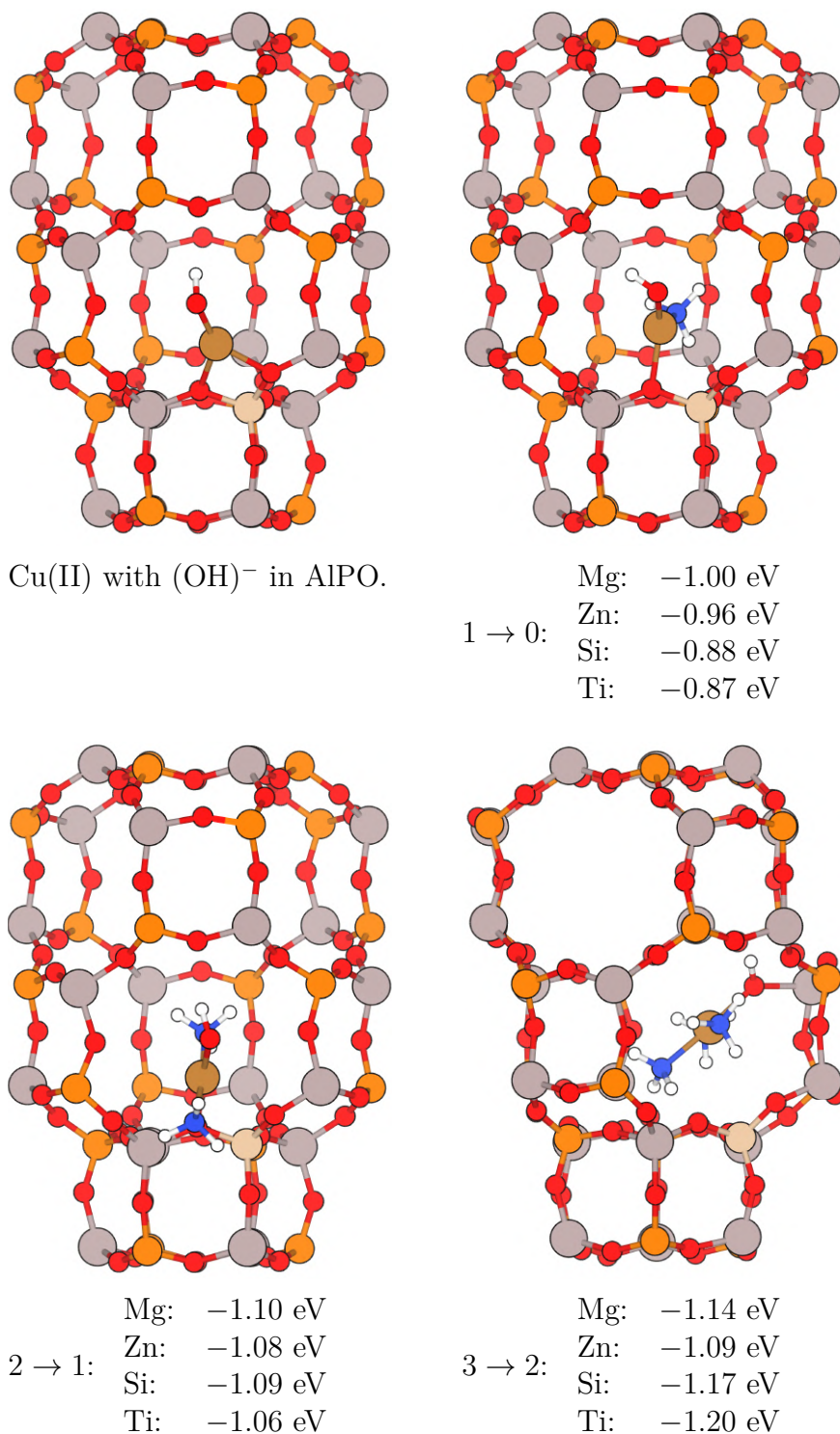


**Figure 5.46:** The lowest energy positions of  $(\text{Cu(II)}(\text{OH})^-(\text{NH}_3)_x)^+$  complexes in Si doped AlPO, with corresponding  $\text{NH}_3$  adsorption energies for all considered dopant atoms. The structure with the  $(\text{Cu(II)}(\text{OH})^-(\text{NH}_3)_3)^+$  complex is rotated  $30^\circ$  compared to the other ones.

In all considered structures,  $(\text{Cu(II)(OH)}^-)^+$  to  $(\text{Cu(II)(OH)}^-(\text{NH}_3)_2)^+$  are preferably adsorbed to the zeolite frameworks. The  $(\text{Cu(II)(OH)}^-(\text{NH}_3)_3)^+$  complex is free in CHA, BEA and MFI, while in AlPO it is not. This is because the O atom of the complex binds to an Al atom of the AlPO, as visualized in figure 5.46. The  $(\text{Cu(II)(OH)}^-(\text{NH}_3)_x)^+$  complexes are shaped and bound to the structures as described in figure 5.47, except in Ga and Fe doped MFI, in which  $(\text{Cu(II)(OH)}^-(\text{NH}_3))^+$  is bound to two O atoms of the zeolite. However, in Al and B doped MFI the Cu(II) counter ion of the  $(\text{Cu(II)(OH)}^-(\text{NH}_3))^+$  complex is close to being bound to one more O atom, since the distances between the atoms in question are about 2.4 Å.

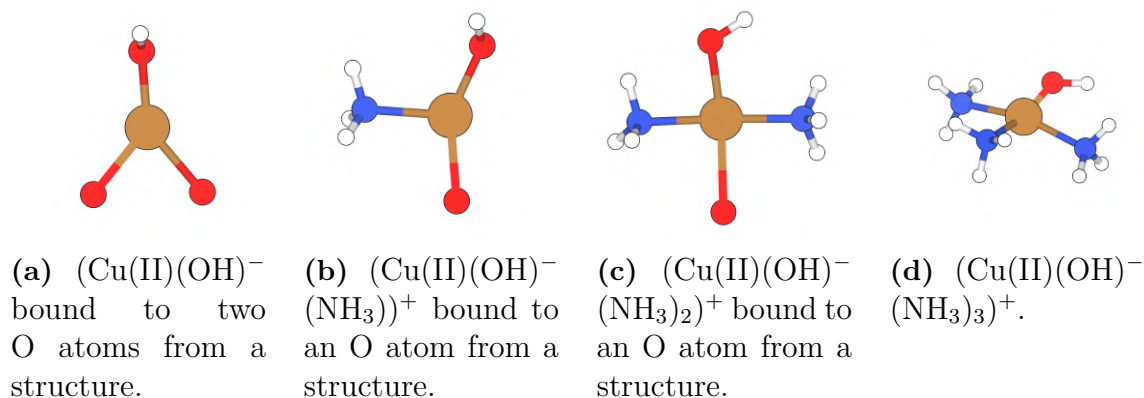


**Figure 5.47:**  $(\text{Cu(II)(OH)}^-(\text{NH}_3)_x)^+$  complexes in the structures.

The number of O-Cu bonds in all considered structures are presented in table 5.8.

**Table 5.8:** Number of O bonds to a Cu(II) counter ion with  $(\text{OH})^-$  adsorbed in CHA, BEA, MFI and AlPO for all considered dopant atoms with zero to three adsorbed  $\text{NH}_3$ . The bond to the O atom of  $(\text{OH})^-$  is not included.

	0 $\text{NH}_3$	1 $\text{NH}_3$	2 $\text{NH}_3$	3 $\text{NH}_3$
CHA	2	1	1	0
BEA	2	1	1	0
MFI-Al/B	2	1	1	0
MFI-Ga/Fe	2	2	1	0
AlPO	2	1	1	0

Again, in the case of there being a different number of bonds for different dopant atoms within the same structure, the distances between the considered atoms are around 2.4 Å.

The adsorption energies of  $\text{NH}_3$  in all considered structures are presented in figure 5.48. The adsorption energies are relatively close for the different types of dopant atoms. The adsorption energies of the second  $\text{NH}_3$  are the highest in most of the zeolites, while the adsorption energies of the third are the highest in AlPO because of the O atom of the complex binding to Al of the AlPO structure being very energetically favourable.

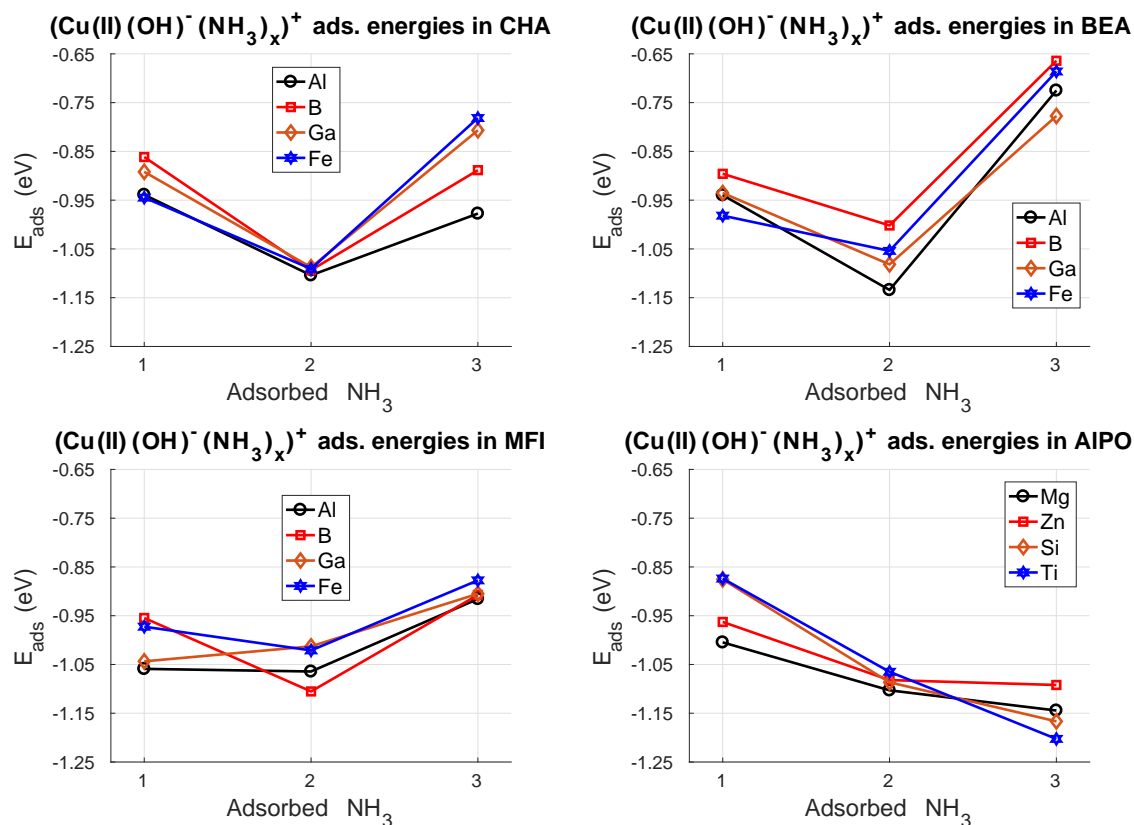


**Figure 5.48:** The sequential adsorption energies of  $\text{NH}_3$  on  $\text{Cu(II)}$  with  $(\text{OH})^-$  adsorbed for all considered dopant atoms in CHA, BEA, MFI and AIPO.

## 5.9 Possibility of $\text{H}_2\text{O}$ dissociation

In all 17 CHA distributions, BEA and MFI with two Al dopant atoms and AIPO with two Si dopant atoms, the lowest energy configurations of  $\text{H}_2\text{O}$  and  $\text{H}_2\text{O}$  dissociated into OH and H were compared. For dissociated  $\text{H}_2\text{O}$ , H should create a Brønsted site and OH should adsorb to the  $\text{Cu(I)}$  counter ion. The OH would then gain one electron, recreating the situation in section 5.8, with  $(\text{OH})^-$  adsorbed to  $\text{Cu(II)}$ . Assuming a similar behaviour to  $\text{NH}_3$  adsorption, the results should be about the same for the other dopant atoms.

In the dopant configurations with a negative dissociation energy,  $(\text{OH})^-$  adsorbed to  $\text{Cu(II)}$  should be more common than in the configurations with positive dissociation energy. If  $(\text{OH})^-$  adsorbed to  $\text{Cu(II)}$  is energetically favourable, it could be a competitor to  $\text{NH}_3$  adsorption on  $\text{Cu(II)}$  in those dopant configurations.  $\text{H}_2\text{O}$  should not be a strong competitor to  $\text{NH}_3$  adsorption on  $\text{Cu(II)}$ , since  $\text{NH}_3$  is a stronger base than  $\text{H}_2\text{O}$ .

In all considered configurations, the lowest energy positions of  $\text{H}_2\text{O}$  on  $\text{Cu(II)}$  are the same as the lowest energy positions of  $\text{NH}_3$  on  $\text{Cu(II)}$ , presented on sections 5.5 and 5.7, with a few exceptions. In the lowest energy positions of OH and H,  $(\text{OH})^-$  is

adsorbed to Cu(II) at one dopant atom, as in section 5.8, and H creates a Brønsted site at the other dopant atom. The lowest energy configurations of H<sub>2</sub>O and of OH and H in Al doped BEA are presented in figure 5.49a and 5.49b, respectively.

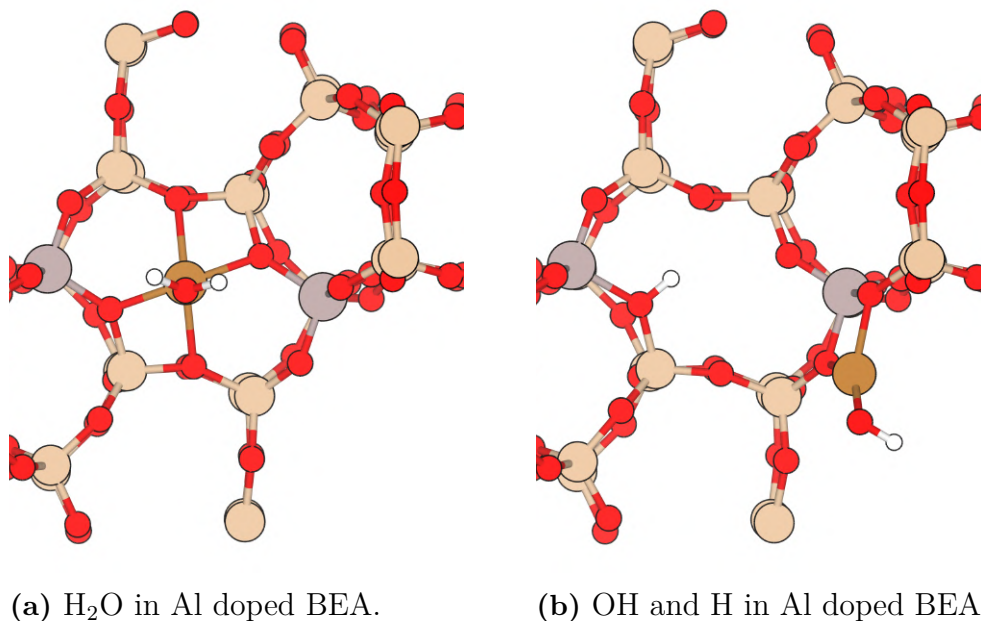


**Figure 5.49:** Lowest energy configurations of H<sub>2</sub>O and of OH and H in Al doped BEA.

The dissociation energies of H<sub>2</sub>O into OH and H in all considered configurations are presented in table 5.9.

**Table 5.9:** Dissociation energy of H<sub>2</sub>O into OH and H in Al doped CHA, BEA and MFI and Si doped AIPO.

Structure	$E_{\text{dis}}$ (eV)	Structure	$E_{\text{dis}}$ (eV)	Structure	$E_{\text{dis}}$ (eV)
CHA-a	0.64	CHA-h	0.14	CHA-o	0.05
CHA-b	0.58	CHA-i	0.44	CHA-p	0.01
CHA-c	0.15	CHA-j	0.03	CHA-q	-0.07
CHA-d	0.65	CHA-k	0.06	BEA	0.42
CHA-e	0.02	CHA-l	0.19	MFI	0.23
CHA-f	0.06	CHA-m	0.26	AIPO	0.60
CHA-g	0.77	CHA-n	0.33		

In all cases except distribution q in CHA, H<sub>2</sub>O dissociation is not energetically favourable and in distribution q, the dissociation energy is very small. This means that (OH)<sup>-</sup> originating from H<sub>2</sub>O adsorbed to Cu(II) should be rare and that adsorption of NH<sub>3</sub> should dominate in all considered dopant configurations.

When the (Cu(II)(H<sub>2</sub>O))<sup>2+</sup> complex can bind to O atoms next to both dopant atoms, dissociation is very unfavourable, with dissociation energies above 0.4 eV.

## 5. Results

---

In the cases where the dopant atoms are far from each other, dissociation is more favourable. This is because  $(\text{Cu(II)(H}_2\text{O)})^{2+}$  in that case can not bind to O atoms next to both dopant atoms, while  $(\text{Cu(II)(OH)}^-)^+$  and  $\text{H}^+$  can bind to O atoms next to one dopant atom each.

# 6

## Discussion

In this chapter the advantages and disadvantages of the methods used and possible alternative methods are discussed. The results, how well they correspond to previous studies and the possible implications of them are also discussed. Lastly possible further work that can build upon the obtained results is presented.

### 6.1 Thoughts on the methods used

#### 6.1.1 Finding the global minima

In order to find the global potential energy minimum positions of the atomic complexes, many different starting positions had to be tested. Up to eight different starting positions were tested for all considered atomic complexes in every considered structure. The structures were then relaxed using the conjugate gradient method [43]. Given that a counter ion-NH<sub>3</sub> complex was oriented in roughly the right direction and had no atoms of the zeolite in the way, it would converge to the same position independent of starting starting position.

The starting configurations were chosen by inspection. A drawback of this method is that lower energy positions can have been missed. However, a great effort was put into testing every possible minimum that could be found, especially in CHA and AIPO, where the computational times were reasonably short. In BEA and MFI, the positions tested were of similar nature to the ones that were found to be the global minima in CHA and AIPO.

Other ways in which the potential energy surfaces could have been probed include molecular dynamics using molecular dynamics [86]. The computational time needed to probe the surfaces this way would however be too long considering the number of time steps needed, especially in BEA and MFI. An even better option than molecular dynamics would have been Monte-Carlo sampling [87]. However, since the minima were quite easy to find by inspection, the conjugate gradient method was the preferred method, even in hindsight.

#### 6.1.2 Effect of local minima

During desorption of NH<sub>3</sub> from a complex at a global potential energy minimum, it is very hard to know if the complex will stick in the same position or move to its

new global minimum. If the case is that the complex sticks to the local minimum, the adsorption energy should be calculated from the energies at that local minimum, and not the global minima. One situation where the calculated global minima are distanced far from each other are the  $(\text{Cu(II)(NH}_3)_x)^{2+}$  complexes for Al dopant distribution a in CHA in figure 5.21.

If one were to consider the adsorption energies at different local minima of the structures, one would end up with as many quartets of adsorption energies in the structures. More effort has to be put into investigating the barriers of diffusion for the complexes moving from local to global minima. This could be done by using molecular dynamics [86]. But assuming that the complexes diffuse over the barriers during the desorption processes at standard operating conditions, the calculated adsorption energies are sufficient.

### 6.1.3 Treatment of entropy in the structures

As explained in section 4.2.2, treating the entropy of the complexes in the structures is difficult. Considering only the vibrational entropy of the atomic complexes is better than considering no entropy at all, but more sophisticated approaches could be made. For example one could use Monte Carlo integration to obtain a better description of the entropy [88].

## 6.2 Thoughts on the results

The results show that the adsorption energies in zeolites can be tuned by changing the zeolite frameworks or dopant atoms. However, what showed to change the adsorption energies the most was the positions of the dopant atoms relative to each other. It has been made clear that the dopant distribution should be of great consideration when synthesising zeolites.

### 6.2.1 Consistency of the results

The calculated lowest energy configurations are in most cases consistent with each other. For example, the  $(\text{Cu(I)(NH}_3))^+$  complex is adsorbed to the zeolite or AIPO surfaces, while the  $(\text{Cu(I)(NH}_3)_2)^+$  complex is not. The  $(\text{Cu(II)(NH}_3)_2)^{2+}$  complex binds in two different ways to the structures, it either forms in planar or semi-tetrahedral structure with two O atoms. In most cases, the number of O-Cu bonds are the same for different dopant atoms within the same frameworks. In the cases when the number of bonds are different, the atoms in question are about 2.4 Å from each other.

With Cu(II) as a counter ion, the differences in adsorption energies for different dopant atoms can be explained by the differences in the shapes of the lowest energy configurations of the structures. Some differences are visualized in figure 5.27 and 5.28. For  $\text{H}^+$  and Cu(I), a linear relationship between the adsorption energy of  $\text{NH}_3$  and the bond order of the O-H/Cu bonds was found when exchanging dopant atoms.

For  $\text{H}^+$ , a linear relationship was also found between the adsorption energy of  $\text{NH}_3$  and the OH frequency shift upon CO adsorption.

The frequency shift upon CO adsorption on a Cu counter ion was not applicable because of CO adsorbing close to the Cu ion, displacing it from its lowest energy position without CO present and breaking some of its bonds to O atoms, contrary to adsorption at Brønsted sites, where to  $\text{H}^+$  counter ion was only displaced somewhat. It was also found that only the bond orders presented in section 5.3.1 and 5.4.1 could be related to adsorption energies of  $\text{NH}_3$ . In other cases, the Cu counter ions bound to more than one O atom, which made relating them to adsorption energies difficult. Other approaches, such as relating the sum of all bond orders for selected atoms also proved unsuccessful.

## 6.2.2 Comparison to previous studies

Comparisons to previous DFT studies can be difficult due to differences in dopant configurations and exchange-correlation functionals. In reference [7], the adsorption energies of  $\text{NH}_3$  in Al doped CHA were obtained with the PBE-cx functional in the 36 atom and 288 atom unit cells. In the case of two dopant atoms in the unit cells, they were placed opposite each other in a six-membered ring, like in dopant distribution a.

In reference [7], the adsorption energy of a fourth  $\text{NH}_3$  on Cu(II) was calculated to be  $-1.59$  eV and  $-1.51$  eV for the different cells, while in this thesis it was calculated to only  $-0.84$  eV for dopant distribution a, which is the most comparable distribution. The other adsorption energies are within 0.2 eV of those obtained in reference [7]. The  $(\text{Cu(II)(NH}_3)_4)^{2+}$  complex is believed not to take part in the catalytic reaction cycle at low temperatures because of the high adsorption energy of the fourth  $\text{NH}_3$ . Among all dopant distributions, the highest adsorption energy of the fourth  $\text{NH}_3$  of the  $(\text{Cu(II)(NH}_3)_4)^{2+}$  complex is only  $-1.26$  eV, calculated for distributions h and o. So that the  $(\text{Cu(II)(NH}_3)_4)^{2+}$  complex does not take part in the reaction cycle at low temperatures might have to be reevaluated.

In reference [7], one experimental TPD peak at about  $290^\circ\text{C}$  is believed to stem from desorption of  $\text{NH}_3$  from  $(\text{Cu(I)(NH}_3)_2)^+$  while another experimental peak at about  $420^\circ\text{C}$  is believed to stem from desorption of  $\text{NH}_3$  from Brønsted sites,  $(\text{Cu(I)(NH}_3))^+$  and  $(\text{Cu(II)(NH}_3)_4)^{2+}$ . The adsorption energy of  $\text{NH}_3$  from the  $(\text{Cu(II)(NH}_3)_4)^{2+}$  complex for dopant distribution a calculated in this thesis is too low for that to be the case, but it is plausible that the other three desorption processes are causing the respective peaks. Due to the wide variety of adsorption energies of  $\text{NH}_3$  from  $(\text{Cu(II)(NH}_3)_x)^{2+}$  complexes calculated in this thesis, it is hard to appoint all of them to experimental TPD peaks. Some of the simulated dopant configurations were probably not present experimentally.

## 6.3 Connection to $\text{NO}_x$ reduction

The results of this thesis can hopefully aid in developing catalysts for low  $\text{NO}_x$  emissions. The wide variety of adsorption energies might make sure that there is  $\text{NH}_3$  available to react with  $\text{NO}_x$  also at high temperatures. First factors outside of  $\text{NH}_3$  adsorption, that has to be taken into account when designing the catalyst, are discussed. Then what distributions, of the ones considered, that have  $\text{NH}_3$  adsorption energies most suitable for SCR applications is discussed.

### 6.3.1 Stability of the structures

One of the most important factors of the structures is their stability. As stated in section 4.6.3, CHA, BEA, MFI and AIPO lose some of their catalytic capacities permanently at about 800 °C, 760 °C, 600 °C and 1000 °C, respectively [60, 61, 62, 63].

Even though AIPO can withstand high temperatures, it has bad structural stability in presence of  $\text{H}_2\text{O}$  vapor [89]. As a consequence, it can suffer from coke formation and pore blocking, which compromises its catalytic performance while also decreasing its lifetime [90]. In the simulations of  $(\text{Cu(II)(OH)}^-(\text{NH}_3)_3)^+$  in AIPO, it was found that the OH of the complexes bind to Al of the AIPO in the structures lowest energy configurations. This is visualized for Si doped AIPO in figure 5.46. So one likely way that the pores are blocked is by  $\text{H}_2\text{O}$  dissociating into H that adsorbs at Brønsted sites and OH that adsorbs to Al and mixes with O of the AIPO structure. With this in mind, CHA is probably the most stable structure of the ones considered.

Regarding the stability of the structures with respect to dopant atoms, B should probably be avoided. This because bonds between B and O atoms break when  $\text{H}^+$ ,  $\text{Cu(II)}$  or  $(\text{Cu(II)(NH}_3)_3)^{2+}$  are adsorbed to the B doped zeolites.

### 6.3.2 Effect of dopant distribution on $\text{NO}_x$ conversion

The most interesting finding of the thesis are the large differences in adsorption energies for different dopant distributions in CHA in section 5.7. Thus, it is critical that the dopant distribution actually can be controlled during the synthesis of zeolites. Previous studies have shown that an Al dopant distribution can be controlled in both CHA [16], BEA [17] and MFI [18, 19]. This means that it should be possible to tailor the dopant distribution so that  $\text{NH}_3$  adsorption energies that are preferred with respect to the operating conditions in an SCR catalyst are obtained.

In the TPD curve for distribution g of Al dopant atoms in CHA in figure 5.42, the first  $\text{NH}_3$  stays adsorbed even at temperatures way above SCR standard operating conditions, which results in it not taking part in the  $\text{NO}_x$  conversion. Thus,  $\text{NH}_3$  adsorption energies of  $-2.47$  eV are too high for SCR applications.  $\text{NH}_3$  desorption at temperatures way below standard operating conditions, as for the fourth  $\text{NH}_3$  in distribution a and d in figure 5.42, is also not ideal. For distribution q however, the fourth  $\text{NH}_3$  starts to desorb at 200 °C, followed by the third at 300 °C and the

second at 350 °C. Then the first NH<sub>3</sub> starts to desorb at 450 °C, which is about where there are no second and third NH<sub>3</sub> left. So for distribution q, NH<sub>3</sub> desorb at all temperatures between 200 °C and 700 °C. This can be compared to distribution a, where NH<sub>3</sub> desorb from 0 °C to 500 °C.

Temperatures of 700 °C are much higher than SCR operating conditions, but it should be preferred to have NH<sub>3</sub> adsorbed as a reserve, compared to it desorbing at lower temperatures. Therefore distribution q should be the best suited for SCR applications, compared to distributions a, d and g. Thus, among these four distributions, q should be aimed for during the synthesis. TPD curves could also be calculated for the other distributions, since 200 °C might be just too high of a temperature for NH<sub>3</sub> desorption to start taking place. However, one could have different dopant distributions in different parts of the zeolite, so that it as a whole is perfectly suited for SCR applications.

Another important part of reaction (1.1) is the dissociation of O<sub>2</sub>, on which the influence of the Al dopant distribution also has been studied [14]. One can then consider the effect on both NH<sub>3</sub> adsorption and O<sub>2</sub> dissociation energies when tailoring the dopant atom distribution.

## 6.4 Possible further work

As stated in section 6.1.2, calculating the diffusion barriers to the global minima are of great interest for a further understanding on from what minima the adsorption energies actually should be calculated.

Other ways in which this work could be expanded on is by testing different dopant distributions for all considered dopant atoms in all considered structures, and not just for Al in CHA. For BEA and MFI all positions of Si atoms are not equivalent, so different positions of only one dopant atom could also be tested there. However, as Al doped CHA is one of the most prevalent SCR catalysts today [71, 85], to look at it first was an obvious choice. Unfortunately, the computational time needed to explore different dopant distributions in BEA and MFI would be a large limitation.

Another type of counter ion could also be tested, instead of H or Cu. A counter ion that is a widely used alternative to Cu is Fe [91]. Both its capabilities in NH<sub>3</sub> adsorption and O<sub>2</sub> dissociation could be tested.



# 7

## Conclusion

Adsorption energies of  $\text{NH}_3$  in CHA, BEA, MFI and AlPO for various dopant atom types and distributions with  $\text{H}^+$ , Cu(I), Cu(II) and Cu(II) with  $(\text{OH})^-$  adsorbed as counter ions have been calculated. For  $\text{H}^+$ , the type of dopant atom influences the adsorption energies by up to 0.6 eV, and the differences are also big with Cu(II) as a dopant atom. However, for Cu(I) and Cu(II) with  $(\text{OH})^-$  adsorbed, the differences are not that substantial. The type of zeolite framework has a considerable impact on the adsorption energies.

What was found to impact the adsorption energies the most is the positions of dopant atoms relative to each other, with Cu(II) as counter ion. This is made clear by the exploration of 17 different distributions of Al dopant atoms in CHA, presented in section 5.7. Some of these dopant distributions are better suited for SCR applications than others. For distributions a, d and g,  $\text{NH}_3$  desorb at temperatures outside of SCR standard operating conditions, while for distribution q most  $\text{NH}_3$  desorb during the standard operating conditions. This makes q the preferred dopant distribution to aim for during the synthesis, out of the ones considered.

Even though BEA, MFI and AlPO might have some advantages compared to CHA, they are overall less stable than CHA and are therefore less suited for SCR operating conditions. Because of this, the differences of the adsorption energies for the Al dopant distributions in CHA are of most interest for SCR applications. The obtained results can hopefully be of use when synthesising zeolites, to further reduce  $\text{NO}_x$  emissions stemming from diesel engines.



# Bibliography

- [1] R. van Santen. *Modern Heterogeneous Catalysis*. John Wiley & Sons, Ltd, 2017.
- [2] F. Gao, J. H. Kwak, J. Szanyi, and C. H. F. Peden. Current Understanding of Cu-Exchanged Chabazite Molecular Sieves for Use as Commercial Diesel Engine DeNO<sub>x</sub> Catalysts. *Topics in Catalysis*, 56(15):1441–1459, Nov 2013.
- [3] D. Vallero. *Fundamentals of Air Pollution (5th Edition)*. Elsevier, 2014.
- [4] X. Yuan, H. Liu, and Y. Gao. Diesel Engine SCR Control: Current Development and Future Challenges. *Emission Control Science and Technology*, 1(2):121–133, May 2015.
- [5] J. Wang, H. Chen, Z. Hu, M. Yao, and Y. Li. A Review on the Pd-Based Three-Way Catalyst. *Catalysis Reviews*, 57(1):79–144, 2015.
- [6] J. Weitkamp. Zeolites and catalysis. *Solid State Ionics*, 131(1):175 – 188, 2000.
- [7] L. Chen, T. V. W. Janssens, M. Skoglundh, and H. Grönbeck. Interpretation of NH<sub>3</sub>-TPD Profiles from Cu-CHA Using First-Principles Calculations. *Topics in Catalysis*, 62(1):93–99, Feb 2019.
- [8] C. Paolucci, A. A. Parekh, I. Khurana, J. R. Di Iorio, H. Li, J. D. Albarracin Caballero, A. J. Shih, T. Anggara, W. N. Delgass, J. T. Miller, F. H. Ribeiro, R. Gounder, and W. F. Schneider. Catalysis in a Cage: Condition-Dependent Speciation and Dynamics of Exchanged Cu Cations in SSZ-13 Zeolites. *Journal of the American Chemical Society*, 138(18):6028–6048, 2016. PMID: 27070199.
- [9] T. V. Johnson. *Review of Selective Catalytic Reduction (SCR) and Related Technologies for Mobile Applications*, pages 3–31. Springer New York, New York, NY, 2014.
- [10] L. S. Dent and J. V. Smith. Crystal Structure of Chabazite, a Molecular Sieve. *Nature*, 181:1794–1796, jun 1958.
- [11] P. N. Plessow and F. Studt. Unraveling the Mechanism of the Initiation Reaction of the Methanol to Olefins Process Using ab Initio and DFT Calculations. *ACS Catalysis*, 7(11):7987–7994, 2017.
- [12] P. N. Plessow and F. Studt. Theoretical Insights into the Effect of the Framework on the Initiation Mechanism of the MTO Process. *Catalysis Letters*, 148(4):1246–1253, Apr 2018.
- [13] J. N. Brønsted. Einige Bemerkungen über den Begriff der Säuren und Basen. *Recueil des Travaux Chimiques des Pays-Bas*, 42(8):718–728, 1923.
- [14] L. Chen, H. Falsig, T. V. W. Janssens, J. Jansson, M. Skoglundh, and H. Grönbeck. Effect of Al-distribution on oxygen activation over Cu-CHA. *Catal. Sci. Technol.*, 8:2131–2136, 2018.

- [15] W. Löwenstein. The distribution of aluminum in the tetrahedra of silicate and aluminates. *American Mineralogist*, 39:92–96, 1954.
- [16] T. Nishitoba, N. Yoshida, J. N. Kondo, and T. Yokoi. Control of Al Distribution in the CHA-Type Aluminosilicate Zeolites and Its Impact on the Hydrothermal Stability and Catalytic Properties. *Industrial & Engineering Chemistry Research*, 57(11):3914–3922, 2018.
- [17] O. Larlus and V. P. Valtchev. Control of the Morphology of All-Silica BEA-type Zeolite Synthesized in Basic Media. *Chemistry of Materials*, 17(4):881–886, 2005.
- [18] O. H. Han, C. S. Kim, and S. B. Hong. Direct Evidence for the Nonrandom Nature of Al Substitution in Zeolite ZSM-5: An Investigation by  $^{27}\text{Al}$  MAS and MQ MAS NMR. *Angewandte Chemie International Edition*, 41(3):469–472, 2002.
- [19] V. Gábová, J. Dědeček, and J. Čejka. Control of Al distribution in ZSM-5 by conditions of zeolite synthesis. *Chem. Commun.*, pages 1196–1197, 2003.
- [20] R. O. Jones and O. Gunnarsson. The density functional formalism, its applications and prospects. *Rev. Mod. Phys.*, 61:689–746, Jul 1989.
- [21] A. D. Becke. Perspective: Fifty years of density-functional theory in chemical physics. *The Journal of Chemical Physics*, 140(18):18A301, 2014.
- [22] E. Schrödinger. Quantisierung als Eigenwertproblem. *Annalen der Physik*, 384(4):361–376, 1926.
- [23] B. H. Bransden and C. J. Joachain. *Physics of atoms and molecules*. Prentice Hall, 2003.
- [24] M. Born and R. Oppenheimer. Zur Quantentheorie der Molekeln. *Annalen der Physik*, 389(20):457–484, 1927.
- [25] L. H. Thomas. The calculation of atomic fields. *Mathematical Proceedings of the Cambridge Philosophical Society*, 23(5):542–548, 1927.
- [26] E. Fermi. Un Metodo Statistico per la Determinazione di alcune Prioprietà dell’Atomo. *Rendiconti Accademia Dei Lincei*, 6:602–607, 1927.
- [27] P. Hohenberg and W. Kohn. Inhomogeneous Electron Gas. *Phys. Rev.*, 136:B864–B871, Nov 1964.
- [28] W. Kohn and L. J. Sham. Self-Consistent Equations Including Exchange and Correlation Effects. *Phys. Rev.*, 140:A1133–A1138, Nov 1965.
- [29] U. von Barth and L. Hedin. A local exchange-correlation potential for the spin polarized case. i. *Journal of Physics C: Solid State Physics*, 5(13):1629–1642, jul 1972.
- [30] D. C. Langreth and M. J. Mehl. Beyond the local-density approximation in calculations of ground-state electronic properties. *Phys. Rev. B*, 28:1809–1834, Aug 1983.
- [31] A. D. Becke. Density functional calculations of molecular bond energies. *The Journal of Chemical Physics*, 84(8):4524–4529, 1986.
- [32] M. Ernzerhof and G. E. Scuseria. Assessment of the Perdew-Burke-Ernzerhof exchange-correlation functional. *The Journal of Chemical Physics*, 110(11):5029–5036, 1999.
- [33] J. P. Perdew, K. Burke, and M. Ernzerhof. Generalized Gradient Approximation Made Simple. *Phys. Rev. Lett.*, 77:3865–3868, Oct 1996.

- 
- [34] S. Grimme, J. Antony, S. Ehrlich, and H. Krieg. A consistent and accurate ab initio parametrization of density functional dispersion correction (DFT-D) for the 94 elements H-Pu. *The Journal of Chemical Physics*, 132(15):154104, 2010.
- [35] C. Kittel. *Introduction to Solid State Physics*. Wiley, 8 edition, 2004.
- [36] F. Bloch. Über die Quantenmechanik der Elektronen in Kristallgittern. *Zeitschrift für Physik*, 52(7):555–600, Jul 1929.
- [37] M. C. Payne, M. P. Teter, D. C. Allan, T. A. Arias, and J. D. Joannopoulos. Iterative minimization techniques for ab initio total-energy calculations: molecular dynamics and conjugate gradients. *Rev. Mod. Phys.*, 64:1045–1097, Oct 1992.
- [38] P. E. Blöchl. Projector augmented-wave method. *Phys. Rev. B*, 50:17953–17979, Dec 1994.
- [39] J. Kohanoff. *Electronic Structure Calculations for Solids and Molecules: Theory and Computational Methods*. Cambridge University Press, 2006.
- [40] H. Hellmann. *Einführung in die Quantenchemie*. Leipzig: Franz Deuticke, 1937.
- [41] R. P. Feynman. Forces in Molecules. *Phys. Rev.*, 56:340–343, Aug 1939.
- [42] J. P. Perdew, S. Kurth, and D. Joubert. *Density Functionals: Theory and Applications, Density functionals for non-relativistic coulomb systems*, pages 8–59. Springer Berlin Heidelberg, Berlin, Heidelberg, 1998.
- [43] M. R. Hestenes and E. Stiefel. *Methods of conjugate gradients for solving linear systems*, volume 49. Journal of Research of the National Bureau of Standards, 1952.
- [44] D. Sholl and J. A. Steckel. *Density Functional Theory: A Practical Introduction*. John Wiley & Sons, Ltd, 2009.
- [45] D. A. McQuarrie and J. D. Simon. *Physical Chemistry: A Molecular Approach*. University Science Books, Sausalito, Calif., 1997.
- [46] M. Jørgensen and H. Grönbeck. Adsorbate entropies with complete potential energy sampling in microkinetic modeling. *The Journal of Physical Chemistry C*, 121(13):7199–7207, 2017.
- [47] W. Heisenberg. Über den anschaulichen Inhalt der quantentheoretischen Kinetik und Mechanik. *Zeitschrift für Physik*, 43(3):172–198, Mar 1927.
- [48] T. M. Lowry. The uniqueness of hydrogen. *Journal of the Society of Chemical Industry*, 42(3):43–47, 1923.
- [49] A. Arvidsson. *Partial methane oxidation: insights from first principles and micro-kinetics calculations*. PhD thesis, Chalmers University of Technology, May 2019.
- [50] I. D. Brown. Recent Developments in the Methods and Applications of the Bond Valence Model. *Chemical Reviews*, 109(12):6858–6919, 2009. PMID: 19728716.
- [51] J. A. Enterkin, A. E. Becerra-Toledo, K. R. Poepelmeier, and L. D. Marks. A chemical approach to understanding oxide surfaces. *Surface Science*, 606(3):344–355, 2012.
- [52] T. A. Manz. Introducing DDEC6 atomic population analysis: part 3. Comprehensive method to compute bond orders. *RSC Adv.*, 7:45552–45581, 2017.

- [53] T. A. Manz and N. G. Limas. Introducing DDEC6 atomic population analysis: part 1. Charge partitioning theory and methodology. *RSC Adv.*, 6:47771–47801, 2016.
- [54] D. A. McQuarrie and J. D. Simon. *Molecular Thermodynamics*. University Science Books, 1999.
- [55] D. V. Schroeder. *An Introduction to Thermal Physics*. Addison Wesley, 1999.
- [56] J. Rogal and K. Reuter. Ab initio atomistic thermodynamics for surfaces: A primer. Technical report, Max-Planck-Gesellschaft zur Förderung der Wissenschaften e.V. Büro Berlin, 2006.
- [57] M. W. Chase. *NIST-JANAF thermochemical tables*. Journal of physical and chemical reference data. Monograph ; no. 9. American Chemical Society, Washington, D.C, 4th ed. edition, 1998.
- [58] M. Niwa, N. Katada, M. Sawa, and Y. Murakami. Temperature-Programmed Desorption of Ammonia with Readsorption Based on the Derived Theoretical Equation. *The Journal of Physical Chemistry*, 99(21):8812–8816, 1995.
- [59] N. Katada, H. Igi, J. H. Kim, and M. Niwa. Determination of the Acidic Properties of Zeolite by Theoretical Analysis of Temperature-Programmed Desorption of Ammonia Based on Adsorption Equilibrium. *The Journal of Physical Chemistry B*, 101(31):5969–5977, 1997.
- [60] S. J. Schmiege, S. H. Oh, C. H. Kim, D. B. Brown, J. H. Lee, C. H. F. Peden, and D. Heui Kim. Thermal durability of Cu-CHA NH<sub>3</sub>-SCR catalysts for diesel NO<sub>x</sub> reduction. *Catalysis Today*, 184(1):252 – 261, 2012. Catalytic Control of Lean-Burn Engine Exhaust Emissions.
- [61] S. B. Liu, J. F. Wu, L. J. Ma, T. C. Tsai, and I. Wang. On the thermal stability of zeolite beta. *Journal of Catalysis*, 132(2):432 – 439, 1991.
- [62] T. C. Hoff, R. Thilakaratne, D. W. Gardner, R. C. Brown, and J. P. Tessonier. Thermal Stability of Aluminum-Rich ZSM-5 Zeolites and Consequences on Aromatization Reactions. *The Journal of Physical Chemistry C*, 120(36):20103–20113, 2016.
- [63] Y. Watanabe, A. Koiwai, H. Takeuchi, S. A. Hyodo, and S. Noda. Multinuclear NMR Studies on the Thermal Stability of SAPO-34. *Journal of Catalysis*, 143(2):430 – 436, 1993.
- [64] P. G. Blakeman, E. M. Burkholder, H. Y. Chen, J. E. Collier, J. M. Fedeyko, H. Jobson, and R. R. Rajaram. The role of pore size on the thermal stability of zeolite supported Cu SCR catalysts. *Catalysis Today*, 231:56 – 63, 2014. Challenges for Catalytic Exhaust Aftertreatment.
- [65] G. Kresse and J. Hafner. Ab initio molecular dynamics for liquid metals. *Phys. Rev. B*, 47:558–561, Jan 1993.
- [66] G. Kresse and J. Furthmüller. Efficiency of ab-initio total energy calculations for metals and semiconductors using a plane-wave basis set. *Computational Materials Science*, 6(1):15 – 50, 1996.
- [67] G. Kresse and J. Furthmüller. Efficient iterative schemes for ab initio total-energy calculations using a plane-wave basis set. *Phys. Rev. B*, 54:11169–11186, Oct 1996.
- [68] G. Kresse and D. Joubert. From ultrasoft pseudopotentials to the projector augmented-wave method. *Phys. Rev. B*, 59:1758–1775, Jan 1999.

- [69] L. Chen, T. V. W. Janssens, and H. Grönbeck. A comparative test of different density functionals for calculations of NH<sub>3</sub>-SCR over Cu-Chabazite. *Phys. Chem. Chem. Phys.*, 21:10923–10930, 2019.
- [70] N. G. Limas and T. A. Manz. Introducing DDEC6 atomic population analysis: part 4. Efficient parallel computation of net atomic charges, atomic spin moments, bond orders, and more. *RSC Adv.*, 8:2678–2707, 2018.
- [71] L. Chen, H. Falsig, T. V. W. Janssens, and H. Grönbeck. Activation of oxygen on (NH<sub>3</sub>CuNH<sub>3</sub>)<sup>+</sup> in NH<sub>3</sub>-SCR over Cu-CHA. *Journal of Catalysis*, 358:179 – 186, 2018.
- [72] T. Lu, W. Yan, and R. Xu. Chiral zeolite beta: structure, synthesis, and application. *Inorg. Chem. Front.*, 6:1938–1951, 2019.
- [73] J. M. Newsam, M. M. J. Treacy, W. T. Koetsier, and C. B. De Gruyter. Structural Characterization of Zeolite Beta. *Proceedings of the Royal Society of London. Series A, Mathematical and Physical Sciences*, 420(1859):375–405, 1988.
- [74] D. H. Olson, G. T. Kokotailo, S. L. Lawton, and W. M. Meier. Crystal structure and structure-related properties of ZSM-5. *The Journal of Physical Chemistry*, 85(15):2238–2243, 1981.
- [75] H. van Koningsveld and J. C. Jansen. Single crystal structure analysis of zeolite H-ZSM-5 loaded with naphthalene. *Microporous Materials*, 6(3):159 – 167, 1996.
- [76] AlPO<sub>4</sub>; AlPO-34 (Al[PO<sub>4</sub>]<sup>-34</sup>, T = 260 K) Crystal Structure: Datasheet from “PAULING FILE Multinaries Edition – 2012” in SpringerMaterials ([https://materials.springer.com/isp/crystallographic/docs/sd\\_1628437](https://materials.springer.com/isp/crystallographic/docs/sd_1628437)).
- [77] R. Y. Brogaard, B. M. Weckhuysen, and J. K. Nørskov. Guest-host interactions of arenes in H-ZSM-5 and their impact on methanol-to-hydrocarbons deactivation processes. *Journal of Catalysis*, 300:235–241, 2013.
- [78] S. M. Opalka and T. Zhu. Influence of the Si/Al ratio and Al distribution on the H-ZSM-5 lattice and Brønsted acid site characteristics. *Microporous and Mesoporous Materials*, 222:256 – 270, 2016.
- [79] X. Yu, B. Liu, and Y. Zhang. Effect of Si/Al ratio of high-silica HZSM-5 catalysts on the prins condensation of isobutylene and formaldehyde to isoprene. *Heliyon*, 5(5):e01640, 2019.
- [80] N. J. Venkatesha, Y. Bhat, and B. S. Jaiprakash. Dealuminated BEA Zeolite for selective synthesis of five-membered cyclic acetal from glycerol under ambient conditions. *RSC Advances*, 6:18824–18833, 02 2016.
- [81] L. Rodríguez-González, F. Hermes, M. Bertmer, E. Rodríguez-Castellón, A. Jiménez-López, and U. Simon. The acid properties of H-ZSM-5 as studied by NH<sub>3</sub>-TPD and 27Al-MAS-NMR spectroscopy. *Applied Catalysis A: General*, 328(2):174 – 182, 2007.
- [82] J. Liang, H. Li, S. Zhao, W. Guo, R. Wang, and M. Ying. Characteristics and performance of SAPO-34 catalyst for methanol-to-olefin conversion. *Applied Catalysis*, 64:31 – 40, 1990.
- [83] M. Busch, R. B. Wang, A. Hellman, J. Rossmeisl, and H. Grönbeck. The Influence of Inert Ions on the Reactivity of Manganese Oxides. *The Journal of Physical Chemistry C*, 122(1):216–226, 2018.

- [84] H. A. Jahn and E. Teller. Stability of Polyatomic Molecules in Degenerate Electronic States. I. Orbital Degeneracy. *Proceedings of the Royal Society of London. Series A, Mathematical and Physical Sciences*, 161(905):220–235, 1937.
- [85] C. Wen, L. Geng, L. Han, J. Wang, L. Chang, G. Feng, D. Kong, and J. Liu. A comparative first principles study on trivalent ion incorporated SSZ-13 zeolites. *Phys. Chem. Chem. Phys.*, 17:29586–29596, 2015.
- [86] W. C. Swope, H. C. Andersen, P. H. Berens, and K. R. Wilson. A computer simulation method for the calculation of equilibrium constants for the formation of physical clusters of molecules: Application to small water clusters. *The Journal of Chemical Physics*, 76(1):637–649, 1982.
- [87] W. K. Hastings. Monte Carlo sampling methods using Markov chains and their applications. *Biometrika*, 57(1):97–109, 04 1970.
- [88] M. Jørgensen, L. Chen, and H. Grönbeck. Correction to “Monte Carlo Potential Energy Sampling for Molecular Entropy in Zeolite”. *The Journal of Physical Chemistry C*, 123(15):10166–10166, 2019.
- [89] J. Bauer, T. Selvam, J. Ofili, E. Che, R. Herrmann, and W. Schwieger. Stability of AlPO and SAPO molecular sieves during adsorption-desorption cycles of water vapor investigated by in-situ XRD measurements. In R. Xu, Z. Gao, J. Chen, and W. Yan, editors, *From Zeolites to Porous MOF Materials - The 40th Anniversary of International Zeolite Conference*, volume 170 of *Studies in Surface Science and Catalysis*, pages 837 – 844. Elsevier, 2007.
- [90] J. Wang, M. Yang, W. Shang, X. Su, Q. Hao, H. Chen, and X. Ma. Synthesis, characterization, and catalytic application of hierarchical SAPO-34 zeolite with three-dimensionally ordered mesoporous-imprinted structure. *Microporous and Mesoporous Materials*, 252:10 – 16, 2017.
- [91] S. Brandenberger, O. Kröcher, A. Tissler, and R. Althoff. The State of the Art in Selective Catalytic Reduction of NOx by Ammonia Using Metal-Exchanged Zeolite Catalysts. *Catalysis Reviews*, 50(4):492–531, 2008.